University of Alberta

Development of an Ultrasonic Gas Sensor for Automotive Use

by

Jason Scott Olfert ©

A thesis submitted to the Faculty of Graduate Studies and Research in partial fulfillment of the requirements for the degree of Master of Science.

Department of Mechanical Engineering

Edmonton, Alberta
Fall 2003

Library and
Archives Canada

Published Heritage
Branch

395 Wellington Street
Ottawa ON K1A 0N4
Canada

Bibliothèque et
Archives Canada

Direction du
Patrimoine de l'édition

395, rue Wellington
Ottawa ON K1A 0N4
Canada

Your file Votre référence
ISBN: 0-612-95895-7
Our file Notre référence
ISBN: 0-612-95895-7

The author has granted a non-exclusive license allowing the Library and Archives Canada to reproduce, loan, distribute or sell copies of this thesis in microform, paper or electronic formats.

The author retains ownership of the copyright in this thesis. Neither the thesis nor substantial extracts from it may be printed or otherwise reproduced without the author's permission.

L'auteur a accordé une licence non exclusive permettant à la Bibliothèque et Archives Canada de reproduire, prêter, distribuer ou vendre des copies de cette thèse sous la forme de microfiche/film, de reproduction sur papier ou sur format électronique.

L'auteur conserve la propriété du droit d'auteur qui protège cette thèse. Ni la thèse ni des extraits substantiels de celle-ci ne doivent être imprimés ou aturement reproduits sans son autorisation.

In compliance with the Canadian Privacy Act some supporting forms may have been removed from this thesis.

While these forms may be included in the document page count, their removal does not represent any loss of content from the thesis.

Conformément à la loi canadienne sur la protection de la vie privée, quelques formulaires secondaires ont été enlevés de cette thèse.

Bien que ces formulaires aient inclus dans la pagination, il n'y aura aucun contenu manquant.

Canada

Reproduced with permission of the copyright owner. Further reproduction prohibited without permission.

A feeble youth had he fallen to the earth, yet now he arose a resolute warrior for the rest of his life and knew and felt this suddenly, at that same moment of his ecstacy. And never, never for all the rest of his life would Alyosha be able to forget that moment. 'Someone visited my soul in that hour,' he would say later with resolute faith in his words...

Three days later he left the monastery, something that was also in concordance with the precept of his deceased Elder, who had commanded him to 'sojourn in the world'.

Fyodor Dostoyevsky
The Brothers Karamazov

By faith he sojourned in the land of promise as in a foreign country...
Hebrews 11:9a

To Michaelia

ACKNOWLEDGEMENTS

I would like to thank to following people for their contribution to this project:

Dr. M.D. Checkel and Dr. C.R. Koch for their supervision and guidance.

Terry Nord for providing invaluable help with developing the electronics on the prototype sensor.

Rick Bubenko for providing mechanical insight for the machining of the prototype sensor.

Machine Shop staff who contributed to this project including, Bernie Faulkner, Albert Yuen, Andrew Coward and Dirk Kelm.

Natural Science and Engineering Research Council (NSERC), Luscar Ltd., Faculty of Engineering, Alberta Heritage Scholarship Fund, David Morris and Walter Johns for their financial contribution.

The Combustion & Environment Research Group for providing technical and non-technical support.

My wife, Michaelia, for her relentless editing.

Finally, my family, who have supported me through out my education.

TABLE OF CONTENTS

LIST OF TABLES

LIST OF FIGURES

LIST OF NOMENCLATURE

A	Amplitude
α	Acoustic Absorption Coefficient
α_r	Acoustic Reflection Coefficient
c	Sound Speed
c_d	Damping Constant
d	Path Length of Ultrasonic Sensor
d^*	Theoretical Path Length
D	Diameter of Ultrasonic Transducer
δ_{total}	Total Error, Accuracy
δ_{cal}	Calibration Error
δ_r	Repeatability Error
δ_{res}	Resolution Error
EGR	Mass Fraction of EGR
F	Force
f	Frequency of Acoustic Wave
f_n	Natural or Resonant Frequency
γ	ratio of C_p to C_v
h	Specific Enthalpy
HHV	Higher Heating Value
I	Intensity of Acoustic Wave

k	Spring Constant
LFL	Lean Flammability Limit
m	Mass
$\dot{m}$	Mass Flow Rate
M	Molecular Weight
P	Pressure
ϕ	Phase Difference of Acoustic Waves
Φ	Time Difference of Acoustic Waves
Q	Volumetric Flow Rate
$\dot{Q}$	Heat Transfer Rate
Q_m	Mechanical Q Factor
ρ	Density
R	Universal Gas Constant
t	Time
sg	Specific Gravity
T	Temperature
θ	Phase Range of Phase Comparator
W	Wobbe Number
x	Displacement
y	Molecular or Volume Fraction of Gas
Z	Acoustic Impedance
ζ	Damping Factor

CHAPTER 1

INTRODUCTION

THE performance of internal combustion engines has greatly improved since their invention. In recent years, the major focus of improvements has been exhaust emissions and fuel efficiency. These improvements have been made through the use of technologies such as control systems, catalytic converters, exhaust gas recirculation and the use of alternative fuels. Most of these technologies make use of sensors to improve the performance of the system. The sensors that are used must be cost effective, durable, accurate and have fast response times. This thesis describes the development of an ultrasonic sensor for automotive use with examples of automotive applications.

The purpose of this project was to develop a sensor to measure the sound speed of a gaseous medium in an automotive environment. The sound speed of a gas can be related to a number of important properties such as gaseous fuel quality or gas concentration. In an automotive environment, a sensor must be durable and relatively small, so that it can fit into the engine compartment. Traditionally, sound speed measurements use acoustic techniques which required long path lengths (the distance between ultrasonic transducers), on the order of centimeters or meters, which consequently results in large sensors unsuitable for automotive applications. This thesis describes the development of a novel acoustic technique called the discrete acoustic wave and phase detection (DAWPD) method for measuring sound speeds with path lengths on the order of millimeters. This thesis also presents possible automotive applications for the sensor such as a natural gas quality sensor, variable gaseous fuel concentration sensor and an exhaust gas recirculation sensor.

Chapter 2 describes the development of the DAWPD method. The basic principles of the technique are explained and compared to other acoustic techniques. Experimental results are used to prove that the DAWPD method can provide accurate measurements over short path lengths. Sources of error are also identified and discussed. The chapter concludes by laying out design guidelines for the proper design of a sensor using the DAWPD technique.

Chapter 3 discusses two applications for an automotive DAWPD sensor. First, the sensor can be used as a natural gas quality sensor. The performance of natural gas vehicles (NGVs) can be compromised by variations in the composition of the natural gas fuel. The chapter discusses why natural gas composition can vary, how these variations can cause the quality or properties of the natural gas to change, and how changes in properties affect the performance of NGVs. Theory is given to show that the sound speed in natural gas is related to the quality of the gas. Experimental results are used to show that the DAWPD method can be used to measure the range of sound speeds common to natural gas with adequate accuracy for the application.

The second application for a DAWPD sensor is to be used as a variable gaseous fuel (VGF) concentration sensor for VGF vehicles. A VGF vehicle is a vehicle that uses natural gas, hydrogen, or a mixture of the two gases for fuel. For proper operation of a VGF vehicle the concentration of the fuel (ie. the quantity of hydrogen and methane) must be known. Chapter 3 shows how sound speed measurements can be used to relate the sound speed of the fuel to the concentration of the gas mixture. Experimental results are given to show that the DAWPD method can be used to measure the concentration of a natural gas and hydrogen gas mixture with reasonable accuracy. Suggestions are made for improvements in measuring sound speeds with the DAWPD method in a variable fuel mixture.

Chapter 4 describes a third application for a DAWPD sensor – an exhaust gas recirculation sensor. Exhaust gas recirculation (EGR) has been used to reduce oxides of nitrogen (NO_x) in combustion engine emissions. Proper measurement of EGR rates can improve the performance of emission control systems. The chapter discusses the theory behind EGR measurement with a sound speed sensor. Also, experimental measurements were used to show that EGR can be measured on an engine. Problems with EGR measurement with a sound speed sensor are discussed and recommendations for further research are given.

In Chapter 5, the conclusion to this thesis is given. The major thesis conclusions are summarized and future work is considered. The future work considers the use of micro-electro-mechanical system (MEMS) ultrasonic transducers with the DAWPD method. Advantages for these types transducers in automotive applications are discussed.

CHAPTER 2

DEVELOPMENT OF AN ULTRASONIC GAS SENSOR

2.1 Introduction

ULTRASONIC gas sensors which measure sound speeds have a number of useful applications in industry such as gas composition and temperature measurement. Various acoustic methods have been used in the past to measure sound speeds in gases. Most of these methods are based on "time-of-flight" and require long path lengths (and therefore large sensors) to make accurate sound speed measurements. This chapter discusses how a discrete acoustic wave and phase detection (DAWPD) method can be used to measure sound speeds using a short path length. This technique makes it possible to accurately measure sound speed with sensors of millimeter or sub-millimeter dimensions.

This chapter presents the theory behind using sound speeds to measure gas composition and temperature. Prototype sensors used to test this theory are described and their performance experimentally measured. Sources of error and uncertainty are discussed and techniques for reducing these uncertainties are presented and experimentally verified.

Based on this work, design guidelines have been developed which are useful in designing a scaled down micro-sensor. These guidelines include equations which relate the path length of the sensor with the driving frequency and diameter of the transducer. These relations show that a suitable micro-sensor can be made using the DAWPD method.

2.2 Relation Between Gas Concentration, Temperature and Sound Speed

Acoustic methods have been used in the past to measure the concentration or thermodynamic properties of fluids such as gases[1–3]. In particular, the sound speed of a gas can be used to determine its properties. Assuming it is an ideal gas, the sound speed can be calculated using Eq. 2.1:

$$c = \sqrt{\frac{\gamma RT}{M}} \tag{2.1}$$

where R is the universal gas constant, T is the temperature, M is the molecular weight and γ is the ratio of specific heat at constant pressure, C_p, to the specific heat at constant volume, C_v.

For any gas mixture, c is affected by the temperature, molar mass and the ratio of specific heats, γ. γ is generally inversely correlated with molar mass, so $c \propto (\gamma/M)^{\frac{1}{2}}$ is a slightly stronger relationship than $c \propto T^{\frac{1}{2}}$.

For a mixture of gases the sound speed can be found from Eq. 2.2:

$$c = \sqrt{\frac{\sum_i y_i C_{p_i}}{\sum_i y_i C_{v_i}} \frac{RT}{\sum_i y_i M_i}} \tag{2.2}$$

where y_i is the molar or volume fraction of gas i, C_{p_i} and C_{v_i} are the specific heats for gas i and M_i is the molecular weight of gas i.

For a binary or quasi-binary gas mixture Eq. 2.2 can be simplified. A binary gas is gas mixture made of two gases and a quasi-binary gas mixture is a gas composed of more than two gases where two or more gases are compositionally related. An example is a mixture of air and carbon monoxide (CO). Air is composed of oxygen and nitrogen in a fixed ratio (21% O_2 and 79% N_2). From Eq. 2.2, the sound speed for a binary or quasi-binary mixture can be expressed as:

$$c = \sqrt{\frac{RT(y_1 C_{p_1} + (1 - y_1) C_{p_2})}{(y_1 M_1 + (1 - y_1) M_2)(y_1 C_{v_1} + (1 - y_1) C_{v_2})}} \tag{2.3}$$

choosing gas 1 with concentration, y_1, to have the lower sound speed.

The concentration of gas 1 can be found by arranging Eq. 2.3 to give:

$$y_1 = \frac{-b + \sqrt{b^2 - 4ad}}{2a} \tag{2.4}$$

where

$$a = \frac{c^2}{RT}[M_1(C_{v1} - C_{v2}) + M_2(C_{v2} - C_{v1})] \tag{2.5}$$

$$b = \frac{c^2}{RT}[M_1 C_{v2} + M_2(C_{v1} - 2C_{v2})] - C_{p1} + C_{p2} \tag{2.6}$$

and

$$d = \frac{c^2}{RT} M_2 C_{v2} - C_{p2} \tag{2.7}$$

This is the basis for using sound speed to measure gas composition and temperature.

2.3 Sound Speed Measurement Methods

Numerous acoustic methods can be used to determine the sound speed of a gas[4–10]. The most commonly used method is the time-of-flight method which requires long path lengths or reflection techniques for adequate accuracy and resolution. Uncertainty analysis (see App. A) shows that at short path lengths, the uncertainty in the time-of-flight method can be extremely high, showing that it is much better suited to long path lengths.

The uncertainty in the sensor is highly sensitive to the transducers used. Piezoceramic transducers are a common, commercially available and inexpensive ultrasonic transducer that generally operates in the 40 kHz range. These transducers use mechanical structures to match the impedance of the piezoelectric ceramic to the impedance of air. These devices are resonant in nature, requiring a series of pulses to fully excite the transducer. Figure 2.1 shows the build-up of the receiving signal of a resonant ultrasonic transducer. The resonant nature of this signal causes error in the time measurement because it is uncertain which pulse is the first pulse received in the train of pulses. The build-up period depends on the particular transducer used, however for this error analysis we will conservatively assume a build-up period of one half wavelength (a less conservative error estimate being 1 or 2 wavelengths). Therefore at a frequency of 40 kHz the uncertainty in the time dimension will be one-half of the period or 12.5×10^{-6}s. As the path length of the sensor becomes smaller the uncertainty in the time dimension becomes proportionally larger. Over a short path length the time measurement will be on the same order of magnitude as the uncertainty in the time measurement (ie. the time measurement and the error in the time measurement are both on the order of μs). Figure 2.2 is a plot of the uncertainty of the sensor as a function of path length, as derived in App. A.

To reduce the uncertainty in the time dimension a higher frequency transducer can be used. Since the wavelength will be shorter for a higher frequency wave, the time uncertainty will be reduced. The uncertainty in the time dimension can also be reduced by using broadband high frequency transducers[11]. Broadband transducers will not have ringing or build-up effects so the uncertainty in the time dimension can be reduced dramatically, allowing for shorter path lengths.

Increasing the frequency and using broadband transducers reduces some error in

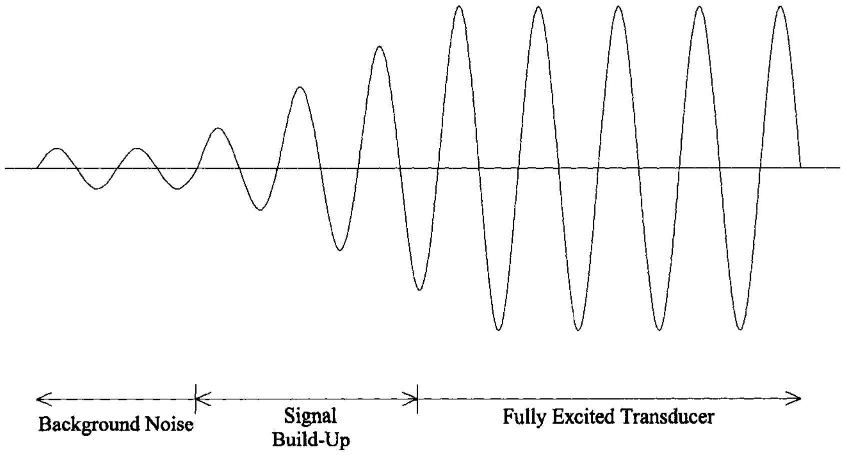

Figure 2.1: Signal Build-Up of Receiving Ultrasonic Transducer

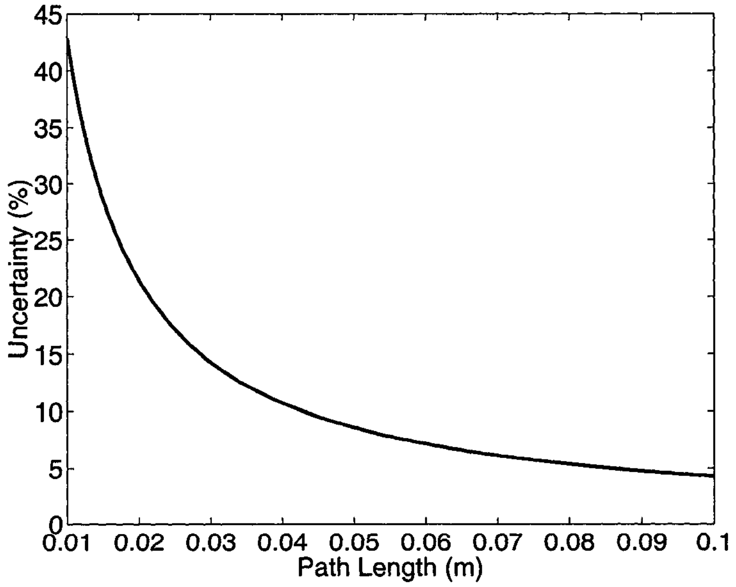

Figure 2.2: Uncertainty of Time-of-Flight Method Over Various Path Lengths

the time dimension, but as the path length becomes shorter another cause of error becomes more apparent. As the path lengths become small the time measurement will also become very small, which necessitates the use of more sophisticated and expensive timing circuitry to reduce the error in the time measurement.

Time-of-flight methods also have limited response times because single sound pulses are sent and received. Resonant piezoelectric transducers create a sound wave when they are driven by an electronic signal at a frequency near the resonant frequency of the transducer. It takes a finite amount of time for the transducer to begin to transmit a sound wave, and when the driving signal is terminated, the transducer will continue to ring for a period of time. The minimum time interval between sending wave pulses, known as the 'dead-zone'[12], is determined by the build-up and ringing of the piezoelectric crystal, therefore response time is limited by the ringing time of the transducer.

Time-of-flight methods are limited to in their application at short path lengths. This leads to the need for the DAWPD method.

2.4 Discrete Acoustic Wave and Phase Detection Method

A method similar to the DAWPD method has been shown in the past to produce highly sensitive measurements[10]. This chapter shows that the DAWPD method is ideal for making a sound speed sensor using a path length less than one wavelength with an extremely fast response time. Also, the circuitry is simple and cost effective.

The DAWPD method measures the phase difference between a transmitted and received ultrasonic wave, where the phase difference between the waves is proportional to the sound speed. Figure 2.3 shows a schematic diagram of the system. The frequency generator produces a continuous 40 kHz square wave (which matches the resonant frequency of the piezoelectric transducers), which drives the piezoelec-

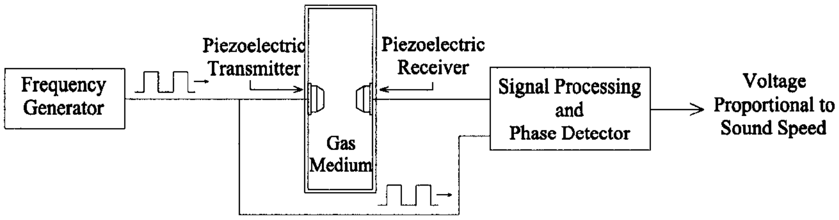

Figure 2.3: Schematic of Ultrasonic Gas Sensor

tric transmitter. The piezoelectric transmitter converts the electrical signal into an ultrasonic vibration which travels through the gas medium and is received by the piezoelectric receiver. Likewise, the receiver converts the ultrasonic signal into an electric signal which is amplified and conditioned into a square wave (also at 40 kHz). The square wave produced by the frequency generator and the square wave produced by the receiver are fed into a phase discriminator which produces a voltage which is proportional to the phase difference between the sent and received waves.

An example of an simple and cost effective phase discriminator is an exclusive OR (XOR) gate. The output of the XOR has a value of one, for two inputs where one of the inputs has a value of one; but for two inputs of zero or one the output is zero (see Table 2.1). In the application of the DAWPD method the XOR will have two square waves as inputs and a square wave as an output as seen in Fig. 2.4. The output of the XOR gate (Fig. 2.4c) goes high if the transmitted signal (Fig. 2.4a) or the received signal (Fig. 2.4b), (which will have a difference in phase, ϕ) goes high but not both. Thus as the sound speed increases, the phase difference will decrease; which changes the duty cycle of the XOR output. The XOR output is then integrated to give a

Table 2.1: XOR Gate Logic Table

Input		Output
A	B	
0	0	0
0	1	1
1	0	1
1	1	0

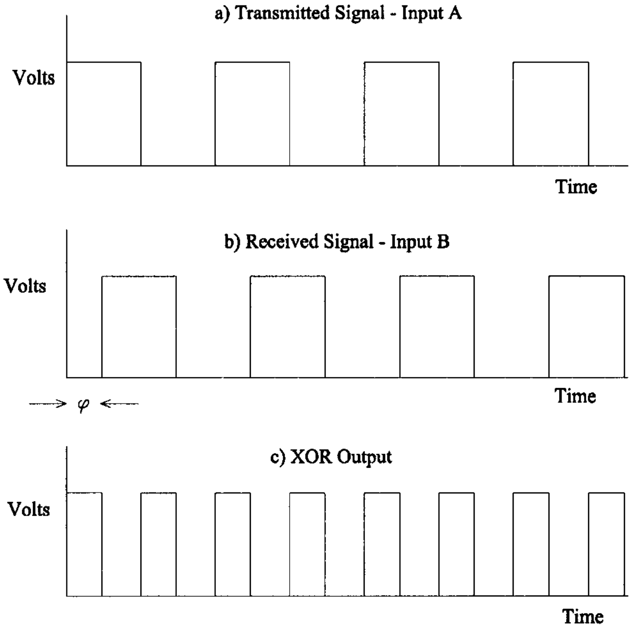

Figure 2.4: Phase Discrimination of Transmitted and Received Signals

voltage proportional to the phase difference.

The sound speed of the gas medium is proportional to the phase difference between the sent and received waves:

$$c = \frac{1}{\frac{\phi}{2\pi f d} + \frac{1}{c_{ref}}} \tag{2.8}$$

where c_{ref} is the sound speed in a reference gas, d is the path length between the speaker and microphone, f is the frequency of the ultrasonic sound wave and ϕ is the phase difference between the two waves. Graphically, Eq. 2.8 is shown in Fig. 2.5, using an example of a mixture of air and methane.

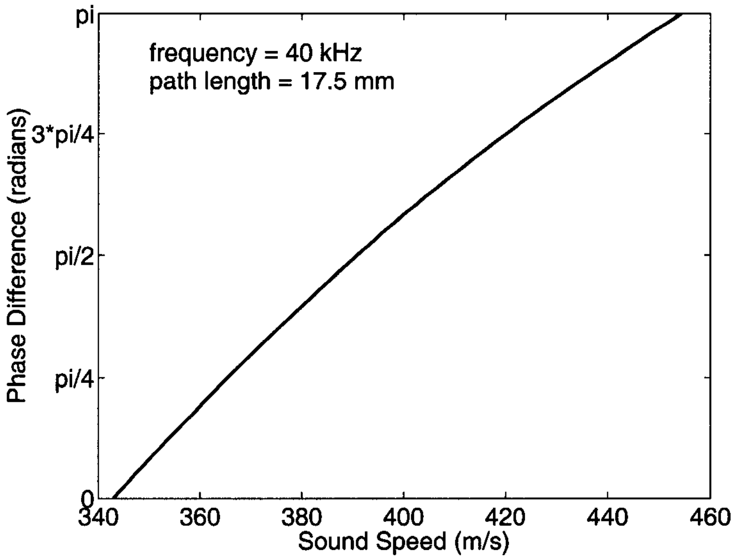

Figure 2.5: Variation of Phase Difference with Sound Speed

The advantage of the discrete acoustic wave and phase detection method is that a very small sensor can be highly sensitive. The path length of the sensor is determined by the gases to be measured, the phase range of the phase comparator and the driving frequency of the ultrasonic transducers. The ideal path length, or the path length for maximum sensitivity, between ultrasonic transducers can be found by solving Eq. 2.8 for the path length and knowing that the phase difference cannot exceed the range of the phase comparator:

$$d = \frac{\frac{1}{f}\frac{\theta}{2\pi}}{\frac{1}{c_1} - \frac{1}{c_2}} \tag{2.9}$$

where f is the driving frequency of the ultrasonic transducers, θ is the phase range of the phase comparator in radians, c_1 is the lowest sound speed that will be measured and c_2 is the highest sound speed that will be measured.

To obtain maximum sensitivity in the sensor, the full range of the phase comparator should be used. For an XOR gate phase comparator the phase range is π radians. This phase comparator provides a linear voltage for a change in phase up to π radians. If less than the full range of the phase comparator is used then sensor sensitivity will decrease. In the case of exceeding the range of the XOR comparator non-valid measurements will occur. Due to the logic of XOR gate, a phase difference of $\frac{5\pi}{4}$ will produce the same voltage output as a phase difference of $\frac{\pi}{4}$. Therefore it is imperative not to exceed the phase range of the XOR comparator.

For an example of an ideal path length calculation, a binary gas mixture of air and methane can be used. For maximum sensitivity, the sensor should be designed for a phase difference of zero radians (zero voltage output) at 0% methane concentration and phase difference of π radians (maximum voltage output) at 100% methane concentration. For this example:

f=40,000 Hz

$\theta=\pi$ (radians)

c_1=sound speed in air at 25°C = 343 m/s

c_2=sound speed in methane gas at 25°C = 451 m/s

Applying Eq. 2.9, the ideal distance, *d*, is found to be 17.5 mm.

Equation 2.9 is a useful equation for the design of a DAWPD sensor. By changing sensor parameters, such as frequency and phase comparator range, the ideal distance will change. For example, by increasing the driving frequency of the transducers the distance between the transducers should be lessened to retain maximum sensitivity. Therefore, a very small sensor can be manufactured which has excellent sensitivity.

Another advantage of the DAWPD acoustic method is that the response time is faster than that of time-of-flight methods. With time-of-flight methods over small path lengths, the time delay due to ringing effects can be on the same order of the time for the acoustic pulse to travel the path length. The DAWPD method uses continuously oscillated piezoelectric transducers, so build-up and ringing effects are not important. Without ringing effects, the response time of the DAWPD sensor is only limited by the path length, the sound speed and the transient phase response of the transducers.

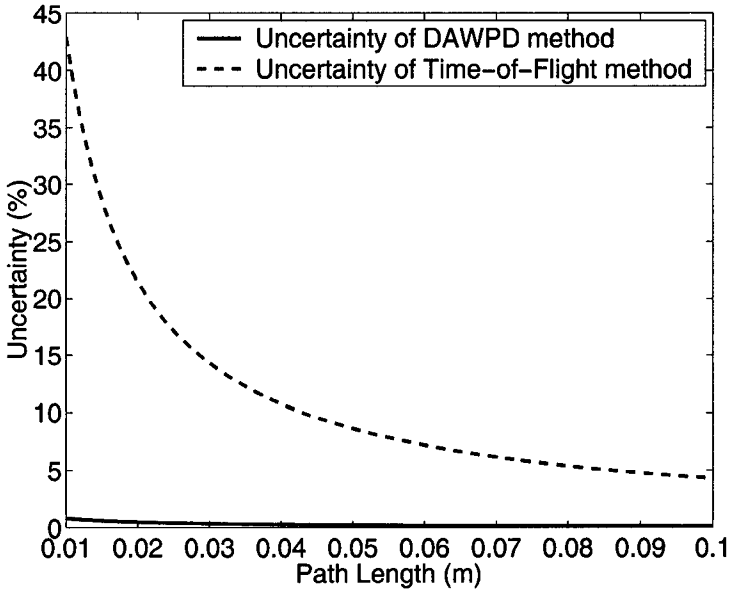

Figure 2.6: Uncertainty Comparison of DAWPD and Time-of-Flight Methods Over a Variety of Path Lengths with 40 kHz Transducers

2.5 Uncertainty in the DAWPD method

Uncertainty analysis of the DAWPD method shows (see App. A) that for short path lengths at similar operating parameters, this method will have much lower uncertainty compared to time-of-flight methods. Figure 2.6 compares the uncertainty between the two acoustic methods over a range of path lengths. The DAWPD uncertainty varies little with path length, showing that over a small path length this method will have less uncertainty than the time-of-flight method.

Although the uncertainty in the DAWPD method is nearly independent of path length, measurement error can arise from other sources. In particular the sources of uncertainty in the DAWPD measurement method comes from two major sources: i) ultrasonic reflections within the sensor and ii) resonant frequency changes of the ultrasonic transducers.

2.5.1 Reflections as a Source of Uncertainty

One of the main causes of uncertainty with the DAWPD method is error in the phase measurement caused by ultrasonic reflections within the sensor. Reflections from the interior walls of the sensor and between the transducers cause constructive and destructive interference of the original ultrasonic wave which alters the phase difference of the received wave. Figure 2.7 depicts an example of a reflection which causes a change in the phase difference of the received wave. Figures 2.7a and 2.7b show the original transmitted wave and the reflected wave, respectively. The reflected wave (which has reflected off a wall for example) will have traveled a longer path length, will have a smaller amplitude and will be out of phase of the original wave. The addition of the ultrasonic waves at the position of the receiving transducer will result in a wave of different amplitude and phase of that of the original transmitted wave, as seen in Fig. 2.7c. In this particular case the addition of the original and reflected wave resulted in a received wave of increased amplitude and decreased phase difference compared to the original wave. The change of phase is proportional to the relative amplitude of the reflected wave and the relative phase difference between the original and reflected wave. For example, if the amplitude of the reflected wave is small compared to the original wave, then the change in phase difference will be small, thereby reducing the error in the sensor. Also, when the reflected wave has a phase difference of 0, π, 2π... then the change in phase difference will be zero. However, at a phase difference of $\frac{\pi}{2}$, $\frac{3\pi}{2}$, $\frac{5\pi}{2}$... the change in phase difference will be a maximum.

This theory shows that the uncertainty is proportional to the amplitude of the reflected wave. By reducing the amplitude of the reflected wave the uncertainty of the sensor can be reduced. This will be shown experimentally in Sec. 2.6.2.2.

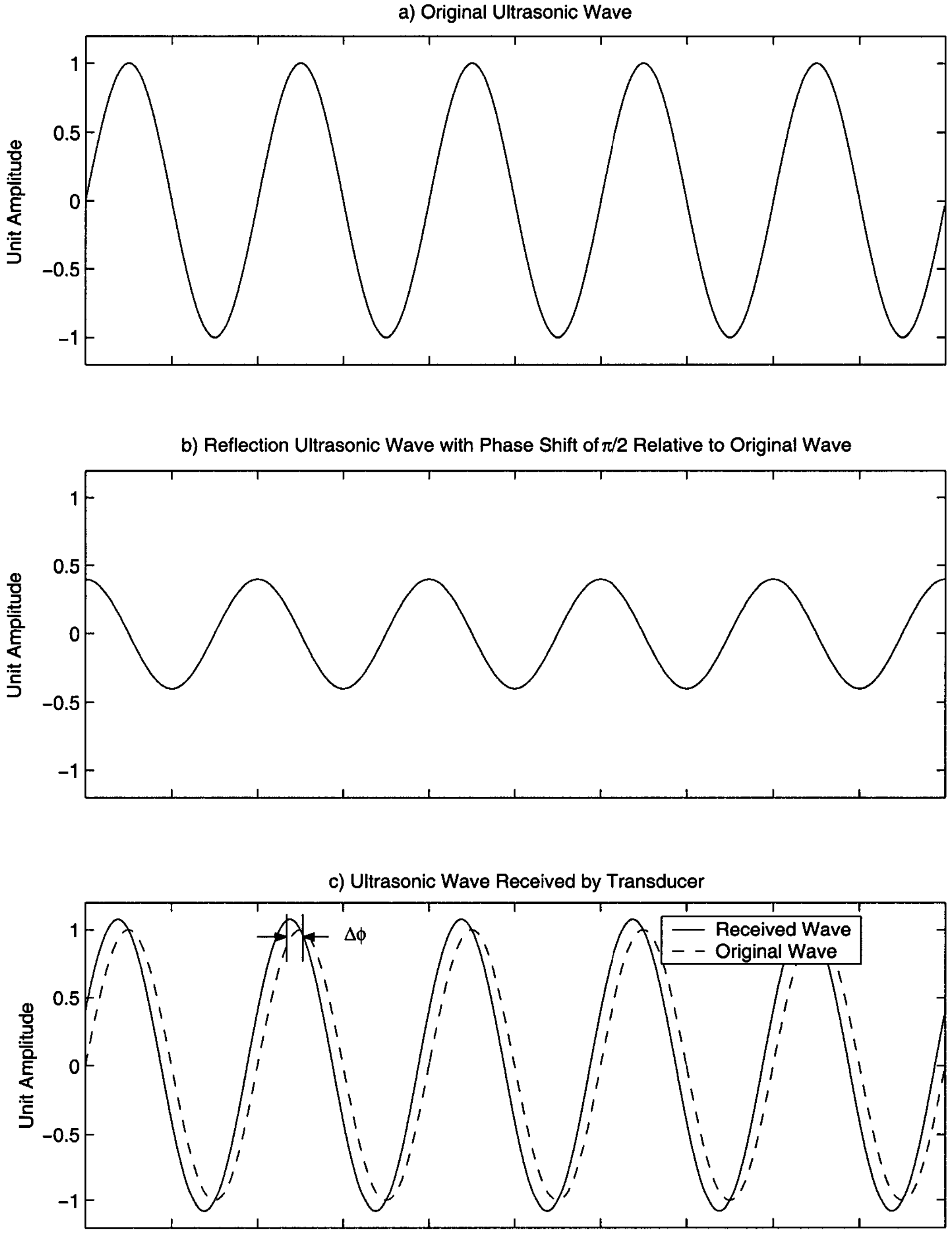

Figure 2.7: Interference of Original and Reflected Signal and the Resulting Received Signal

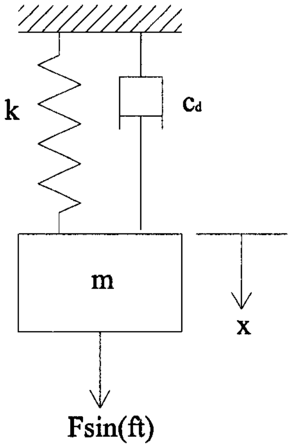

Figure 2.8: Forced Harmonic Vibration of a Damped Single Degree-of-Freedom Spring-Mass System

2.5.2 Transducer Resonant Frequency Deviation as a Source of Uncertainty

Another cause of uncertainty in the DAWPD method is resonant frequency deviation of the ultrasonic transducers. The excitation of the transmitting transducer and the reception of the ultrasonic signal by the receiving transducer is analogous to the forced harmonic vibration of a damped single degree-of-freedom spring-mass system[13] as shown in Fig. 2.8.

The motion of this system can be described by its differential equation of motion:

$$m\ddot{x} + c_d\dot{x} + kx = F\sin(ft) \tag{2.10}$$

where m is the mass, k is the spring constant, c_d is damping constant, x is the displacement, F is the amplitude of forcing function, f is the frequency of the forcing function and t is time.

Solving the differential equation of motion, a non-dimensional expression for the amplitude and phase can be found[13]. Where the amplitude, A, can be expressed as:

$$A = \frac{1}{\sqrt{[1-(\frac{f}{f_n})^2]^2 + [2\zeta(\frac{f}{f_n})]^2}} \tag{2.11}$$

and the phase, ϕ, can be shown to be:

$$\phi = \tan^{-1}\left(\frac{2\zeta(\frac{f}{f_n})}{1-(\frac{f}{f_n})^2}\right) \tag{2.12}$$

where f_n is the natural frequency of the system and ζ is the damping factor which is defined as the ratio of the damping constant, c_d, to the critical damping constant, c_c. Note that the amplitude and the phase are only functions of the frequency ratio, $\frac{f}{f_n}$ and the damping factor, where a frequency ratio of 1 is the resonant frequency. Equations 2.11 and 2.12 can be plotted as shown in Figs. 2.9 and 2.10. From the phase diagram (Fig. 2.10) it is apparent that as the forcing frequency deviates from the natural frequency a phase change will occur which can cause error in the DAWPD method. As mentioned above the DAWPD uses ultrasonic transducers continually driven at a fixed frequency. It is known that age and temperature effects can change the resonant frequency of the transducers. If a DAWPD sensor with temperature dependant resonant frequency transducers is used in an environment where the temperature varies, then the frequency ratio will deviate. This deviation will cause an unwanted phase change in addition to the phase change caused by a change in the sound speed. To avoid this error three solutions are presented: i) using resonant frequency matching in a feed-back system, ii) using broadband (low Q_m) transducers driven away from resonance or iii) by maintaining the temperature of the transducers. These solutions will be discussed in more detail in Sec. 2.7.2.

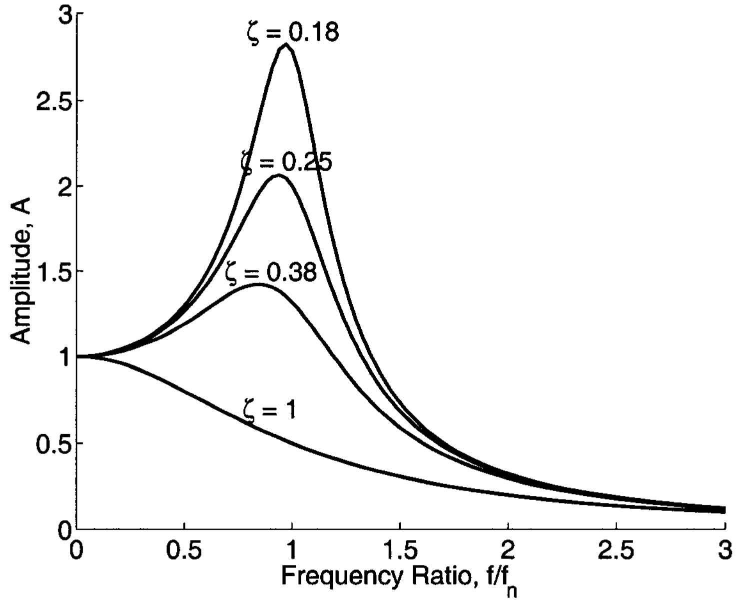

Figure 2.9: Amplitude of Vibration as a Function of the Frequency Ratio for Various Damping Factors

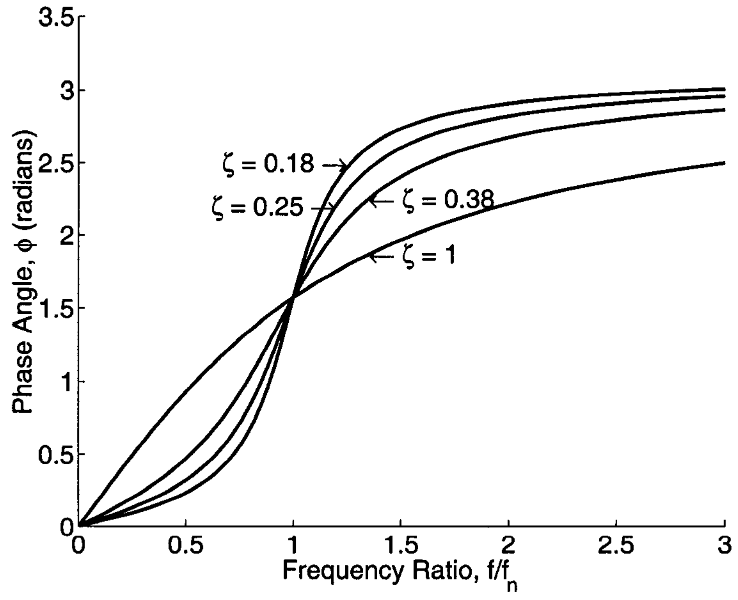

Figure 2.10: Phase of Vibration as a Function of the Frequency Ratio for Various Damping Factors

2.6 Development and Testing of Prototype Sensors

To validate the theory of the DAWPD method, experimental results are used. Two DAWPD prototypes were developed to experimentally test the theory of the DAWPD method. First, a large prototype (which will be referred to as the 'large prototype') was developed to test the effect of the aspect ratio (which is the ratio of the path length of the sensor to the transducer diameter, $\frac{d}{D}$) in a large enough volume so that wall reflections were negligible. Second, a small prototype (which will be referred to as the 'small prototype') was developed to test sensor performance when the path length was on the order of one wavelength.

2.6.1 Experimental Set-Up

Two experimental set-ups were used to determine the performance of the large and small prototypes. The first set-up was used to vary the composition of the gas entering the prototype sensors at a fixed temperature and the second set-up was used to vary the temperature of the gas in the prototype sensors.

2.6.1.1 Variable Gas Composition Experimental Set-Up

Figure 2.11 depicts the experimental set-up used to vary the composition of the gas. Two gases were fed into the Dasibi® multi-gas calibrator which contains two mass flow controllers. The Dasibi® calibrator was calibrated for the gases used in the experiments as shown in App. B. After the gases are mixed, the mixture of gases flows through the ultrasonic sensor and out into a fume hood.

The transducers in the sensor were attached to the circuitry as shown in Fig. 2.12. The driving oscillator produces a 12 V square wave which drives the transmitting transducer producing an ultrasonic signal which passes through the gas mixture. The receiving transducer receives a low level sinusoidal signal which is then amplified. The

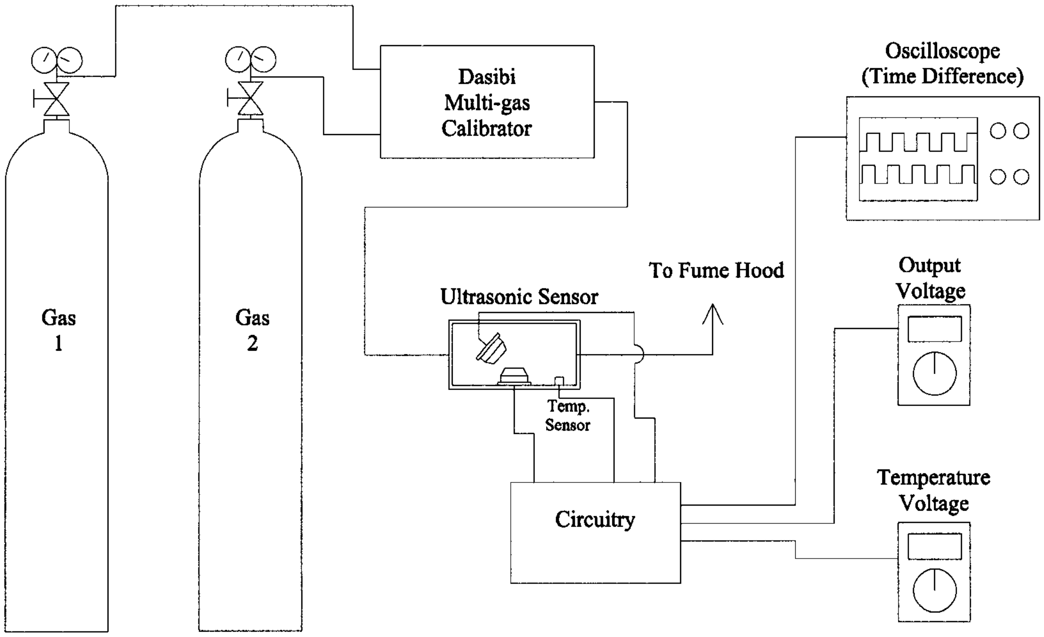

Figure 2.11: Schematic of Variable Gas Composition Experimental Set-Up

amplified signal is then transformed to a 12 V square wave by the use of Schmidt triggers. Time delay circuitry is used in conjunction with the Schmidt triggers. The time delay circuitry can be used to vary the relative time difference between the transmit and receive wave, this allows the voltage output to be 'zero-ed' for any sound speed. The received and transmitted waveforms are sent through the XOR which produces a signal seen in Fig. 2.4. The XOR output is integrated to give a voltage proportional to the phase difference. For experimental purposes a multimeter was used to integrate the signal[a]. It should be noted that changes in duty cycle of the transmitted or received wave will cause non-linearity in the output signal. Therefore a received wave duty cycle adjustment is used to match the duty cycles of the waveforms.

The sound speed is highly dependant on temperature (see Eq. 2.1). Therefore

---

[a] Commercial multimeters using a capacitor charge circuit to measure voltage inherently integrate the input voltage over their measurement period of approximately 1/4 second

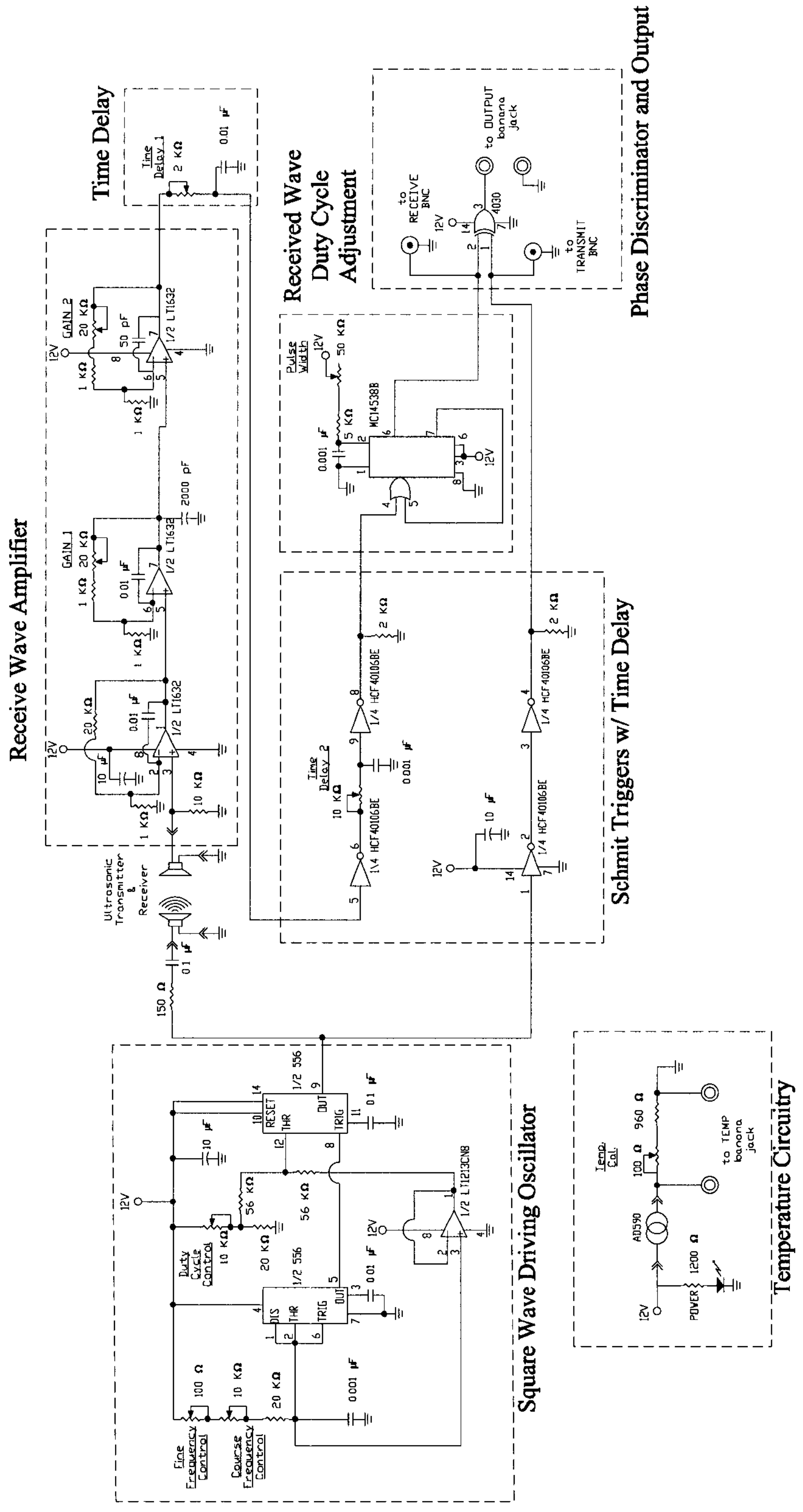

Figure 2.12: Circuitry of Prototype Sensor

temperature was measured using a fast response AD590 temperature sensor which was mounted inside the prototypes to ensure that the gas temperature did not vary. The corresponding circuitry for the temperature measurement is also shown in Fig. 2.12.

Sensor output voltage, temperature voltage and time difference data were collected by passing various gas mixtures of nitrogen, methane and hydrogen. By displaying the transmit and receive signals on the oscilloscope the time difference could be measured manually.

2.6.1.2 Variable Temperature Experimental Set-Up

Figure 2.13 depicts the experimental set-up used to vary the temperature of the sensor and the gas measured. The prototype was placed in the enclosure with the prototype circuitry (same as above) outside of the enclosure. A 1500 W heat gun (Steinel HL1802E) was used to slowly increase the temperature of the air inside the enclosure.

Sensor output voltage, temperature and time difference data, driving frequency of the transducers and received wave amplitude voltage was recorded as the temperature of the air increased.

The amplitude of the received wave was measured from pin 1 of the LT1632 amplifier (see Fig. 2.12). The signal from pin 1 is an amplified and rectified signal of the received wave. This signal was fed into a voltmeter which integrates the signal. Therefore, the voltmeter reading is proportional to the amplitude of the received wave.

2.6.2 Proof of Concept Results

The concept of the DAWPD measurement method was tested by using a mixture of gases to produce a measurable sound speed change. As discussed above, reflections within the sensor can theoretically be a major source of error in the DAWPD method.

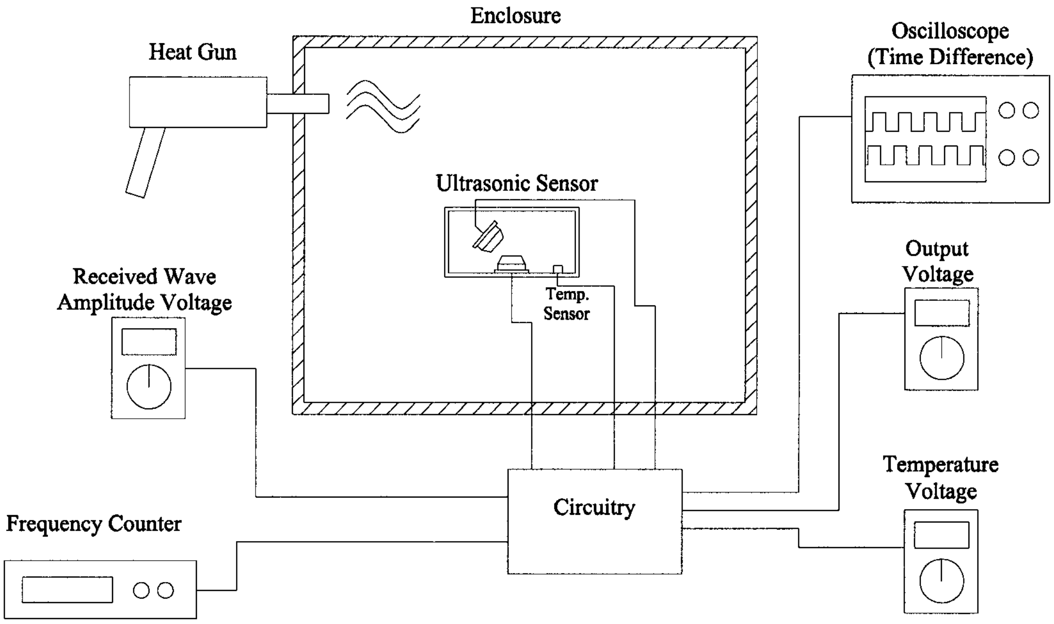

Figure 2.13: Schematic of Variable Temperature Experimental Set-Up

Experimental data proves that reflections within the sensor is a major cause of error. Typical experimental results are shown where reflections (and error) are minimized, and where reflections cause major error in the sensor.

2.6.2.1 Experimental Results with Minimal Reflections

Typical experimental results for one of the prototype sensors are seen in Figs. 2.14 and 2.15 where the reflections within the sensor are small. Various mixtures of nitrogen and hydrogen were used to produce varying sound speeds. Figure 2.14 shows the time difference between the transmitted and received signal for various sound speeds. Experimentally, the time difference can be determined by measuring the time difference between the transmitted and received waves on an oscilloscope. Theoretically, the time difference can be found by solving Eq. 2.8 for the phase difference

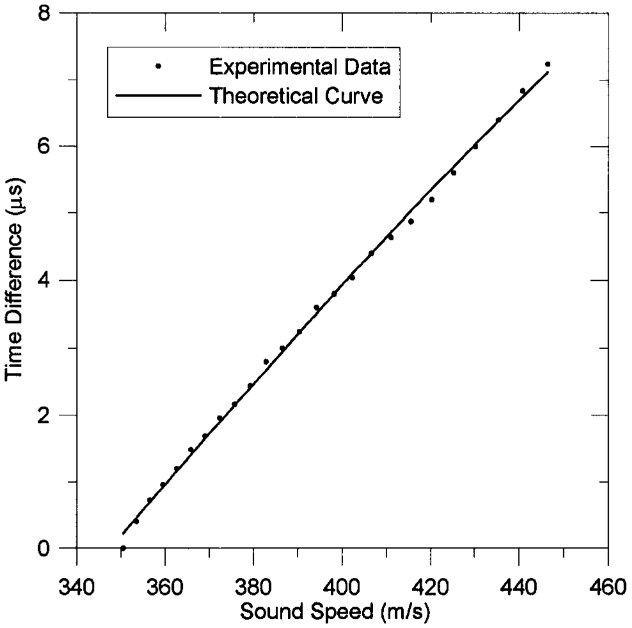

Figure 2.14: Typical Experimental Results of Prototype With Minimal Reflections Compared to Theoretical Curve

and knowing that the phase difference is related to the time difference by:

$$\Phi = \frac{\phi}{2\pi f} \tag{2.13}$$

With this equation the experimental data can be compared to the theoretical curve as shown in Fig. 2.14. The correlation coefficient between the experimental and theoretical curve was found to be 0.9995, which shows that there is a strong correlation between the data and theory.

Figure 2.15 shows the calibration curve for the sensor. The curve is fit with a second order polynomial which matches the order of the theoretical data. The correlation coefficient is found to be 0.9987 which shows that the deviation from the calibration curve is small. In fact, the maximum error from the calibration curve is 0.84% of reading.

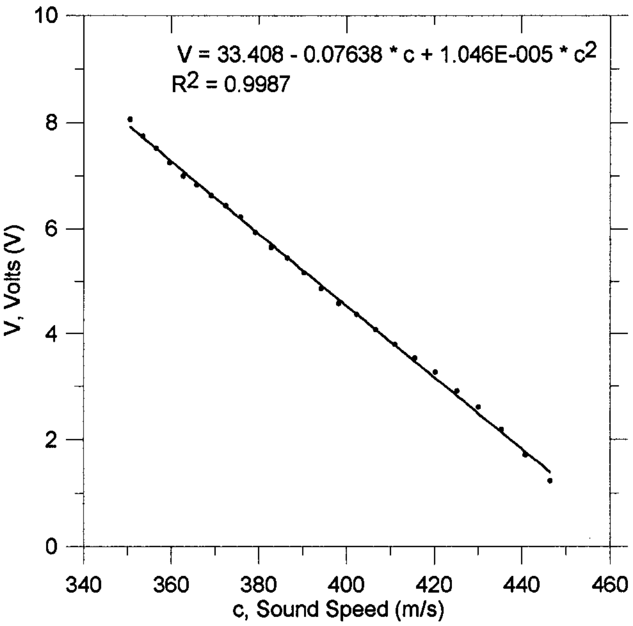

Figure 2.15: Typical Calibration Curve of Prototype With Minimal Reflections

2.6.2.2 Experimental Results with Reflections Causing Error

Experimental results support that reflections within the sensor is a major cause of sensor error. Figure 2.16a shows a calibration curve of a prototype sensor. The calibration curve from Fig. 2.16a shows that there is considerable error from the 'best-fit' curve. Figure 2.16b shows that the peak-to-peak amplitude of the received signal increases and decreases as the sound speed changes. The amplitude change is due to the constructive and destructive interference of the original ultrasonic wave and other reflected sound waves. Figure 2.16c shows that the error from the calibration signal is related to the deviation from the average amplitude. Recall that the amplitude of the received wave will be a maximum when the original wave and the reflected wave are in phase and likewise the amplitude will be a minimum when the waves are $n\pi$ radians out of phase (see Sec. 2.5.1). At these two points the phase change, and therefore the error due to reflections, will be zero. By the same logic, the error due to reflections will be a maximum when the amplitude of the received wave is at its average value. This can be seen in Fig. 2.16c, at values of $c \approx 365$ m/s and 410 m/s, where the amplitude of the received signal is near its maximum and minimum value and the error from the calibration curve is near zero.

To increase the accuracy of the sensor it is desired to reduce the ultrasonic reflections within the sensor which affect the phase of the received signal. Ideally the reflections would be eliminated or reduced in intensity so that a desired sensor accuracy could be achieved.

The intensity of a reflected signal is decreased by three factors: i) loss due to molecular absorption, ii) loss due to the distance from the ultrasonic source and iii) loss due to the reflection from the wall. The intensity of a reflected ultrasonic signal, I, can be shown to be[14]:

$$I = I_o \times \underbrace{\alpha_r}_{\text{Reflection Loss}} \times \underbrace{e^{-\alpha l}}_{\text{Absorption Loss}} \times \underbrace{\frac{1}{4\pi l^2}}_{\text{Distance Loss}} \tag{2.14}$$

where I_o is the intensity of the original wave, α is the absorption coefficient of the gas, l is the distance traveled by the ultrasonic wave and α_r is the reflection coefficient such that,

$$\alpha_r = \left(\frac{Z_2 - Z_1}{Z_1 + Z_2}\right)^2 \tag{2.15}$$

where Z_1 and Z_2 are the acoustic impedance of the gas and the wall, respectively. If Z_1 and Z_2 are on the same order of magnitude then α_r will be very small, thereby reducing the intensity of the reflected wave. The acoustic impedance of air (which has a similar impedance to the gases used in the experiment) and aluminum (the material of both prototypes) is approximately 430 $\frac{\text{kg}}{\text{m}^2\text{s}}$ and $1.7 \times 10^7 \frac{\text{kg}}{\text{m}^2\text{s}}$, respectively. The intensity of the reflections will be relatively large inside the prototypes causing error. Therefore, adding an acoustic insulation, such as Kaowool®, which has a lower impedance, will reduce the intensity of the reflected waves.

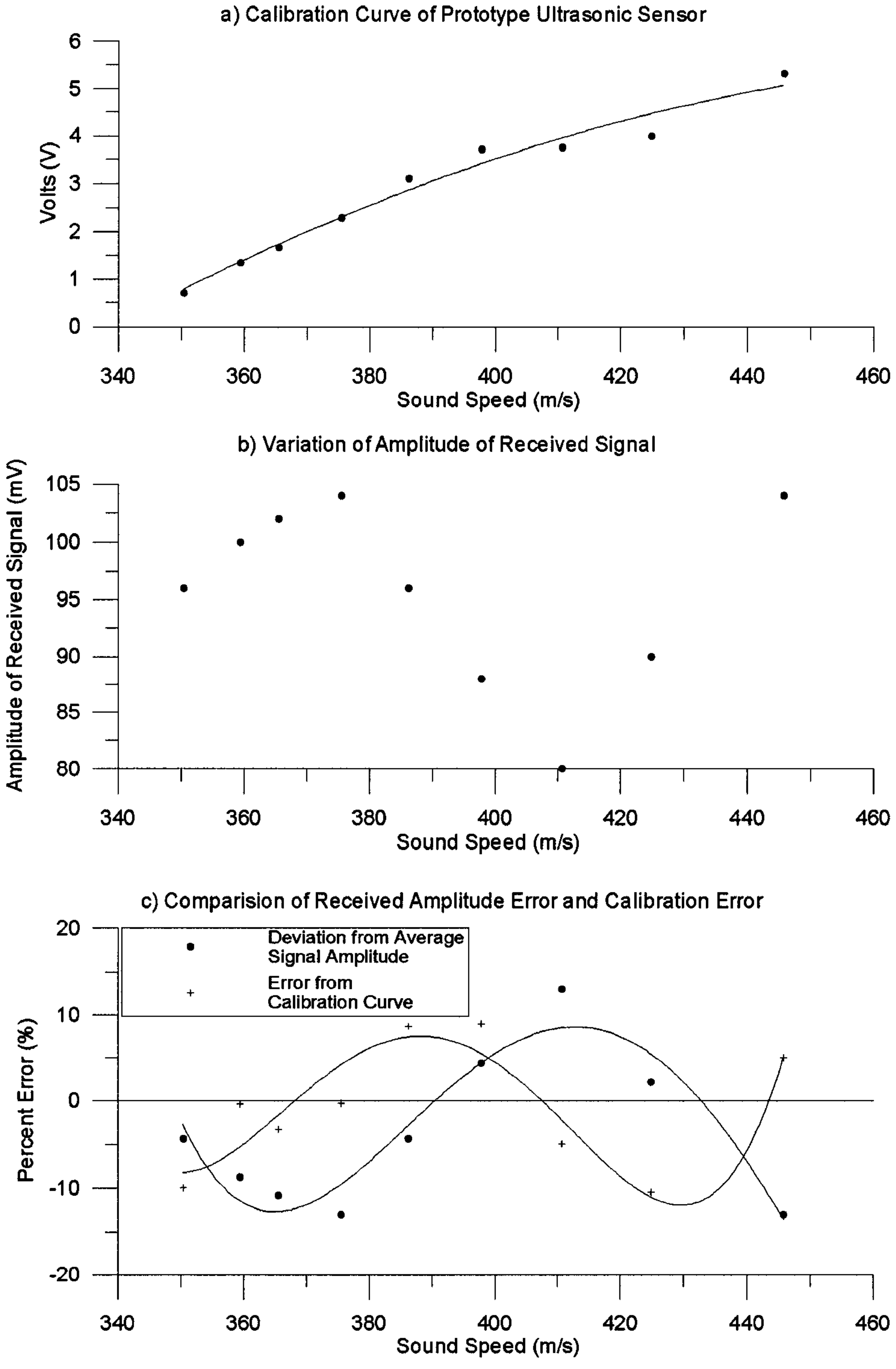

a) Calibration Curve of Prototype Ultrasonic Sensor

b) Variation of Amplitude of Received Signal

c) Comparision of Received Amplitude Error and Calibration Error

Figure 2.16: Comparison of Error from Calibration Curve and Amplitude of Received Signal

2.6.3 Large Prototype Design: Aspect Ratio of Sensor

The large prototype was designed to find a suitable aspect ratio for sensor development, where the aspect ratio is the ratio of the path length over the transducer diameter, or $\frac{d}{D}$. It will be shown that ultrasonic reflections can come from two sources: i) reflections between the transducers and ii) reflections from the walls of the sensor. By adjusting the aspect ratio the intensity of the reflections between the transducers will change. To study the effects of changes in aspect ratios and reflections between the transducers, the large prototype was designed so that the reflections from the walls of the sensor would be minimal. Therefore the large prototype was developed so that the distance from the walls of the sensor to the transducers was large compared to the path length.

The large prototype (as seen in Fig. 2.17) has exterior dimensions of 90 mm x 155 mm x 205 mm. The inside of the enclosure was insulated with 10 mm thick Kaowool® acoustic insulation to minimize the ultrasonic reflections from the sides of the enclosure. The path length, d, between the transducers can be adjusted by adding shims between the transducers mounts and the enclosures' walls. Detailed drawings of the prototype can found in App. D.

Large and small piezoelectric transducers were used for this prototype. The transducers were mounted on similar transducer mounts so that the transducers were interchangeable. The large transducers (Panasonic # EFR-RQB40K5 and EFR-TQB40KS) had an effective diameter, D, of 10 mm, while the small transducers (SensComp # 40KT08 and 40KR08) had an effective diameter of 8.4 mm.

To show that reflections between transducers cause error in the sensor, measurements were taken in the large prototype which has acoustic insulation to minimize reflections from the walls. The results are shown in Fig. 2.18. The plot compares path length to correlation coefficient, R^2. The correlation coefficient is a measure

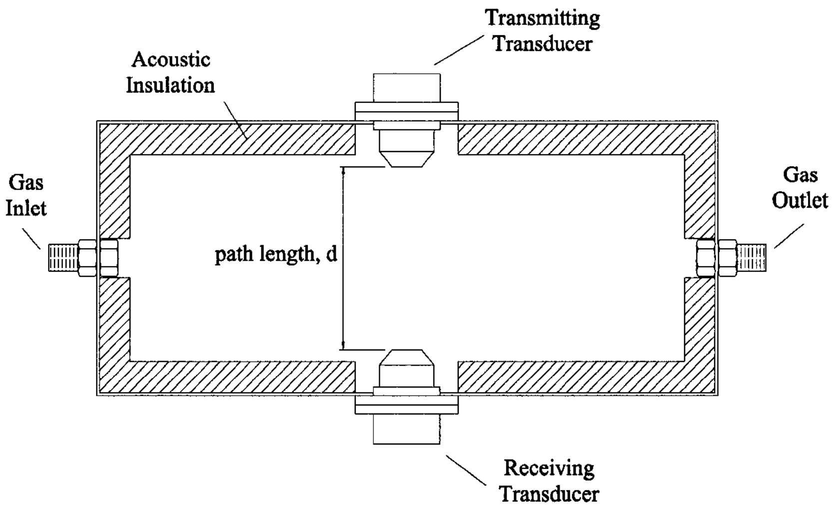

Figure 2.17: Schematic of Large Prototype of Ultrasonic Gas Sensor

of the error in representing the data by a horizontal line through the centroid. A correlation coefficient of 1 means that the 'best-fit' line is an exact representation of the data. Therefore, a correlation coefficient close to 1 means there is little scatter from the calibration curve, which means that the error is small.

To find the correlation coefficient for each path length, various sound speeds were measured with the sensor at each path length and the measurements were plotted, from which the correlation coefficient could be calculated.

Figure 2.18 shows that at short path lengths the accuracy of the sensor is poor, as the distance between the transducers increases the error of the sensor decreases. This would suggest that the error is caused by reflections between the transducers. This agrees with theory, since as the distance increases, the intensity of the reflected wave, and therefore the error, will be proportionally smaller compared to the original ultrasonic wave, as seen in Eq. 2.14.

Since reflections between transducers cause error, it is desirable to reduce the error. The error can be reduced by decreasing the size of the ultrasonic sensors, which reduces the size of the reflecting surface so that the energy of the reflected wave is

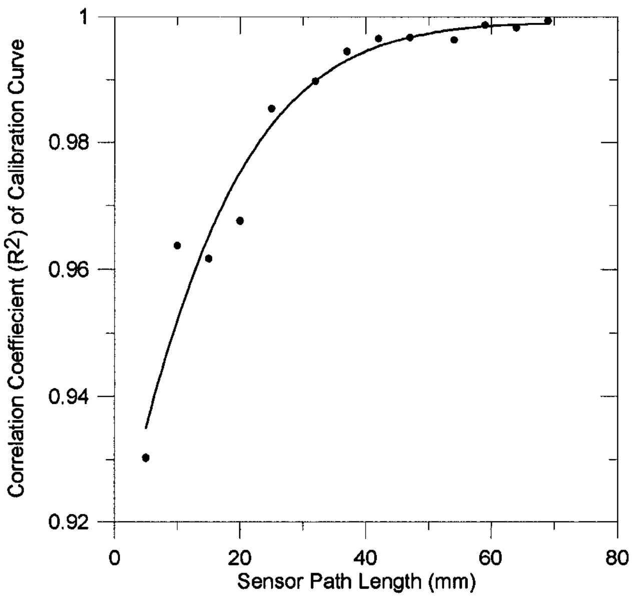

Figure 2.18: Variation of Correlation Coefficient with Sensor Path Length (Large Prototype with Large Transducers)

reduced. Due to a limit of commercially available ultrasonic transducers, only two transducer diameters were tested. The large transducer has an effective diameter of 10 mm and the small transducer has an effective diameter of 8.4 mm. Figure 2.19 shows that the smaller transducers produce less error than the large transducers at short path lengths where the reflections between transducers are strong.

As mentioned above, the path length and the transducer diameter both affect sensor error. The aspect ratio can be used to show which ratio of path length and diameter will result in an adequate sensor. Figure 2.20 shows the correlation coefficient for various aspect ratios. From the plot it is apparent that an aspect ratio greater than approximately 6 no longer results in an increase in accuracy. Thus for design purposes an aspect ratio greater than 6 should be used.

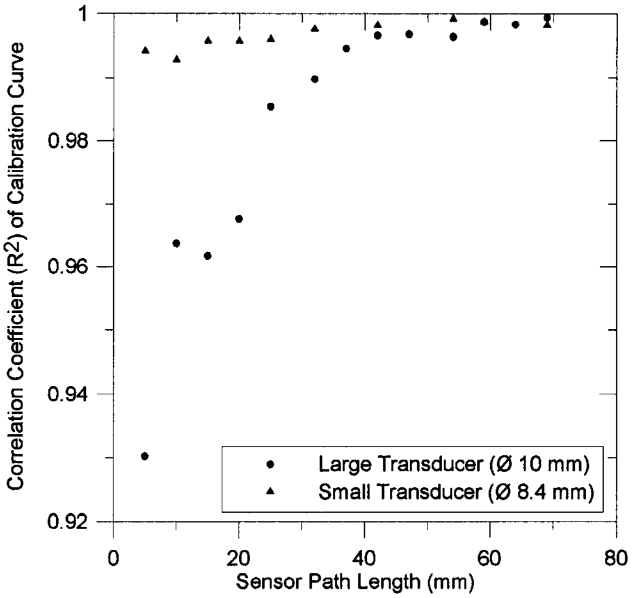

Figure 2.19: Variation of Correlation Coefficient with Diameter of Transducers (Large Prototype with Large and Small Transducers)

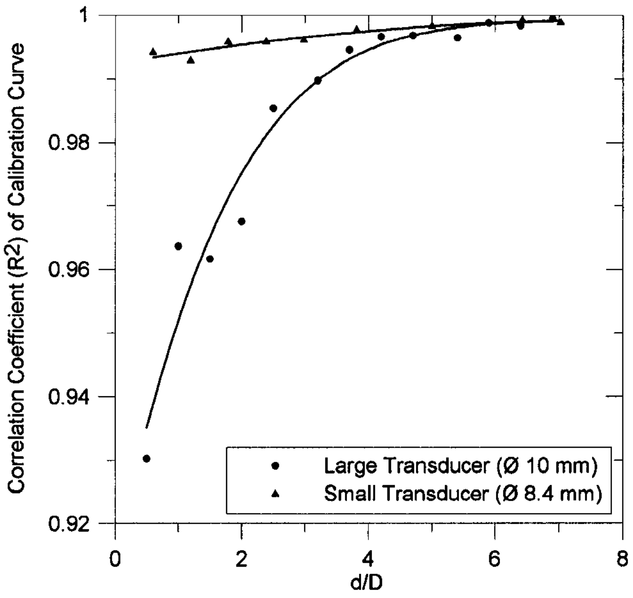

Figure 2.20: Variation of Correlation Coefficient with Large and Small Transducers (Large Prototype)

2.6.4 Small Prototype Design: Path Lengths on the Order of One Wavelength

The large prototype showed that at a suitable aspect ratio, with minimal wall reflections, a desirable accuracy could be reached. The small prototype was developed to show that suitable sensor accuracy could also be achieved with path lengths on the order of one wavelength and with walls at close distances. This sensor accuracy can be achieved by reducing the intensity of the reflections: i) from the walls of the sensor and ii) between the transducers. It will be shown that by adding acoustic insulation, reflections from the sides of the walls can be reduced considerably. Also by angling and offsetting the transducers the reflections between the transducers can be reduced.

The small prototype (with exterior dimensions of 57 mm x 92 mm x 47 mm) was developed with more adjustable parameters as seen in Fig. 2.21. The prototype is designed to be adjustable in angle, offset and normal distance. The angle between the two piezoelectric transducers can be adjusted by rotating the receiving transducer mount in the slot. The offset distance can be adjusted by moving the receiving transducer mount along the transverse slot. Finally, the normal distance can be adjusted by adding shims to the transmitting transducer mount. Kaowool® acoustic insulation, 10 mm thick, was installed on the inside of the box to dampen acoustic reflections. Detailed drawings of the prototype can found in App. C.

To study the effects of wall reflections, prototype performance was measured with various amounts of acoustic insulation. The prototype was tested with no acoustic insulation and then tests were repeated by adding insulation to one wall at a time. Figure 2.22 shows the effect of adding acoustic insulation to the inside of the small prototype. The correlation coefficient increases as more sides of the prototype are covered with acoustic insulation. This shows that as more insulation is added to the walls the accuracy of the prototype increases. This suggests that the intensity of the

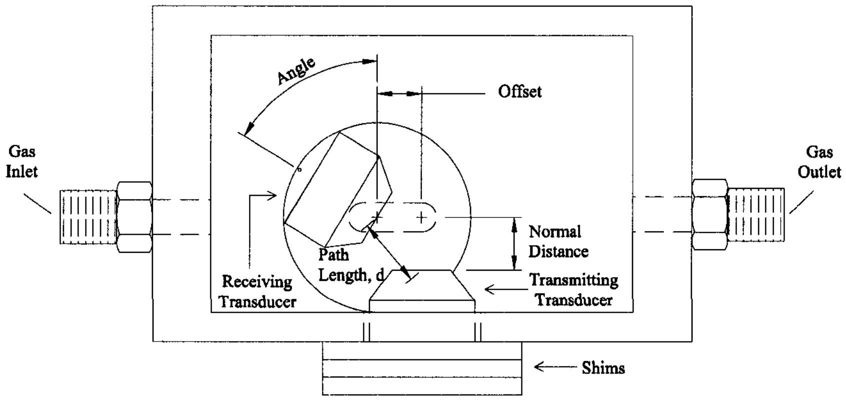

Figure 2.21: Schematic of Small Prototype of Ultrasonic Gas Sensor

reflected waves from the walls have decreased.

To minimize the reflections between the transducers at path lengths on the order of one wavelength, different transducer arrangements can be used: i) angling the transducers and ii) offsetting the transducers.

By angling the transducers, reflections off the receiving transducers will not be reflected directly back to the transmitting transducer, therefore the error due to reflections will be smaller. Figure 2.23 shows that as the angle between the transducers increases, the error decreases. For this particular prototype and transducers, increasing the angle to approximately 40° - 60° resulted in increased accuracy compared to the sensor with an angle of 0° between transducers. However, increasing the angle between the transducers too drastically resulted in poor accuracy. A high angle between the transducers will result in the receiving transducer being less sensitive to the direct ultrasonic wave, and more sensitive to a reflected wave from the walls of the sensor, thereby increasing the error.

Reflections between transducers can also be reduced by offsetting the distance between the transducers. Similar to angling the transducers, offsetting the transducers

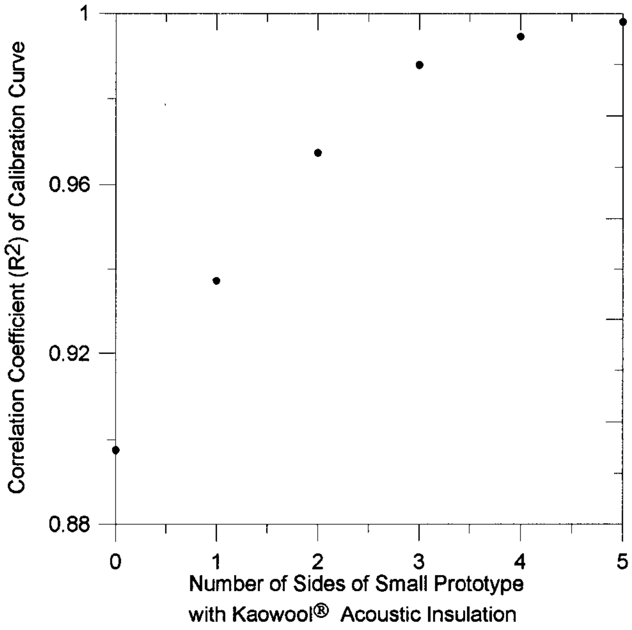

Figure 2.22: Variation of Correlation Coefficient with Acoustic Insulation (Small Prototype with Large Transducers at 8 mm normal distance, 0 mm offset and 70° angle)

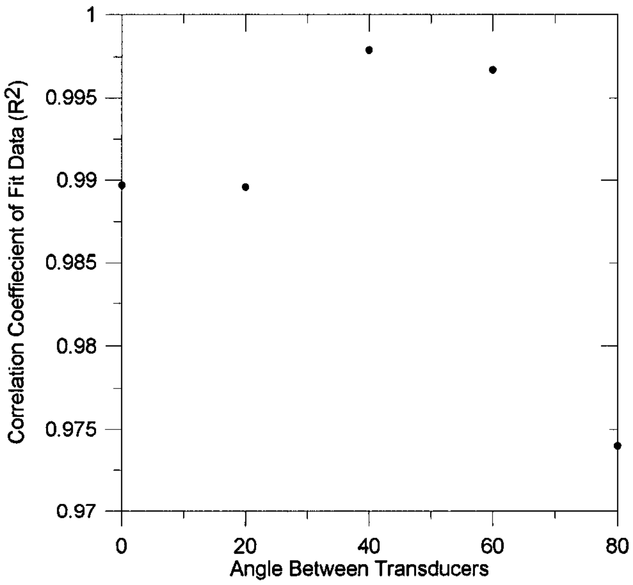

Figure 2.23: Variation of Correlation Coefficient with Angle Between Transducers (Small Prototype with Large Transducers at 8 mm normal distance)

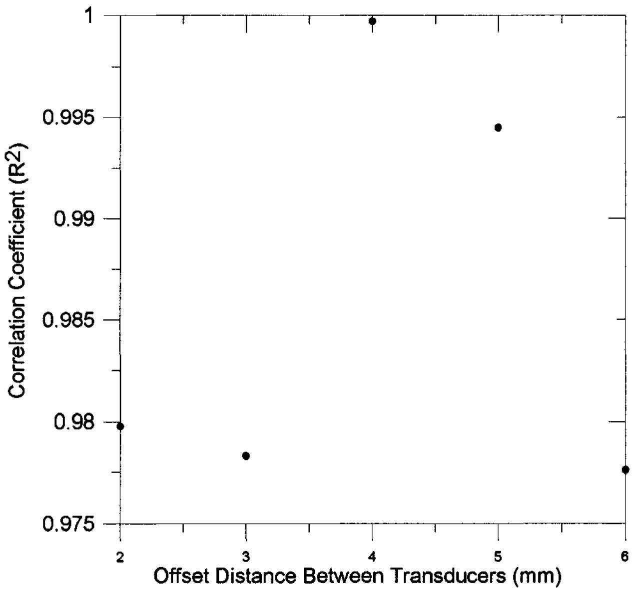

Figure 2.24: Variation of Correlation Coefficient with Offset Between Transducers (Small Prototype with Large Transducers at 8 mm normal distance and 70° angle)

results in the reflections off the receiving transducer to be reflected away from the transmitting transducer. Figure 2.24 shows that the offset distance between transducers affects the error in the sensor. For this particular prototype and transducers, small offsets of 2 - 3 mm resulted in little to no effect on the error of the sensor. However, slightly larger offsets of 4 - 5 mm resulted in less error. Also, like angle effects, large offsets eventually result in higher error due to decreased sensitivity to the direct ultrasonic wave.

2.6.5 Transducer Resonant Frequency Temperature Dependance

The temperature variation experiment was used to show that resonant frequency temperature dependant transducers can cause error in the DAWPD method. It will be shown that: i) the transducers used in the prototypes are resonant and their resonant frequency is temperature dependant, ii) temperature variations with temperature dependant resonant transducers can cause major errors and ii) using resonant frequency matching these errors can minimized.

The small prototype with the large transducers (Panasonic # EFR-RQB40K5 and EFR-TQB40KS) was used to test the resonant characteristics of the transducers and the effects of temperature on the transducer and the sensor. The small prototype was configured with an 8 mm normal distance, 4 mm offset and a 70° angle to ensure that error due to reflections was minimized.

The resonant characteristics of the transducers were tested by varying the driving frequency at constant temperature. The amplitude and the time difference (which is proportional to phase difference) for each frequency was recorded. Figure 2.25 shows the frequency response curve for the pair of transducers. From this figure it is apparent that these transducers are highly resonant since the amplitude decay from resonance is so steep. The quality of resonance can be described by the mechanical 'Q' factor, Q_m , which can be defined by the relation[15]:

$$Q_m = \frac{f_n}{f_2 - f_1} \tag{2.16}$$

where f_1 and f_2 are the frequencies on each side of f_n where the amplitude is equal to $\frac{1}{\sqrt{2}}$ of the maximum amplitude which occurs at f_n. From Eq. 2.16 it can be shown that Q_m for the transducers used was 115, which is relatively high. The transducers used are of the piezoceramic variety, which are known to have high Q_m factors compared to other kinds of ultrasonic transducers[12]. MEMS (Micro-Electro-Mechanical System) transducers have been made which have a broader bandwidth, these transducers have been known to have Q_m factors of approximately 10[16,17]. Transducers with large bandwidths have the advantage of being able to operate at a wider range of frequencies away from the resonant frequency.

Another important transducer characteristic is the phase angle response curve. As mentioned in Sec. 2.5.2 driving the ultrasonic transducers away from the natural

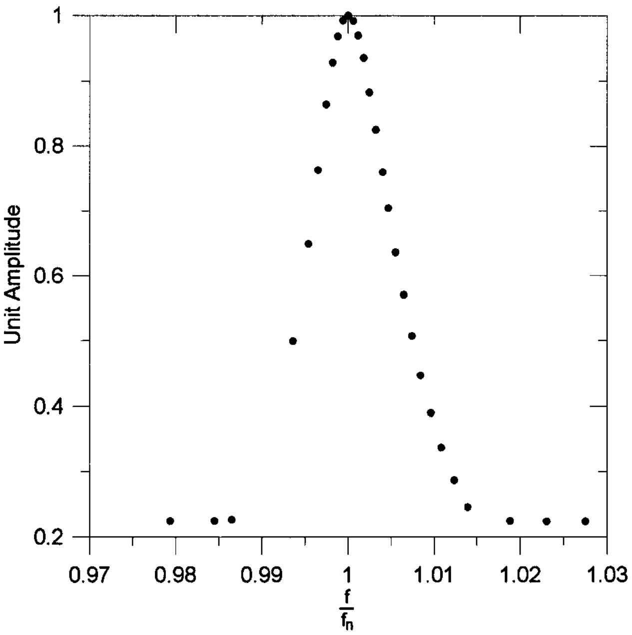

Figure 2.25: Frequency Response Curve for Large Transducers (T=23.6°C)

frequency will cause an undesirable change in phase. Figure 2.26 shows the variation of the time difference (which is proportional to phase difference) of the transducers with a change in driving frequency. The slope of the curve near resonance is steep, suggesting that a small deviation from the resonant frequency will result in a large error. It should be noted that measurements with the prototype sensor is on the order of microseconds, and from the figure it is apparent that even a small change in frequency will cause a phase change of many microseconds. This will result in errors on the same order of magnitude as the measurement if the driving frequency deviates from the resonant frequency of the transducers.

The transducers' resonant frequency dependance on temperature was tested using the experimental set-up shown in Fig. 2.13. The natural frequency of the transducers was found over a range of temperatures (the transducers tested have an operable temperature range of -20 to 60°C) and is shown in Fig. 2.27. The figure shows that the resonant frequency decreases with an increase in temperature. Therefore, there is

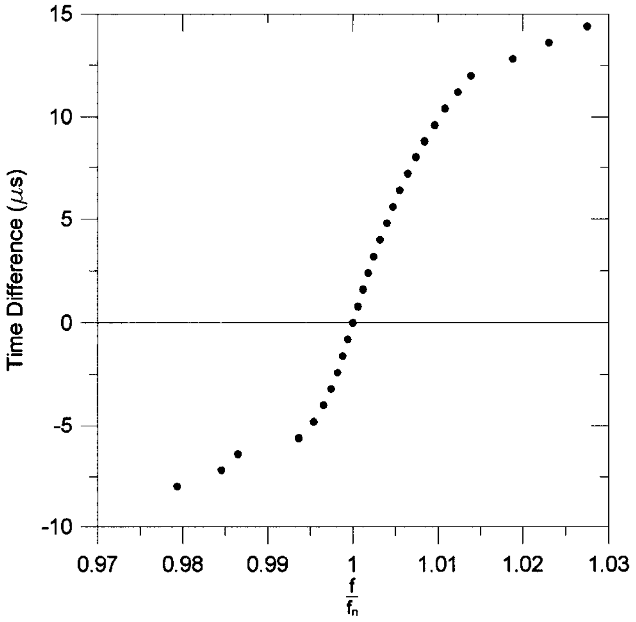

Figure 2.26: Phase Angle Response Curve for Large Transducers (T=23.6°C)
(For 40 kHz driving frequency, ϕ(radians) = 0.251 × Φ(μs))

a strong temperature dependance on the resonant frequency of the transducers tested. This would suggest that temperature measurements made with these transducers would have substantial error.

The error caused by these temperature dependant transducers can be seen by measuring the time difference with an increase in temperature. Recall from Eq. 2.1 that an increase in temperature will cause an increase in the sound speed. For a DAWPD sensor an increase in the sound speed will result in a decrease in the time difference. Figure 2.28 shows the experimental time difference recorded by the sensor and the theoretical time difference which would be expected from the sensor. It is apparent that the experimental data without resonant frequency matching does not correspond to the theoretical curve. The cause of this is due to the resonant frequency change of the transducer as the temperature increases. With the current prototype the frequency ratio, $\frac{f}{f_n}$, will change with temperature since the driving frequency is

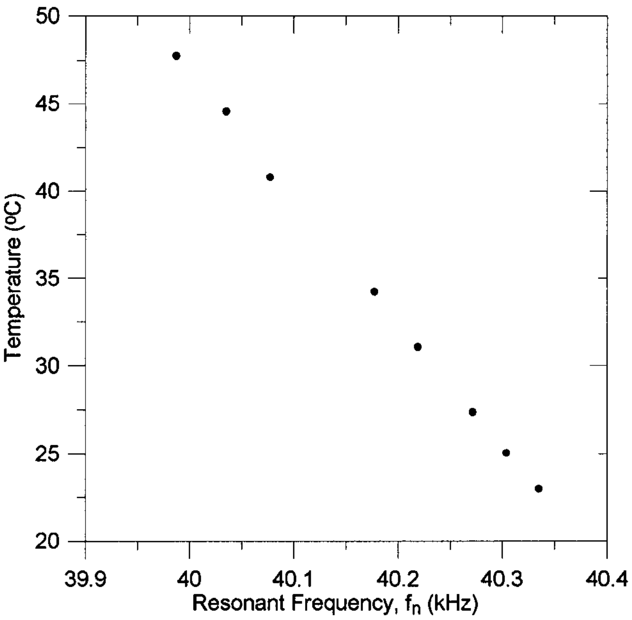

Figure 2.27: Resonant Frequency Temperature Dependance of Large Transducers

held constant as the natural frequency changes. This will cause a phase difference in the sensor as shown in the phase angle response curve (Fig. 2.26). This phase difference between the transducers causes the transmitted and received signals to shift relative to each other causing measurement error.

One method of reducing this error is to change the driving frequency of the transmitting transducer to match the resonant frequency of the transducer pair. By matching the driving and the resonant frequency the frequency ratio will remain constant, which will ensure that the phase angle between the transducers remains constant, substantially reducing the error in the system.

Experimentally, the frequencies can be matched by varying the 'fine frequency control' potentiometer in the prototype circuitry (see Fig. 2.12) until the amplitude of the received signal is a maximum. The amplitude of the received wave can be read from the 'Received Wave Amplitude' voltmeter (see Fig. 2.13). However, matching the resonant and the driving frequency can be difficult due to inadequate resolution of

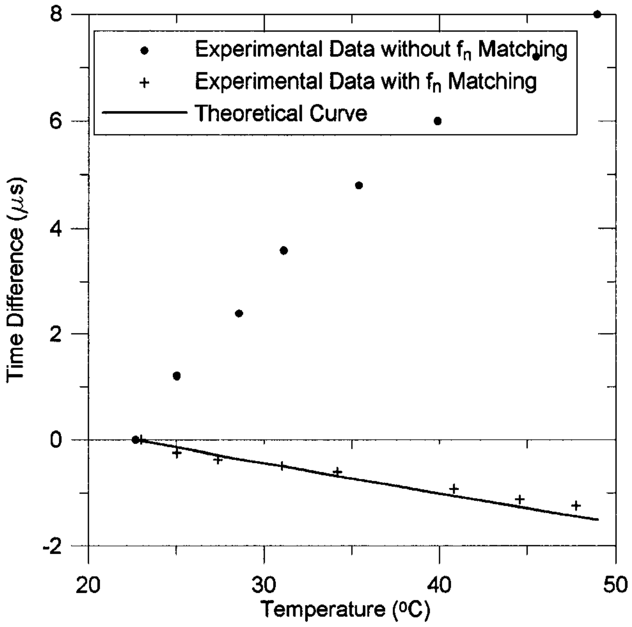

Figure 2.28: Comparison of Experimental Data with and without Resonant Frequency Matching to the Theoretical Time Difference of Sensor Output with Temperature Variation

the amplitude measurement. This difficulty can be seen in Fig. 2.29. The figure shows the received wave directly from the ultrasonic transducer (Fig. 2.29a). The received wave is then amplified and rectified (Fig. 2.29b). This rectified signal is integrated by a voltmeter (Fig. 2.29c) which gives a voltage proportional to the amplitude of the received wave. Matching the frequency with this system can be difficult since a small frequency change will cause a large time difference and a relatively small change in the measured amplitude voltage. A higher resolution amplitude measurement system would allow for more accurate frequency matching.

Figure 2.28 compares the experimental data with and without resonant frequency matching to the theoretical curve. It is clear that matching the frequency greatly increases the accuracy of the sensor, although there is still scatter about the theoretical curve. The cause of the data scatter is most likely to inaccurate frequency matching as mentioned above.

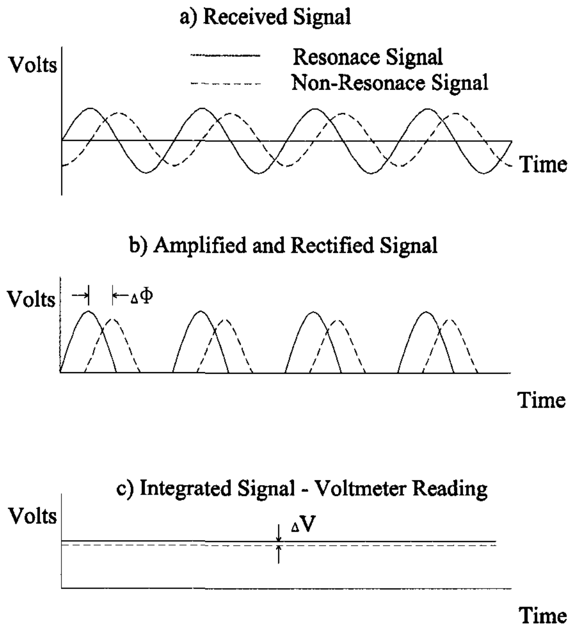

Figure 2.29: Received Wave Amplitude Measurement Method

2.7 Design Guidelines

The goals of this project are to design a micro-sensor to measure sound speeds in gases with adequate accuracy for various automotive applications. Design guidelines are needed so that these goals can be met. These design guidelines will give equations to specify required sensor parameters such as: transducer diameter, sensor path length and driving frequency. Suggestions will be given for reducing the size of the sensor enclosure and for reducing error due to temperature effects.

2.7.1 Sensor Parameters - Frequency, Diameter and Path Length

As mentioned above, one goal of this project is to design a micro-sensor to measure sound speeds of gas mixtures. A micro-sized ultrasonic transducer is needed to make a sound speed micro-sensor. MEMS ultrasonic transducers have been made[16–18], however none are currently commercially available. Design guidelines are needed so that the current sensor technology can be scaled down when micro-transducers become available. The needed design parameters of a micro-sensor are: driving frequency (f), transducer diameter (D) and path length between transducers (d).

The sensor should be designed for a particular range of sound speeds, c_1 and c_2, and for a particular distance in which the sensor should fit into, d. The discrete acoustic wave and phase detection method has been shown to be useful for small path lengths. Therefore, the driving frequency which has maximum sensitivity can be found by solving Eq. 2.9 for frequency:

$$f = \frac{\frac{\theta}{2\pi}}{d(\frac{1}{c_1} - \frac{1}{c_2})} \tag{2.17}$$

where the phase range, θ, is determined by the circuitry used, however, for the prototype demonstrated the phase range is π radians.

Experimentally it was found that reflections from walls and between transducers was a major cause of error in the sensor. It was also shown that for larger path lengths the aspect ratio could be used to design a sensor with suitable accuracy. Figure 2.20 showed that a suitable aspect ratio is:

$$\frac{d}{D} \approx 6 \tag{2.18}$$

For larger $\frac{d}{D}$, the error due to reflections between the transducers is small. This relation (Eq. 2.18) is assuming that the reflections from the walls is small and the transducers are not angled or offset relative to each other.

To design a sensor on the order of a wavelength it was shown that reflections from the walls can be reduced with acoustic insulation and reflections between sensors can be reduced by: i) angling the transducers, ii) offsetting the transducers and iii) using smaller diameter transducers. Angling or offsetting the transducers can be

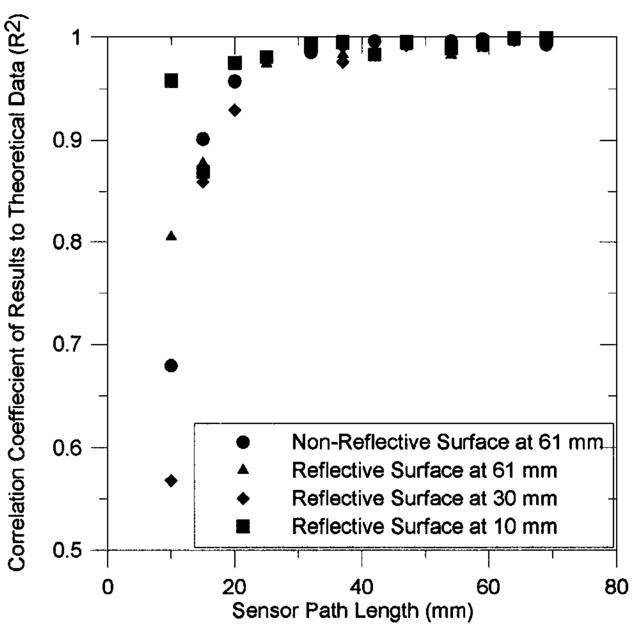

Figure 2.30: Variation of Theoretical Correlation Coefficient with Reflective Surfaces at Various Distances (Large Prototype with Large Transducers)

used to design a sensor with a smaller path length relative to the sensor diameter. However, it is simpler for scaling and design purposes to avoid angling and offsetting the transducers unless a smaller path length is needed relative to the transducer diameter.

As mentioned above, the wall reflections can be reduced by using acoustic insulation, however, an experiment was performed to determine how reflective surfaces effected the performance of the sensor. Figure 2.30 shows the performance of the large prototype sensor with a reflective surface at 61 mm, 30 mm and 10 mm. Moving the reflective surface does little to change the performance of the sensor. At close distances the error is caused by reflections between the transducers and at farther distances the reflections from the walls travel a farther distance and the amplitude of the reflection is reduced.

2.7.2 Transducer Parameters - Temperature and Age Effects

Previously it was shown that temperature effects can cause error in the DAWPD sound speed measurement method. This error was caused by a change in the resonance frequency of the transducers as temperature changed. A similar error can be caused from resonant frequency drift with ageing. Ideally, a transducer could be found whose resonant frequency is not temperature or age dependant, however most ultrasonic transducers suffer from these effects[18-20]. These errors can be over come by various methods (or combination of methods) such as: i) using resonant frequency matching in a feed-back system, ii) maintaining the temperature of the transducers or iii) driving transducers away from the resonance frequency.

First, the DAWPD method can use feed-back resonant frequency matching to compensate for the resonant frequency changes due to aging or temperature. It was shown (Sec. 2.6.5) that by controlling the driving frequency to match the resonant frequency, temperature-dependencies could be compensated. However, it was shown that this method may not be able to match the frequencies to the desired accuracy, due to poor amplitude measurement resolution. Resonant frequency matching can also be accomplished by mapping the frequency response of the transducers to changes in temperature (see Fig. 2.27). The temperature of the transducers can be measured and the driving frequency adjusted to match the resonant frequency of the transducers (this method was used in Chapter 4). Commercially, some measurement systems have temperature-controlled oscillators or oscillators that are locked to the resonant frequency of the transducers[12,21]. Another problem with this method is that the feed-back control system would add complexity to a fairly simple measurement system.

Second, the temperature of the transducers could be maintained to stabilize the resonant frequency of the transducers. This technique has been used in the past with some success[18]. However, this method also adds complexity to the measurement system and it will not compensate for resonant frequency changes due to age.

Third, the transducers could be operated away from resonance. The advantage would be that changes in resonance frequency would not produce a large change in phase angle. Figure 2.10 shows the theoretical phase angle curve for a damped single degree-of-freedom spring-mass system. It is apparent from the figure that the slope of the phase angle curve is less steep above and below resonance. If a transducer was operated well away from resonance, then changes in the frequency ratio due to temperature or age would have little effect on the phase of the system, resulting in little error due to frequency ratio changes. MEMS devices have lower Q_m factors than piezoceramic devices, making the MEMS devices ideal candidates for a system which operated away from the resonant frequency of the transducers.

2.8 Conclusions

The purpose of this project was to develop a small ultrasonic sensor to measure the sound speed in gas mixtures. It has been shown that the discrete acoustic wave and phase detection method is a useful method for measuring sound speeds over small path lengths. This method has been shown to give predictable results which closely match theoretical results. It was also found that reflections and resonant frequency changes of the transducers are the dominate source of error in the prototype sensors.

Reflections come from two major sources: i) reflections from walls and ii) reflections between transducers. It was determined experimentally that the reflections off the walls can be reduced by using acoustic insulation on the walls. Reflections between the transducers can be reduced by: i)increasing the distance between transducers, ii) angling the transducers, iii) offsetting the transducers and, iv) decreasing the diameter of the transducers.

Resonant frequency changes are due to temperature and age effects. The error due to resonant frequency change can be reduced by: i) using resonant frequency matching in a feed-back system, ii) maintaining the temperature of the transducers or iii) driving transducers away from the resonance frequency.

Design guidelines were developed, which should be used in designing a scaled down micro-sensor. Useful equations were developed which related the path length of the sensor with the frequency and diameter of the transducers. These relations show that a suitable micro-sensor can be made with the DAWPD method.

REFERENCES

[1] S. O. Colgate, C. F. Sona, K. R. Reed, and A. Sivaraman, "Experimental ideal gas reference state heat capacities of gases and vapors," *J. Chem. Eng. Data*, vol. 35, pp. 1–5, 1990.

[2] P. Labes, J. L. Daridon, B. Lagourette, and H. Saint-Guirons, "Measurement and prediction of ultrasonic speed under high pressure in natural gases," *International Journal of Thermophysics*, vol. 15, no. 5, pp. 803–819, 1994.

[3] A. F. Estrada-Alexanders and J. P. M. Trusler, "The speed of sound and derived thermodynamic properties of ethane at temperatures between 200 K and 450 K and pressures up to 10.5 MPa," *J. Chem. Thermodynamics*, vol. 29, pp. 991–1015, 1997.

[4] E. P. Papadakis, "Ultrasonic phase velocity by the pulse-echo-overlap method incorporating diffraction phase corrections," *J. Acoust. Soc. Am*, vol. 42, pp. 1045–1051, 1967.

[5] E. Polturak, S. L. Garret, and S. G. Lipson, "Precision acoustic gas analyzer for binary mixtures," *American Institute of Physics*, vol. 57, pp. 2837–2841, 1986.

[6] G. Hallewell, G. Crawford, D. McShurley, G. Oxoby, and R. Reif, "A sonar-based technique for the ratiometric determination of binary gas mixtures," *Nuclear Instruments and Methods in Physics Research*, vol. A264, pp. 219–234, 1988.

[7] G. Hallewell, "A sound method for measurement of gas concentration," *Research and Development*, pp. 98–101, Sept 1988.

[8] J. F. Figueroa and J. S. Lamancusa, "A method for accurate detection of time of arrival: Analysis and design of an ultrasonic ranging system," *J. Acoust. Soc. Am*, vol. 91, pp. 486–494, 1992.

[9] M. Joos, H. Müller, and G. Linder, "An ultrasonic sensor for the analysis of binary gas mixtures," *Sensors and Actuators B*, vol. 15-16, pp. 413–419, 1993.

[10] J. T. Tinge, K. Mencke, L. Bosgra, and A. A. H. Drinkenburg, "Ultrasonic gas analyser for high resolution determination of binary-gas composition," *J Physics E: Scientific Instruments*, vol. 19, pp. 953–956, 1986.

[11] L. C. Lynnworth, *Ultrasonic Measurements for Process Control: Theory, Techniques, Applications.* Academic Press, Inc., 1989.

[12] W. Manthey, N. Kroemer, and V. Mágori, "Ultrasonic transducers and transducer arrays for applications in air," *Meas. Sci. Technol.*, vol. 3, pp. 249–261, 1992.

[13] W. T. Thomson and M. D. Dahleh, *Theory of Vibration with Applications.* Prentice-Hall, Inc., 1998.

[14] J. Blitz, *Fundamentals of Ultrasonics.* Butterworth and Co., 1963.

[15] J. Blitz, *Elements of Acoustics.* Butterworth and Co., 1964.

[16] P. D. Harris, M. K. Andrews, and G. C. Turner, "Ultrasonic transmission and reception from bulk-micromachined transdcuers," *IEEE Transactions on Ultrasonics, Ferroelectrics, and Frequency Control*, vol. 48, no. 1, pp. 224–231, 2001.

[17] I. Ladabaum, X. Jin, H. T. Soh, A. Atalar, and B. T. Khuri-Yakub, "Surface micromachined capacitive ultrasonic transducers," *IEEE Transactions on Ultrasonics, Ferroelectrics, and Frequency Control*, vol. 45, no. 3, pp. 678–690, 1998.

[18] L. Rufer, C. Domingues, and S. Mir, "Behavioural modelling and simulation of a MEMS-based ultrasonic pulse-echo system," in *Design, Test, Integration, and Packaging of MEMS/MOEMS 2002. Cannes, France*, pp. 171–182. Vol. 4655.

[19] M. Toda, "Cylindrical PVDF film transmitters and receivers for air ultrasound," *IEEE Transactions on Ultrasonics, Ferroelectrics, and Frequency Control*, vol. 49, no. 5, pp. 626–634, 2002.

[20] M. Hornung, O. Brand, O. Paul, and H. Baltes, "Long-term stability of membrane transducers for proximity sensing," in *SPIE Conference on Micromachined Devices and Components IV - Santa Clara, California - Sept. 1998*, pp. 251–259. Vol. 3514.

[21] Anon, "Proximity sensor using a single piezoceramic ultrasonic transducer," *IBM Technical Disclosure Bulletin*, vol. 29, no. 2, pp. 935–936, 1986.

CHAPTER 3

APPLICATIONS FOR AN ULTRASONIC GAS SENSOR - GASEOUS FUEL SENSORS

3.1 Introduction

ALTERNATIVE fueled vehicles offer a number of advantages over conventional fueled vehicles. However, the performance of alternative fueled vehicles, such as natural gas and variable gaseous fuel vehicles, can be compromised by variations in the quality of the fuel.

This chapter discusses evidence that the fuel quality of natural gas can be correlated with sound speed. It goes on to show that the discrete acoustic wave and phase detection (DAWPD) method can be used to measure the quality of the natural gas with adequate accuracy and range.

Variable gaseous fuel (VGF) vehicles are vehicles that can operate on natural gas, hydrogen, or a mixture of the two fuels, leading to a need to measure the composition of the VGF fuel mixtures. This chapter shows that the DAWPD method can be used to determine the concentration of VGF gas mixtures with adequate accuracy. However, the range of the prototype sensor tested was limited by the type of ultrasonic transducers used. It is postulated that the range of the prototype sensor could be extended by using transducers with an acoustic impedance better matched to the

VGF gas mixture.

3.2 Justification for a Natural Gas Quality Sensor

This section shows that a natural gas quality sensor can improve the performance of NGVs. It shows that the composition of natural gas is dependant on the location of the natural gas well site and also on propane peak-shaving. These changes in natural gas composition can greatly change the fuel quality properties of the natural gas. Changes in the fuel properties can negatively affect the performance of stoichiometric and lean burn NGVs. This section also shows that an acoustic natural gas quality (NGQ) sensor can be used to measure some of the fuel properties so that NGV performance can be improved.

Another similar automotive application for a sound speed sensor in to measure the quality of liquified petroleum gas (LPG) fuel. LPG fuel has significant variations in propane/butane ratio and an accurate, economical sensor could be used to improve LPG engine control systems. This application in not discussed further in this thesis.

3.2.1 Variation of Natural Gas Composition and Quality

The composition of natural gas varies through out the world and even at a single service station over time. The variation is caused by two major sources: i) location of natural gas well sites and ii) propane peak-shaving.

3.2.1.1 Well Site Location

The composition of natural gas varies from well site to well site. In general, natural gas is composed mostly of methane with the addition of heavier hydrocarbons such as ethane, propane etc., other inert gases such as carbon dioxide and nitrogen, and oxygen may also be present. The composition of natural gas can vary greatly depend-

Table 3.1: Four Classifications of World Natural Gas Compositions

	Type			
Component (% Volume)	1	2	3	4
Heavier Hydrocarbons (C_2^+)	$< 10\%$	$< 10\%$	$> 10\%$	$> 10\%$
Carbon Dioxide (CO_2)	$< 2\%$	$> 2\%$	$< 2\%$	$> 2\%$

Source: J. L. Gadon, 1987[1]

Table 3.2: World Natural Gas Reserves by Composition Outside North America

	Type			
Region	1	2	3	4
Europe	80%	9%	11%	0%
Former USSR	77%	2%	13%	8%
Africa	20%	0%	75%	5%
Middle East	0%	55%	22%	23%
Australasia	12%	21%	14%	53%
Latin America	11%	8%	54%	27%
Total	47%	15.5%	23%	14.5%

Source: J. L. Gadon, 1987[1]

ing on the geographical location of the well site. For example, the world natural gas supply can be categorized into four types as seen in Table 3.1. These categories are divided by the amount of hydrocarbons heavier than methane and by the amount of CO_2, which is one of the inert gases often present in natural gas. These categories can be used to show the variation of natural gas supplies around the world as shown in Table 3.2. Table 3.2 shows that the composition can change widely through out the world. For example, Europe's reserves are composed mostly of Type 1 natural gas which is mostly methane (ie. very little heavier hydrocarbons and little inert gas) and Australasia's reserves are mostly composed of Type 4 gas which contains a large portion of heavier hydrocarbons and inert gases.

Within the United States alone, the composition of natural gas can vary, as seen in a survey of 6800 gas samples in the United States[2] (see Table 3.3). The table shows the average natural gas composition as well as the 10^{th} and 90^{th} percentile of methane in the US. The composition if natural gas in the US can vary greatly with

Table 3.3: Natural Gas Composition Based on Methane Fraction in US (% mole)

Component	10 Percentile	Mean	90 Percentile
Methane	83.94%	93.05%	95.98%
Ethane	5.62%	3.47%	2.14%
Propane	0.99%	0.67%	0.36%
C_4 and higher	0.31%	0.33%	0.38%
Nitrogen	6.28%	1.67%	0.53%
Carbon Dioxide	1.37%	0.81%	0.73%
Oxygen	1.49%	0%	0%
Higher Heating Value (MJ/m^3)	36.6	38.3	38.3
Wobbe Number (MJ/m^3)	45.6	49.6	50.2
Methane Number[a]	80	93	98
Lean Flammability Limit[b]	5.2%	4.9%	4.9%
Hydrogen-Carbon Ratio	3.78	3.86	3.89

Source: Adapted from S. Schaedel, 1996[3]

[a] Calculated from experimental relation (Kubesh[4])

[b] Calculated from Le Chatelier's Rule[5]

methane concentrations ranging from 84% to 96%.

Composition changes can also occur over time at the same natural gas service station. Table 3.4 shows the composition of natural gas at a single Thailand service station in two different months. The table shows that over a few months the concentration of methane increased while heavier hydrocarbons and carbon dioxide decreased. Therefore, even fleet-type NGVs, which fill up at the same service station, must be able to run on a range of natural gas fuels.

3.2.1.2 Propane Peak-Shaving

Propane peak-shaving affects the composition of pipeline natural gas[2]. During high demand times for natural gas, such as winter, propane/air mixtures are added to natural gas to supplement natural gas supplies, this process is called propane peak-shaving.

The proportion of propane and air is such that it approximates the heating value and Wobbe number of the natural gas distributed in the pipeline. The heating value

Table 3.4: Thailand Natural Gas Composition at Single Supply Station by Date (% mole)

Component	August 2000	November 2000
Methane	68.9%	73.0%
Ethane	8.11%	6.94%
Propane	2.75%	1.91%
C_4 and higher	1.69%	1.21%
Nitrogen	1.71%	2.02%
Carbon Dioxide	16.8%	14.9%

Source: Chai-anun, 2002[6]

and Wobbe number are maintained so that furnaces, the largest consumers of natural gas, perform as expected. However, peak-shaving does not maintain other fuel properties that are important to NGV engines.

The most common peak-shaved mixtures are mixtures of 55% propane/45% air or 50% propane/50% air. Pure propane/air mixtures cannot be sent directly into the natural gas pipeline, rather they are a supplement to the natural gas. The maximum amount of peak-shaving allowed is a mixture of approximately 50% propane/air mixture and 50% natural gas. It has been noted that propane peak-shaving is only used during high demand times and only for a limited amount of time ie. a few hours to a few days. Since natural gas pipelines have relatively large, complex volumes a customer would rarely see a final mixture of 50% propane/air and 50% natural gas. Table 3.5 shows how the composition of a base natural gas changes with an increase in peak-shaving. As peak-shaving increases, the relative amount of methane decreases dramatically while the concentration of propane, nitrogen and oxygen increases.

3.2.2 Composition Effects on Fuel Properties and NGV Performance

The variation in natural gas composition changes the properties of the fuel for automotive use. Properties of interest for NGVs include: the heating value, Wobbe number, methane number, lean flammability limit and hydrogen-carbon ratio.

Table 3.5: Propane Peak-shaved Natural Gas Composition with Varying Degrees of Peak-shaving (% mole)

		% Peak-shaving			
Component	Base Gas	10%	15%	20%	25%
Methane	94.69%	85.22%	80.49%	75.77%	71.04%
Ethane	2.93%	2.68%	2.55%	2.42%	2.30%
Propane	0.22%	3.85%	5.44%	7.48%	9.29%
C_4 and higher	0.05%	0.13%	0.19%	0.21%	0.25%
Nitrogen	1.44%	6.04%	8.53%	10.63%	12.93%
Carbon Dioxide	0.67%	0.60%	0.57%	0.54%	0.50%
Oxygen	0.00%	1.26%	1.94%	2.52%	3.15%
Heating Value (MJ/m^3)	37.8	37.8	37.5	37.7	37.7
Wobbe Number (MJ/m^3)	49.5	47.0	45.6	44.8	43.9
Methane Number[a]	97	86	81	75[b]	70[b]
Lean Flammability Limit[c]	5.0%	5.1%	5.1%	5.1%	5.1%
Hydrogen-Carbon Ratio	3.90	3.77	3.71	3.63	3.57

Source: Adapted from M. E. Richards, 1996[7]

[a] Calculated from experimental relation (Kubesh,1992[4])

[b] Estimated value; equation not tested on NG with less than 80% methane

[c] Calculated from Le Chatelier's Rule[5]

3.2.2.1 Heating Value

The heating value of a fuel is defined as the magnitude of the heat of reaction for the complete combustion of a unit mass of fuel[8]. The higher heating value is defined as the heating value of the fuel when water is assumed to be fully condensed to the liquid phase, while the lower heating value assumes that the water vapour remains in the gas phase. Table 3.3 shows that the heating value of base natural gas increases with increasing methane content and a corresponding decrease in inert gases. However, Table 3.5 shows that peak-shaving natural gas has little effect on the heating value of the gas, since the propane/air mixture and methane have similar heating values.

3.2.2.2 Wobbe Number

The Wobbe number is a measure of the energy content of natural gas which considers the density of the fuel and heating value[3,9], as shown in Eq. 3.1:

$$W = \frac{HHV}{\sqrt{sg}} \tag{3.1}$$

where HHV is the volumetric higher heating value and sg is the specific gravity of the fuel with respect to air.

The Wobbe number is traditionally used to describe the interchangeability of various gas mixtures. In engine applications, the Wobbe number is proportional to the stoichiometric air to fuel ratio in a natural gas vehicle[10]. In general, an increase in methane or decrease in propane peak-shaving also increases the Wobbe number[11] as seen in Table 3.3 and 3.5.

Propane peak-shaving can also cause wide variations in the Wobbe number of the fuel while the fuel is in the fuel cylinder of the vehicle. In high pressure natural gas tanks, the heavy hydrocarbons in the fuel can condense. If the heavy hydrocarbons drop out, the gaseous fuel reaching the engine will have a relatively high amount of inert gases and a low Wobbe number. As the fuel is consumed the pressure in the tank decreases and the heavy liquid hydrocarbons will re-evaporate thereby increasing the Wobbe number of the fuel.

Changes in the Wobbe number of a fuel can have negative effects on lean burn NGVs. Generally, lean burn NGVs are converted from diesel engines with high compression ratios and are run on the lean side of stoichiometric. These vehicles are traditionally controlled in a open-loop system. These vehicles can perform as expected when the Wobbe number of the fuel remains constant. However, when a lean burn engine runs rich (ie. the fuel has a high Wobbe number) the engine will produce a higher than expect power output and CO emissions increase. When the engine runs lean (ie. the fuel has a low Wobbe number) then the engine can run too lean, resulting in misfires, hesitation or stalling[11,12].

3.2.2.3 Methane Number

The methane number was developed to quantify the knock tendency of a gaseous fuel, much like the octane number for gasoline fuels[9,13,14]. The methane number uses pure methane and pure hydrogen as reference gases, which have a methane number of 100 and 0, respectively. Numerous equations have been developed which relate the composition of natural gas to the methane number[4,14]. The methane number for the sample gases were calculated and are shown in Tables 3.3 and 3.5.

In general, heavier hydrocarbons and inert gases in the natural gas, such as propane peak-shaved natural gas, lower the methane number of the fuel[11]. Also, condensation of heavier hydrocarbons in the fuel tank can effect the methane number of the fuel. If these hydrocarbons condense in the fuel tank, the methane number will increase with the increased proportion of methane in the fuel. Likewise, the methane number will decrease as the hydrocarbons re-evaporate into the gaseous fuel.

Lean burn and high compression ratio stoichiometric NGVs are susceptible to engine knock with low methane number fuels. These vehicles are designed with high compression ratios for optimum fuel consumption. However, low methane number fuels will cause knock in these engines, which can destroy the engine.

3.2.2.4 Lean Flammability Limit

The lean flammability limit (LFL) is the minimum concentration of fuel required for self-sustaining flame propagation at a specific initial pressure and temperature[15]. The LFL varies with composition of the fuel and can be approximated with Le Chatelier's Rule[5,16,17] (see App. E).

In general, the LFL decreases with an increase in heavier hydrocarbons and increases with an increase in inert gases. The LFLs of the sample gases are shown in Tables 3.3 and 3.5. These sample gases show that the LFL changes little with propane peak-shaving since the addition of propane decreases the LFL while the addition of air increases the LFL. However, low LFLs can occur when the natural gas is composed of large amounts of inert gases and little heavier hydrocarbons. For example, natural gas from Thailand (with a composition of approximately 70% methane, 10% heavier hydrocarbons and 17% inert gases) has a LFL of approximately 5.5%, which approaches the concentration of fuel required in a lean burn NGV. LFLs of this order of magnitude can also arise when the heavier hydrocarbons in peak-shaved natural gas condense in the gas tank resulting in a fuel with few heavier hydrocarbons and large amounts of inert gases.

In an internal combustion engine (ICE), fuel concentrations below the LFL will result in misfire and extremely high unburnt hydrocarbons emissions[12]. Lean burn NGVs operate close to the LFL of the fuel, so changes in fuel which lowers the LFL can cause engine misfire if the engine control system does not compensate for the change in the LFL.

3.2.2.5 Hydrogen-Carbon Ratio

The hydrogen-carbon (H/C) ratio is the ratio of hydrogen atoms to carbon atoms in the fuel. For example, methane (CH_4) will have a H/C ratio of 4. Exhaust gas oxygen sensors in NGVs operate on a fixed and known H/C ratio[18] so changes in the H/C ratio can cause voltage biasing in the sensor.

In general, the H/C ratio of a natural gas fuel will increase with increased amounts of methane and decrease with increased amounts of heavier hydrocarbons and carbon dioxide. Table 3.3 shows the increase of the H/C ratio with the increase of methane. The H/C ratio of peak-shaved natural gas will decrease with an increase in peak-shaving (see Table 3.5) due to the increase of heavier hydrocarbons.

Changes in the H/C ratio can be concerning for NGVs operating on a closed-loop control system. Stoichiometric NGVs are the most common closed-looped NGV. In general, stoichiometric NGVs are converted from gasoline vehicles with closed-loop control systems. The majority of these vehicles are normally aspirated, have low compression ratios (8:1 to 12:1) and use oxygen sensors and three-way catalyst to control emissions. These vehicles can handle small composition changes since they can maintain a desired air-to-fuel ratio. However, it has been shown that large changes in gas composition adversely affect the emissions performance of closed-loop vehicles[19]. Closed-loop vehicles have learn capabilities to adjust to the variability in gas quality. However it takes time (on the order of one minute) for the engine control module (ECM) to adjust to the new fuel. This delay, which allows the ECM to learn, can result in increased emissions and lower performance[20]. This can be particulary troublesome with peak-shaved fuel where the fuel composition can change dynamically within the fuel tank. Furthermore, changes in the H/C ratio of the fuel can cause the oxygen sensor to make inaccurate air-to-fuel ratio measurements. This can result in the vehicle continually operating above or below stoichiometric, which will result in higher emissions and decreased performance.

Closed-loop, lean burn NGVs have also been developed to avoid some complications with fuel quality differences[21]. These types of vehicles have been shown to handle changes in the fuel's Wobbe number. However, they are still susceptible to poor performance during the time the vehicle adjusts to changes in the vehicle's fuel[22]. As with the stoichiometric engine, changes in the H/C ratio of the fuel can cause inaccurate measurements from the oxygen sensor, leading to poor vehicle performance, increased emissions and engine misfires.

3.2.3 Methods of Natural Gas Quality Measurement

A natural gas fuel quality (NGQ) sensor can be used to improve vehicle performance. A study was conducted to determine what information was needed for a NGV sensor[23]. It was found that a sensor which measured the fuel's methane number and Wobbe number would be useful in improving the performance of NGVs. Ideally, this type of sensor would be used in conjunction with a feed-back engine control system where a NGQ sensor is used to give an initial 'guess' of the fuel quality and the feed-back system would fine tune the engine parameters. This type of system would drastically reduce the amount of time for the engine to learn a new fuel.

It is proposed that a sensor to measure the LFL would be useful for lean burn NGVs which operate close the LFL. This sensor could be used in a feed-forward control system to compensate for fuel which would cause misfires in the engine. For closed-loop NGVs a sensor which determined the H/C ratio of the fuel could be used to compensate for changes in the output reading of the oxygen sensor.

The study also found that various sensors could be used to determine the quality of the natural gas. Sensors such as sound speed sensors, microanemometers[24], optical sensors etc could be used. However, the sound speed sensor was determine to be best suited for the application because of cost, durability and accuracy.

3.3 Justification for a Variable Gaseous Fuel Concentration Sensor

In search of cleaner internal combustion engines, considerable research has been conducted on using hydrogen as a fuel[25–27]. It has been shown that hydrogen fueled internal combustion engines can reach the equivalent zero emission vehicle (EZEV) limits and be thermodynamically efficient[28]. However, due to tank size limitations, the range of the vehicle is limited and current lack of hydrogen fueling stations further limits the range of the vehicle.

A mixture of hydrogen and methane or natural gas, called Hythane® (a registered trademark of Hydrogen Consultants Inc.) has been used as a fuel for ICEs. The addition of hydrogen to the natural gas lowers the lean flammability limit of the fuel, so that the engine consumes less fuel[29,30]. It has been shown that the emissions from a Hythane vehicle can be very low, even reaching EZEV standards[28,31]. Mixtures of hydrogen and natural gas have also been shown to increase engine efficiency[32].

Due to the limited number of hydrogen or Hythane fueling stations; it was proposed by Norbeck et al, to use a Variable Gaseous Fuel (VGF) vehicle[33,34]. A VGF vehicle can be operated on hydrogen, natural gas or a mixture of the two, such as Hythane. A VGF vehicle can be refilled at a hydrogen, natural gas, or Hythane station regardless of the fuel currently in the fuel tank. The advantages of using such a vehicle include: i) reaching EZEV standards by using pure hydrogen or hydrogen-rich Hythane, ii) using convenient home fueling devices such as natural gas compressors or developmental home-use electrolysis hydrogen producers, iii) the availability of numerous natural gas, hydrogen, and Hythane fueling stations that are already in service, iv) comparable cost of production to conventional vehicles and v) the stimulation to develop a gaseous fuel infrastructure for a transition into fuel cell or pure-hydrogen ICE vehicles[34].

Hydrogen, Hythane and natural gas have very different fuel properties. Because of this, a fuel composition sensor and an engine control system are required for successful operation of a VGF vehicle. The fuel composition sensor is required to distinguish between the changing composition of the fuel. The composition measurement can be used in a feed-forward engine control system which updates engine parameters such as fuel injection and ignition timing, thereby optimizing the engine for the given fuel.

Norbeck et al, developed a gas composition sensor using a thermal conductivity method. However, this sensor suffers from slow response time, pressure and temperature dependance and complex electronics. Thermal conductivity methods are also susceptible to durability issues due to sensor contamination. It is proposed that an ultrasonic sound speed method can be used to determine gas composition with a faster response time, pressure independence and an ability to determine natural gas quality as described in Sec. 3.2.3.

3.4 Theory of Gas Quality and Concentration Measurement with Sound Speed

Sound speed measurements can be used to determine the concentration or quality of a binary or quasi-binary gas mixture. For an ideal gas, the sound speed can be calculated using Eq. 3.2:

$$c = \sqrt{\frac{\gamma RT}{M}} \tag{3.2}$$

where R is the universal gas constant, T is the temperature, M is the molecular weight and γ is the ratio of specific heat at constant pressure, C_p, to the specific heat at constant volume, C_v.

For a mixture of gases the sound speed can be found from Eq. 3.3:

$$c = \sqrt{\frac{\sum\limits_i y_i C_{p_i}}{\sum\limits_i y_i C_{v_i}} \frac{RT}{\sum\limits_i y_i M_i}} \tag{3.3}$$

where y_i is the molar or volume fraction of gas i, C_{p_i} and C_{v_i} are the specific heats for gas i and M_i is the molecular weight of gas i.

For any gas mixture, c is affected by the temperature, molar mass and the ratio of specific heats, γ. Thus, for gas concentration measurements temperature compensation is required.

Table 3.6: Sound Speed of Gases at S.T.P.

Gas	Sound Speed (m/s)
Methane	448
Ethane	313
Propane	252
Butane	216
Nitrogen	330
Carbon Dioxide	260
Oxygen	310

3.4.1 Sound Speed in Natural Gas

The sound speed of natural gas varies with the composition of the gas. Natural gas is composed of mostly methane with heavier hydrocarbons (such as ethane, propane and butane) and inert gases such as carbon dioxide and nitrogen. With propane peak-shaving, the composition of natural gas will also include oxygen. The sound speed of each of these components can be seen in Table 3.6. The table shows that methane has the highest sound speed of the components. All of these components will affect the sound speed of the natural gas according to Eq. 3.3. Figure 3.1 shows the sound speed of mixtures of methane and nitrogen, propane and peak-shaved methane. The figure shows that increasing the amounts of nitrogen, propane or peak-shaved gas, decreases the sound speed of the mixture. Therefore, the sound speed of natural gas is highly dependant on the composition.

Studies have proposed that there are correlations between the properties and sound speed of natural gas[35,36]. The studies plotted the sound speed of 6,700 natural gas samples by fuel quality properties, although the studies did not include samples of peak-shaved natural gas. The studies showed that there was a strong correlation between sound speed and percent methane, percent non-methane hydrocarbons, density and methane number. Moderate correlations were found for the air-fuel ratio, hydrogen-carbon ratio, Wobbe index and LFL.

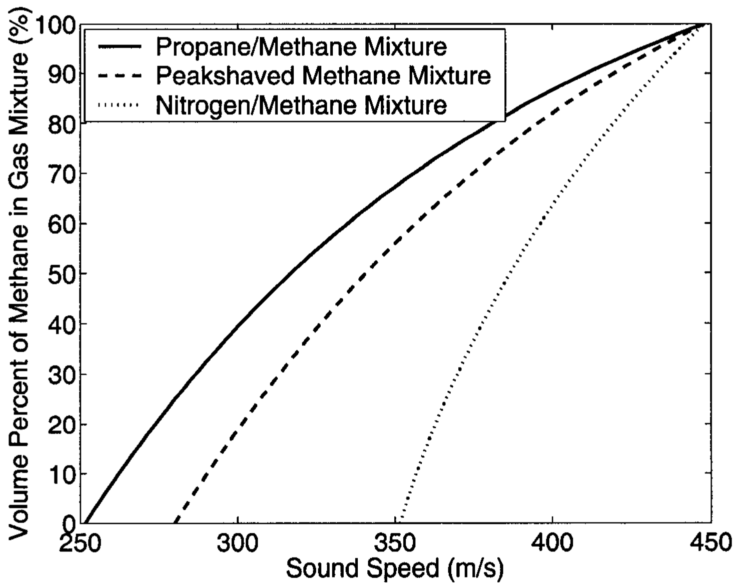

Figure 3.1: Sound Speeds of Mixtures of Methane and Other Gases at S.T.P.

Similar correlations can be found for peak-shaved natural gas. Plotting the methane number, Wobbe index, LFL and H/C data found in Table 3.5 by the sound speed, indicates that there is a correlation between sound speed and the fuel properties (see Fig. 3.2). The figure shows that the sound speed increases with an increase of methane number, Wobbe number and H/C ratio. The sound speed did not correlate well with the LFL, as the LFL does not change with propane peak-shaving.

These correlations indicate that a sound speed sensor would be able to measure the methane number, Wobbe number and H/C ratio of natural gas and peak-shaved natural gas fuel. However, there is little correlation between the sound speed of a peak-shaved natural gas and the LFL, while there is a moderate correlation between sound speed and LFL for non-peak-shaved natural gas. Therefore, a sound speed sensor may not be able to be used as a LFL sensor without further fuel measurements. For example, a oxygen sensor could be used in the fuel to determine if the fuel was peak-shaved (since only peak-shaved gas contains oxygen), or an exhaust oxygen sensor could be used in a control system to determine if the fuel was peak-shaved.

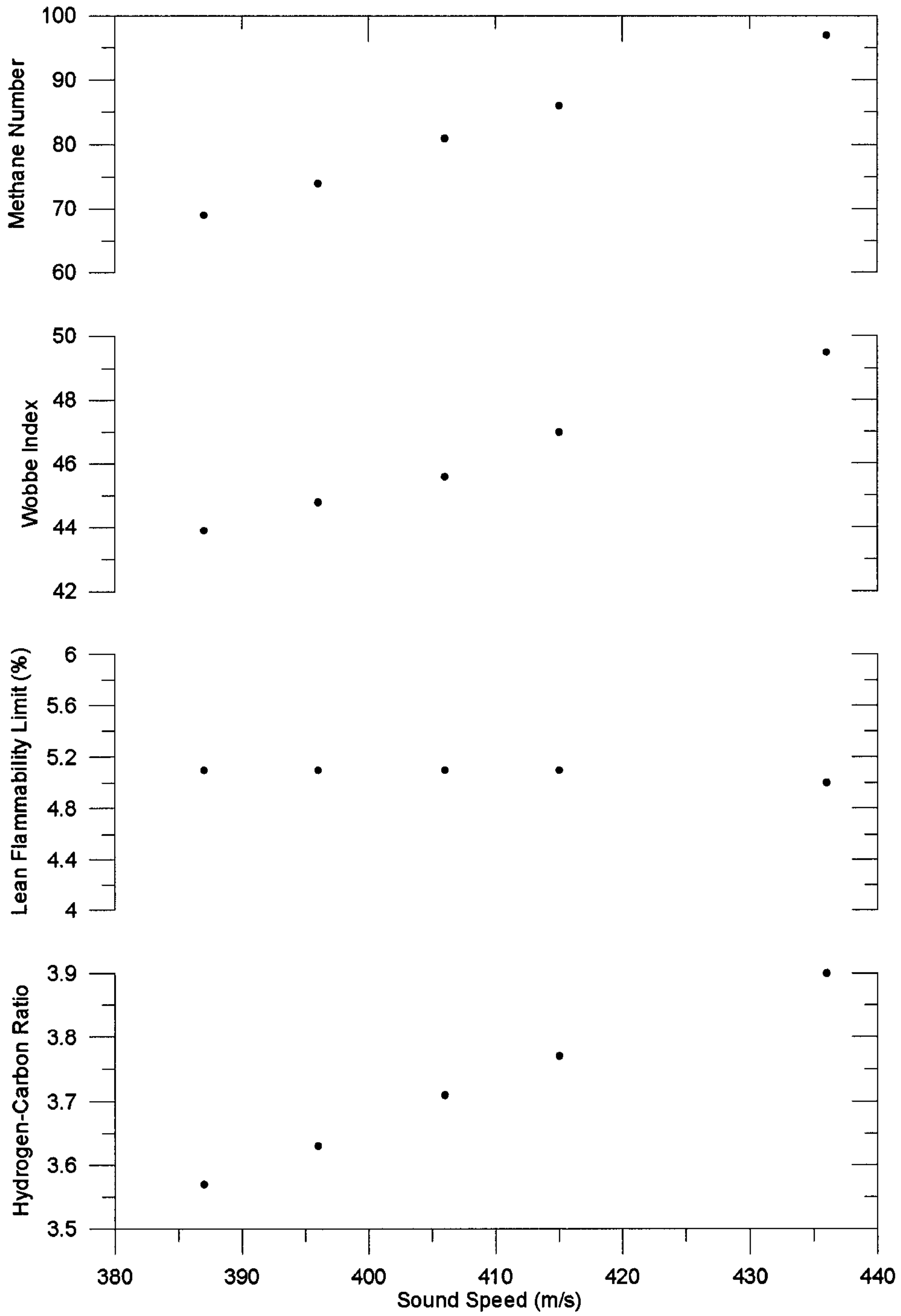

Figure 3.2: Correlation of Sound Speed with Fuel Properties of Peak-shaved Natural Gas (Data from Table 3.5)

The sound speeds in natural gas can range from approximately 370 to 450 m/s at standard temperature[35]. However, for automotive applications, temperatures from -40 to 100°C can be expected. Due to the fluctuation in the temperature, the range of sound speeds to be measured with an NGQ sensor will range from approximately 325 to 500 m/s.

3.4.2 Sound Speed in Natural Gas and Hydrogen Mixtures

A sound speed sensor can measure the composition of a binary gas fuel. For a VGF vehicle, the fuel (composed of hydrogen and natural gas) can be assumed to be a binary mixture of hydrogen and methane. For a binary mixture of hydrogen and methane Eq. 3.3 can be reduced to:

$$c = \sqrt{\frac{RT(y_{\mathrm{H_2}}C_{p_{\mathrm{H_2}}} + (1 - y_{\mathrm{H_2}})C_{p_{\mathrm{CH_4}}})}{(y_{\mathrm{H_2}}M_{\mathrm{H_2}} + (1 - y_{\mathrm{H_2}})M_{\mathrm{CH_4}})(y_{\mathrm{H_2}}C_{v_{\mathrm{H_2}}} + (1 - y_{\mathrm{H_2}})C_{v_{\mathrm{CH_4}}})}} \tag{3.4}$$

Figure 3.3 shows the sound speed of a mixture of hydrogen and methane as a function of concentration. As the fraction of hydrogen increases, the sound speed of the mixture increases rapidly since the sound speed of hydrogen (~1300 m/s at standard temperature) is much higher than that of methane (~450 m/s at standard temperature).

Equation 3.4 assumed that the fuel is a binary mixture of hydrogen and pure methane (instead of natural gas). This assumption will result in measurement error in a sound speed system since the sound speed of natural gas will vary with changes in the composition of the natural gas. Figure 3.3 shows the sound speed of mixtures of hydrogen and pure methane, the United States mean natural gas, and the 10th and 90th percentile of methane concentration (see Table 3.3). The figure shows that the sound speed of the fuel changes with the various types of natural gas present. Therefore, a single sound speed measurement could represent a range of hydrogen

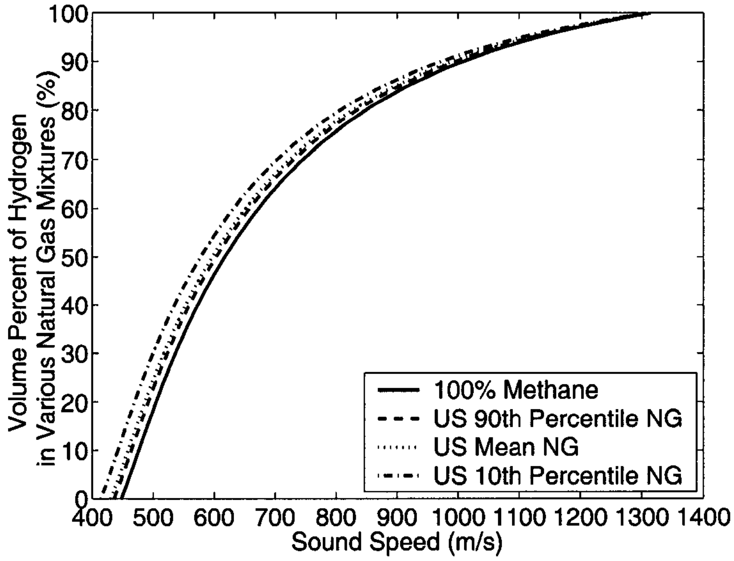

Figure 3.3: Sound Speed of Hydrogen and Natural Gas Mixtures

concentration measurements. For proper vehicle operation, a sound speed sensor can be used in conjunction with a feed-back control system; where the sound speed sensor approximates the amount of hydrogen in the fuel, and the control system is used to fine tune for the variation in the natural gas composition.

In a VGF vehicle, a sound speed sensor can be used to measure the concentration of a hydrogen/natural gas mixture, but it can also be used as a NGQ sensor when the vehicle is only operating on natural gas. For example, measurements above 450 m/s (at standard temperature) can be assumed to be mixtures of hydrogen and methane, from which the concentration of the hydrogen can be found. For measurements below 450 m/s, the fuel is assumed to be natural gas. Therefore, the properties of the natural gas such as methane number and Wobbe index can be found if the only fuel in the tank is natural gas (see Fig. 3.4).

The sound speeds in hydrogen and methane mixtures can range from 450 to 1300 m/s at standard temperature, and natural gas mixtures can be as low as 370 m/s. For operation in a vehicle, with temperatures ranging from -40 to 100°C, the range of

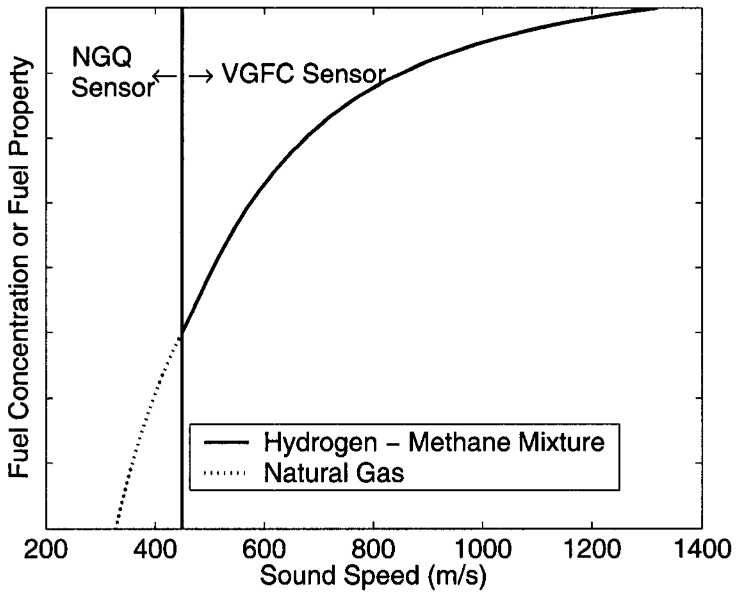

Figure 3.4: Combined Natural Gas Quality Sensor and VGFC Sensor

sound speed necessary for a combined VGFC/NGQ sensor will be 325 to 1470 m/s.

3.5 Experimental Set-Up

The theory of gas concentration measurement by a sound speed sensor was tested using the discrete acoustic wave and phase detection method as described in Chapter 2. The experiment was constructed so that sound speeds could be measured for various gas mixtures.

Figure 3.5 depicts the experimental set-up used to measure the sound speed of gas mixtures. Mixtures of nitrogen and methane were used to create a range of sound speeds that are typical for natural gas. Mixtures of methane and hydrogen were also used to measure the sound speed over the range typical for VGF vehicles. For each sample mixture, two gases were fed into the Dasibi® multi-gas calibrator. The Dasibi® multi-gas calibrator contains mass flow controllers which were calibrated for the gases used in the experiments as shown in App. B. After the gases mixed, the

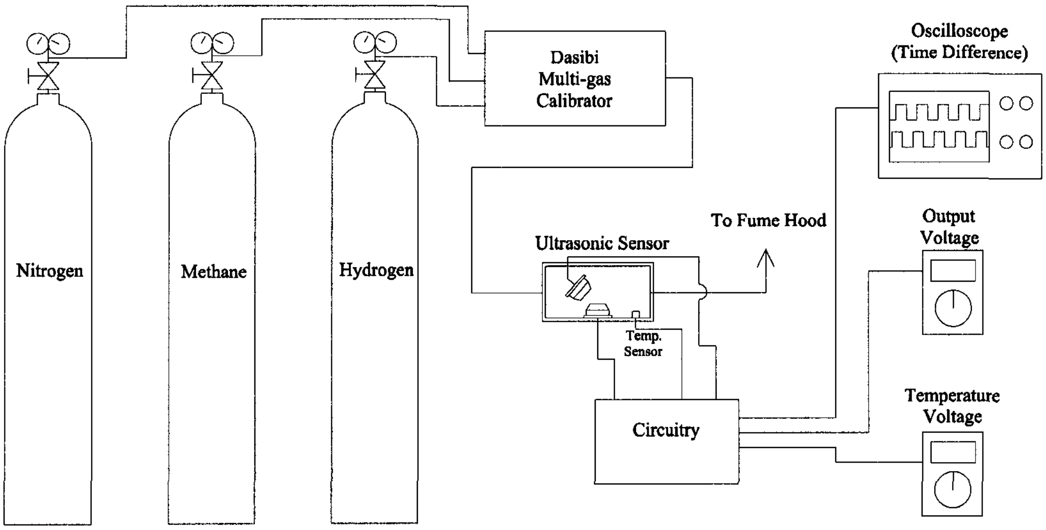

Figure 3.5: Schematic of Variable Gas Composition Experimental Set-Up

sample would flow through the ultrasonic sensor and into a fume hood.

The small prototype, using the DAWPD method, was used as described in Chap. 2 and App. C. The small prototype was set-up with a normal distance of 8 mm, an offset of 4 mm and an angle of 70°. This configuration was found to minimize error for the sound speeds tested and cover the range of sound speeds for the experimental gas mixtures used.

The sound speed is highly dependant on temperature (see Eq. 3.2). A fast response AD590 temperature sensor was mounted inside the prototype to ensure that the gas temperature remained constant during the experiments.

For each sample mixture, the sensor output voltage, temperature and time difference was measured and recorded. The time difference is the relative time difference between the transmitted and received ultrasonic waves. By displaying the transmitted and received signals on the oscilloscope the time difference could be measured manually. The time difference was measured to compare experimental and theoretical results. The time difference, Φ, is related to the phase difference, ϕ, by:

$$\Phi = \frac{\phi}{2\pi f} \tag{3.5}$$

3.6 Experimental Results

The theory of natural gas quality measurement and variable gaseous fuel concentration measurement were verified by the experimental data collected. This section will show that the DAWPD method can be used for a natural gas quality sensor or a VGF concentration sensor. Results of the testing showed that the DAWPD method provides adequate accuracy, repeatability, resolution and range.

3.6.1 Experimental Results for the Natural Gas Quality Sensor

Mixtures of nitrogen and methane were used to create a range of sound speeds typical of natural gas at standard temperature. The DAWPD method measures the phase difference between the transmitted and received ultrasonic waves in the sensor (see Chap. 2). To compare experimental and theoretical data, the time difference between the transmitted and received wave can be used, where the time difference and phase difference are related, as shown in Eq. 3.5.

Experimentally, the time difference can be determined by measuring the time difference between the transmitted and received waves on an oscilloscope. The theoretical time difference for each gas sample mixture, Φ_i, can be calculated by the following equation:

$$\Phi_i = \frac{d}{|\frac{1}{c_1} - \frac{1}{c_i}|} \tag{3.6}$$

where d is the path length of the sensor, c_1 is the sound speed of the reference gas mixture (in this case pure nitrogen) and c_i is the sound speed of the sample mixture. The path length could be determined by measuring the distance between the transducers. However, the exact location of the start and end of the standing waves between the transducers is difficult to determine. Therefore, the theoretical path length between the transducers, d^*, can be estimated by experimental data:

$$d^* = \left| \frac{\Phi_1 - \Phi_n}{\frac{1}{c_1} - \frac{1}{c_n}} \right| \tag{3.7}$$

where Φ_1 and Φ_n are the experimental time difference measurements spanning the range of measurements and c_1 and c_n are the sound speeds of the corresponding gas mixtures (in this case pure nitrogen and pure methane, respectively). These sound speeds can be determined from Eq. 3.3 since a binary gas mixture (nitrogen and methane) was used to create the range of sound speeds. For this particular prototype the theoretical distance was determined to be 11.1 mm (see App. F). As discussed in Sec. 3.5, the normal distance was 8 mm and the offset was 4 mm (see Fig. 2.21). Therefore, the expected path length between the transducers would be 8.9 mm (where the expected path length can be found by taking the 'root-sum-square' of the offset and normal distance). The difference between the measurement and calculation can be attributed to the fact that the ultrasonic waves are generated slightly inside the transducer itself.

Once the theoretical path length is determined, then the theoretical time difference for each gas sample mixture, Φ_i, can be found by substituting the theoretical path length into Eq. 3.6. Table 3.7 shows the calculation of the theoretical time difference of the NGQ sensor.

Figure 3.6 compares the experimental and theoretical time difference over a range of sound speeds (bottom x-axis). This figure shows that the experimental data closely matches the theoretical curve. Reasons for differences between the results can be attributed to sensor error which is described in detail in section 2.5.

The plot also shows the concentration of methane in the methane/nitrogen mix-

Table 3.7: Theoretical and Experimental Data of Natural Gas Quality Sensor

Concentration (%vol. CH_4)	Sound Speed (eq. 3.3) (T=23.9°C) (m/s)	Theoretical Time Difference (eq. 3.6) (μs)	Experimental Time Difference (μs)
0.00	350.5	6.8	6.8
7.74	354.4	6.5	6.4
15.9	359.1	6.0	6.0
24.4	364.7	5.5	5.5
33.5	371.3	5.0	4.9
43.0	379.0	4.4	4.4
53.1	388.2	3.7	3.5
63.8	399.0	3.0	2.8
75.1	411.9	2.1	1.9
87.2	427.4	1.1	0.9
100	446.3	0.0	0.0

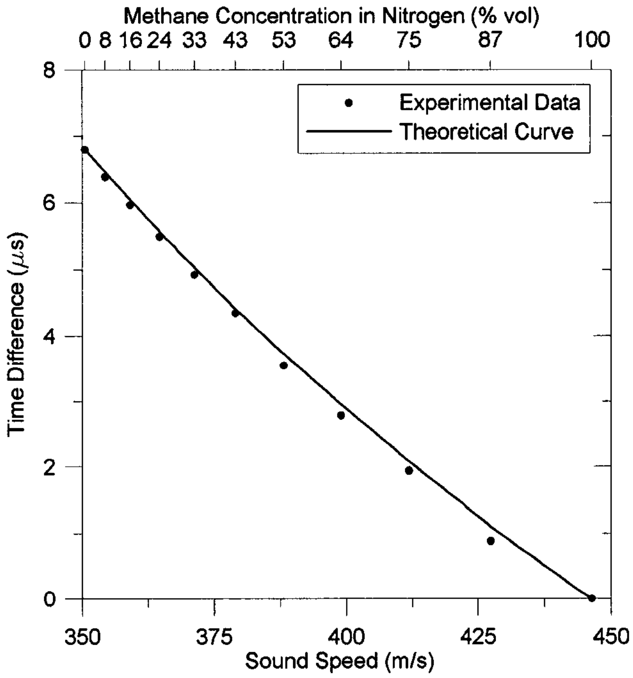

Figure 3.6: Comparison of Experimental and Theoretical Data for Natural Gas Sensor

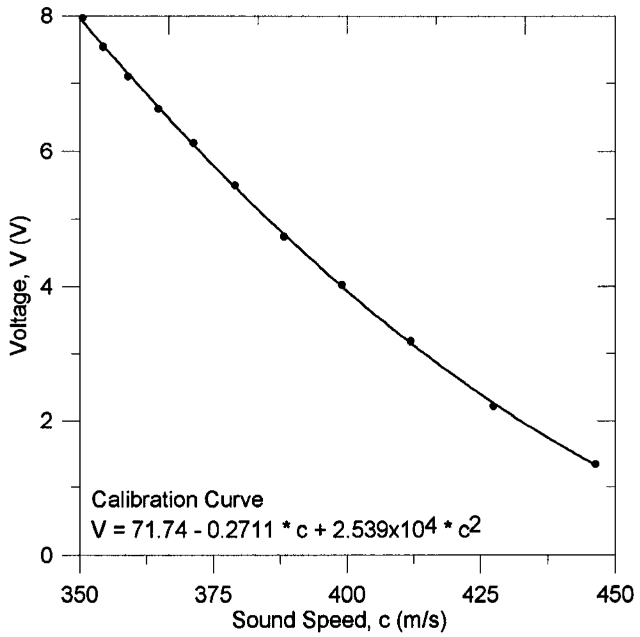

Figure 3.7: Calibration Curve of Prototype Natural Gas Quality Sensor

ture used to produce the variation in sound speeds (top x-axis). The property of interest for the NGQ sensor is the sound speed and not the concentration of the gas; therefore, the data presented for the NGQ sensor will be expressed in terms of sound speed.

The calibration curve of the prototype natural gas quality sensor is shown in Fig. 3.7. The experimental measurements used in the calibration curve are the average of five tests. The results of these tests are shown in App. F.

The static characteristics, such as accuracy, repeatability error, calibration error, resolution error and range of the prototype sensor can be found. These static characteristics are calculated in App. F and are summarized in Table 3.8. The calibration, repeatability and resolution error was determined experimentally. For each type of error the most conservative, or worst-case, error limit was used. Therefore, the maximum error measured for each characteristic is given.

The accuracy, or the total error (δ_{total}), of the sensor can be calculated by using

Table 3.8: Static Characteristics of Natural Gas Quality Sensor

Characteristic	Value (m/s)
Accuracy, δ_{total}	±1.65
Calibration Error, δ_{cal}	±1.18
Repeatability Error, δ_r	±1.13
Resolution Error, δ_{res}	±0.22
Range (as tested)	297 - 446

the 'root-sum-of-squares' of the calibration, repeatability and resolution error. The accuracy of the sensor was determined to be ±1.65 m/s. From the correlations between the natural gas properties and sound speed found by Lueptow[35] it is apparent that an acoustic sensor with accuracy ±5 m/s would be adequate. Therefore, this prototype NGQ sensor using the DAWPD method will have adequate accuracy for this application.

The range of the NGQ sensor and the DAWPD method in general, is proportional to the design parameters such as path length, driving frequency, phase range of phase comparator and sound speed of the reference gas (see Sec. 2.4). The range of the prototype tested was 297 to 446 m/s. By adjusting the 'time delay' circuitry (see Fig. 2.12), the range of the prototype can be adjusted. As discussed in Sec. 3.4, the range of sound speeds that can occur in natural gas in automotive applications is approximately 325 to 500 m/s. However, by adjusting the 'time delay' circuitry the range could be set to 320 to 500 m/s.

3.6.2 Experimental Results for the Variable Gaseous Fuel Concentration Sensor

Mixtures of methane and hydrogen were used to test the prototype variable gaseous fuel concentration (VGFC) sensor. Theoretical and experimental time differences were used to compare theoretical and experimental data. The VGFC sensor uses the same transducer set-up as the NGQ sensor (ie. 8 mm normal distance, 4 mm

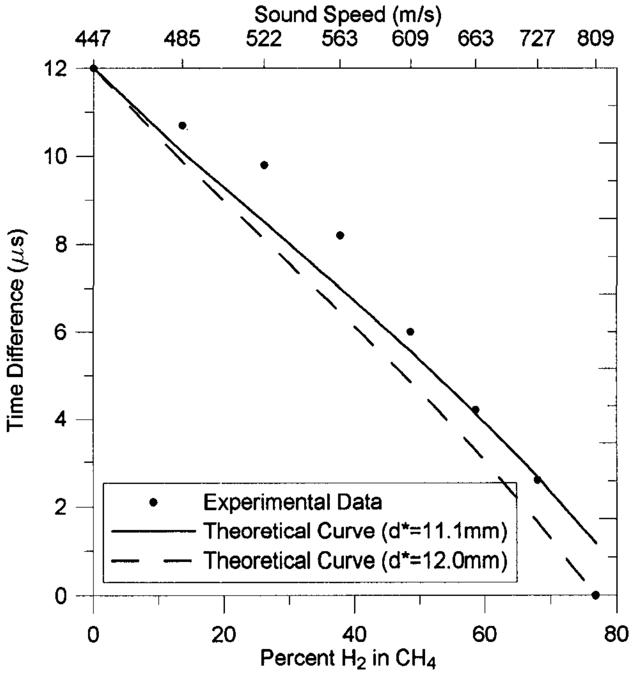

Figure 3.8: Comparison of Experimental and Theoretical Data for Variable Gaseous Fuel Concentration Sensor

offset and 70° angle), because of the identical set-up for both sensors the theoretical path length was expected to be the same. However, after applying Eq. 3.7 to the experimental data for the VGFC sensor, the theoretical path length of the VGFC sensor was found to be 12.0 mm compared to 11.1 mm for the NGQ sensor. Figure 3.8 shows the experimental time difference data and the theoretical time difference data calculated with both theoretical path lengths. From the figure, it is apparent that the experimental measurements have considerable error, and the theoretical path length using the VGFC sensor data (ie. 12.0 mm) is not an accurate representation. For comparison of theoretical and experimental data, the theoretical path length found from the NGQ data (ie. 11.1 mm) will be used instead of that of the VGFC sensor.

Figure 3.8 shows that the experimental data deviates greatly from the theoretical data. This error is mostly likely due to reflections within the sensor (see Chap. 2). Also, the ultrasonic signal is reduced by the difference of acoustic impedance between the ultrasonic transducers and the gas medium the signal passes through. The weaker signal caused by this impedance mismatch could also lead to increased error in the sensor.

The range of the VGFC sensor is limited by the acoustic impedance mismatch of the gas medium and the transducers. With ultrasonic systems, optimum signal transmission is achieved when the ultrasonic transducers and gas medium have the same specific acoustic impedance[37,38]. The acoustic impedance, Z_a, is defined as:

$$Z_a = \rho c \tag{3.8}$$

where ρ is the density and c is the sound speed of the gas. For a mixture of gases, the acoustic impedance can be determined by calculating the density from the ideal gas equation and the sound speed from Eq. 3.3. Figure 3.9 depicts the acoustic impedance change with mixtures of nitrogen/methane and methane/hydrogen. At standard temperature and pressure, pure nitrogen has an acoustic impedance of 404 $\frac{\mathrm{kg}}{\mathrm{m^2 s}}$. As methane concentration increases, the acoustic impedance decreases in the nitrogen/methane mixture. Likewise, as the hydrogen concentration increases, the acoustic impedance of the methane/hydrogen mixture decreases. Ultrasonic transducers (including the transducers used in the prototype) are often designed so that the acoustic impedance is matched to air (430 $\frac{\mathrm{kg}}{\mathrm{m^2 s}}$). If the acoustic impedance of the transducers and the gas medium are different or mismatched, the transmission of the ultrasonic signal will be reduced. If the acoustic impedance mismatch is large enough, the signal may become undetectable.

Experimentally, the affect of acoustic impedance mismatch can be tested by measuring the amplitude of the received signal in mixtures of methane and hydrogen. Figure 3.10 shows the peak-to-peak amplitude of the received signal in mixtures of methane and hydrogen. With moderate amounts of hydrogen, the signal is relatively

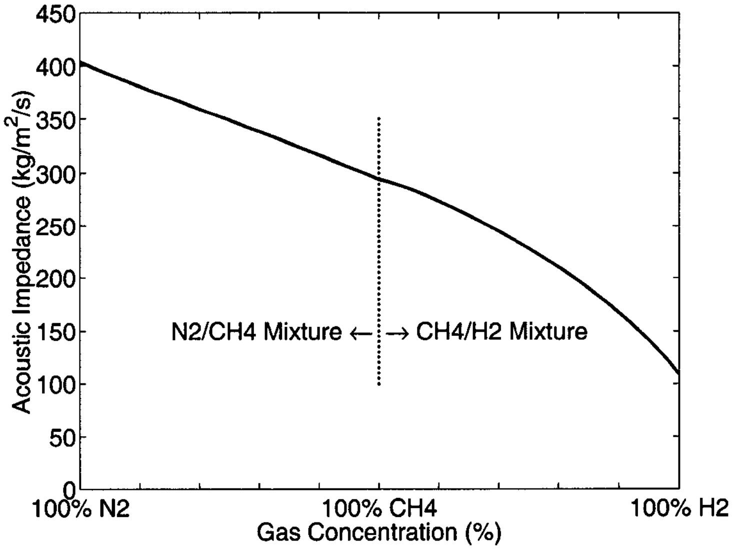

Figure 3.9: Acoustic Impedance of Mixtures of Nitrogen/Methane and Methane/ Hydrogen

constant. The increase and decrease of the signal amplitude is due to the constructive and destructive inference of the ultrasonic signal caused by reflections (see Sec. 2.5.1). As the acoustic impedance of the mixture decreases due to high amounts of hydrogen, the signal amplitude decreases. It was found that at approximately 80% hydrogen, the signal becomes too weak to get a reliable measurement. Therefore, the range of the prototype sensor is limited to approximately 80% hydrogen by volume. The range of the sensor could be extended to 100% hydrogen by using transducers that have acoustic impedances matched to a mixture of methane and hydrogen rather than air. These transducers would allow for a strong ultrasonic signal across the concentration range.

The calibration curve of the prototype VGFC sensor is shown in Fig. 3.11. The experimental measurements in the calibration curve are the average of five tests. The results of these tests are shown in App. F and the static characteristics for the VGFC sensor are summarized in Table 3.9. The property of interest for the VGFC sensor is the concentration of hydrogen in the fuel mixture. Therefore, the sensor

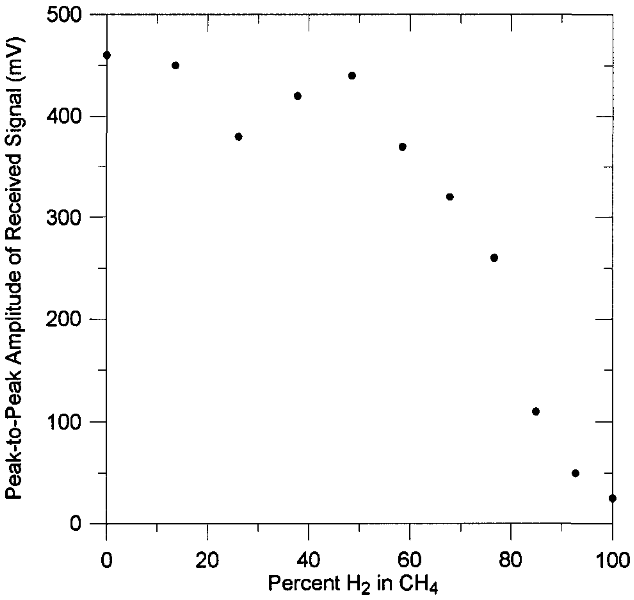

Figure 3.10: Peak-to-Peak Amplitude of Received Signal in Methane/Hydrogen Mixture

Table 3.9: Static Characteristics of Variable Gaseous Fuel Concentration Sensor

Characteristic	Value (% H_2 vol.)
Accuracy, δ_{total}	±6.31
Calibration Error, δ_{cal}	±3.64
Repeatability Error, δ_r	±5.15
Resolution Error, δ_{res}	±0.04
Range (as tested)	0 - 77.5

characteristics will be expressed in % hydrogen by volume. As with the NGQ sensor, the calibration, repeatability and resolution error was determined experimentally for the VGFC sensor. For each type of error the most conservative, or worst-case, error limit was used. Therefore, the maximum error measured for each characteristic is given.

The accuracy of the VGFC sensor was found to be ±6.31% hydrogen by volume. As mentioned above (see Sec. 3.4.2), variations in natural gas concentration at low hydrogen levels will result in measurement error. This error in concentration is on the order of ±6% hydrogen. Therefore, the accuracy of the sensor is adequate for

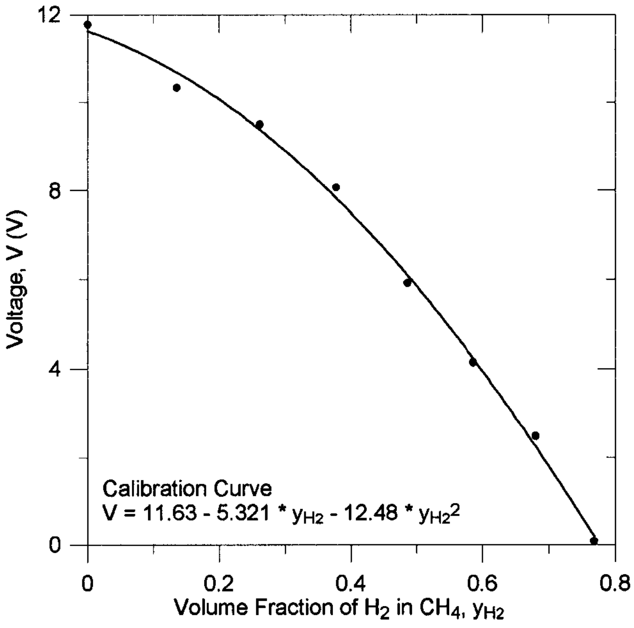

Figure 3.11: Calibration Curve of Prototype Variable Gaseous Fuel Concentration Sensor

this application, since the sensor will be used to give an initial guess of the fuel concentration and a feed-back control system will be used to adapt to changes in the natural gas fuel quality.

As mentioned above, the DAWPD method could be used for a combined NGQ and VGFC sensor. For this measurement system the combined sensor must be able to measure a sound speed range of 325 to 1470 m/s. By decreasing the path length or the driving frequency of the sensor, the relative range of the prototype sensors can increased to meet the range requirements (see Chap. 2). Furthermore, transducers are needed which can generate strong signals in low acoustic impedance conditions such as those present with high hydrogen concentrations.

3.7 Conclusions

This chapter has discussed the need for a natural gas quality sensor. Compositional changes in natural gas have severe effects on the performance of NGVs. Sound speed sensors are well suited for measuring the quality of natural gas in automotive applications. In particular, the discrete acoustic wave and phase detection sensor is a excellent sound speed measurement method for automotive applications. It was shown that the DAWPD prototype has adequate accuracy and range for natural gas quality measurement.

For proper operation of a VGF vehicle a fuel concentration sensor is needed. It was shown that the DAWPD sensor could provide adequate accuracy for a VGFC sensor. It was found, however, that the range of the VGFC sensor was limited by poor acoustic impedance matching between the prototype transducers and high hydrogen concentration mixtures. The range of the prototype sensor could be improved by using transducers better matched to that particular medium.

REFERENCES

[1] J. L. Gadon, "Essai de répartition des réserves gazières par composition des gaz," *Revue de L'Institut du Pétrole*, vol. 42, no. 6, 1987.

[2] W. Liss, W. Thrasher, G. Steinmetz, A. Attari, and P. Chowdiah, "Variability of natural gas composition in select major metropolitan areas of the united states," Tech. Rep. GRI-92/0123, Gas Research Institute, 1992.

[3] S. Schaedel, M. Czachorski, P. Rowley, M. Richards, and Y. Shikari, "Gas composition issues and implications for natural gas vehicles and fueling stations," Tech. Rep. GRI-96/0028, Gas Research Institute, 1996.

[4] J. Kubesh, S. R. King, and W. E. Liss, "Effect of gas composition on octane number of natural gas fuels," *Society of Automotive Engineers*, 1992. SAE Paper 922359.

[5] M. G. Zabetakis, "Flammability characteristics of combustible gases and vapors," Tech. Rep. Bulletin 627, U.S. Bureau of Mines, 1965.

[6] W. T. Chai-anun, "Existing and year 2001-2006 gas composition forecast." Personal Communication, 2002. Petroleum Authority of Thailand (PTT).

[7] M. E. Richards, Y. Shikari, and C. Blazek, "Propane-air peakshaving impact on natural gas vehicles," Tech. Rep. GRI-96/0201, Gas Research Institute, 1996.

[8] J. B. Heywood, *Internal Combustion Engine Fundamentals.* McGraw Hill, Inc, 1988.

[9] J. Klimstra and H. R. Wolting, "Quality aspects of natural gas as an engine fuel," in *Proceedings of the Congress of "Gas Quality - Specification and Measurement of Physical and Chemical Properties of Natural Gas"*, (Groningen, The Netherlands), April 22-25, 1986.

[10] J. Klimstra, "Interchangeability of gaseous fuels - the importance of the wobbe-index," *Society of Automotive Engineers*, 1986. SAE Paper 861578.

[11] W. E. Liss and D. S. Moulton, "Effect of propane-air on NGVs and vehicle fueling stations," Tech. Rep. GRI-94/0158, Gas Research Institute, 1994.

[12] S. R. King, "The impact of natural gas composition on fuel metering and engine operational characteristics," *Society of Automotive Engineers*, 1992. SAE Paper 920593.

[13] T. J. Callahan, T. W. Ryan III, J. P. Buckingham, R. J. Kakockzi, and G. Sorge, "Engine knock rating of natural gases - expanding the methane number database," in *1996 ASME Fall Technical Conference vol. 4*, 1996.

[14] T. Ryan III, T. J. Callahan, and S. R. King, "Engine knock rating of natural gases - methane number," *Journal of Engineering for Gas Turbines and Power*, vol. 115, pp. 769–776, 1993.

[15] I. Glassman, *Combustion.* Academic Press, Inc, 1987.

[16] H. F. Coward and G. W. Jones, "Limits of flammability of gases and vapors," Tech. Rep. Bulletin 503, U.S. Bureau of Mines, 1952.

[17] G. W. Jones, *Inflammability of Mixed Gases.* U.S. Govt. Print. Off., 1929.

[18] J. W. Bozek, R. Evans, C. D. Tyree, and K. L. Zerafa, "Operating characteristics of zirconia galvanic cells (lambda sensors) in automotive closed-loop emission control systems," *Society of Automotive Engineers*, 1992. SAE Paper 920289.

[19] "LNG and propane-air peakshaving storage and deliverability," Tech. Rep. Issue Brief 1990-09, American Gas Association, 1990.

[20] J. Czerwinski and P. Comte, "Influences of gas quality on a natural gas engine," *Society of Automotive Engineers*, 2001. SAE Paper 2001-01-1194.

[21] P. Newman, "It's only natural," *Engine Technology International Magazine*, January 2002.

[22] N. N. Clark, G. E. Mott, C. M. Atkinson, R. J. deJong, R. J. Atkinson, T. Latvakosky, and M. L. Traver, "Effect of fuel composition on the operation of a lean-burn natural gas engine," *Society of Automotive Engineers*, 1995. SAE Paper 952560.

[23] J. E. Huebler and C. F. Blazek, "An evaluation of sensors of NGV and fueling station applications," Tech. Rep. GRI-93/0033, Gas Research Institute, 1993.

[24] U. Bonne, "Sensing fuel properties with thermal microsensors," in *International Society for Optical Engineering Vol. 2722*, 1996.

[25] M. A. DeLuchi, "Hydrogen vehicles: an evaluation of fuel storage, performance, safety, environmental impacts, and cost," *International Journal of Hydrogen Energy*, vol. 14, no. 2, pp. 81–130, 1989.

[26] J. M. Norbeck, *Hydrogen Fuel for Surface Transportation.* Society of Automotive Engineers, 1996.

[27] C. A. Kukkonen, "Hydrogen as an alternative automotive fuel: 1993 update," *Society of Automotive Engineers*, 1994. SAE Paper 940766.

[28] P. Van Blarigan, "Development of a hydrogen fueled internal combustion engine designed for single speed/power operation," in *SAE Future Transportation Technology Conference*, 1996. SAE Paper 961960.

[29] R. L. Hoekstra, K. Collier, and N. Mulligan, "Demostration of hydrogen mixed gas vehicles," in *Proceedings of the 10th World Hydrogen Energy Conference*, pp. 1781–1796, 1994.

[30] R. L. Hoekstra, K. Collier, N. Mulligan, and L. Chew, "Experimental study of a clean burning vehicle fuel," *International Journal of Hydrogen Energy*, vol. 20, no. 9, pp. 737–745, 1995.

[31] R. L. Hoekstra, P. Van Blarigan, and N. Mulligan, "NO_x emissions and effciency of hydrogen, natural gas, and hydrogen / natural gas blended fuels," *Society of Automotive Engineers*, 1996. SAE Paper 961103.

[32] R. Sierens and E. Rosseel, "Variable composition hydrogen / natural gas mixtures for increased engine efficiency and decreased emissions," in *ASME 1998 Spring Technical Conference ICE-Vol.30-3*, 1998. Paper No. 98-ICE-105.

[33] J. Norbeck, J. W. Heffel, C. S. Park, and P. B. Scott, "Development of a variable gaseous fuels engine to facilitate penetration of hydrogen in the transportation sector," Tech. Rep. 9812-AV-RT2F-FR, California Energy Commission, 1999.

[34] J. W. Heffel, J. M. Norbeck, C. S. Park, and P. B. Scott, "Development of a variable blend hydrogen - natural gas internal combustion engine. part 1 - sensor development," in *SAE Future Transportation Technology Conference*, 1999. SAE Paper 1999-01-2899.

[35] R. M. Lueptow, S. Phillips, and M. Oczkowski, "Acoustic natural gas fuel quality sensor," *Society of Automotive Engineers*, 1995. SAE Paper 950529.

[36] R. M. Lueptow and S. Phillips, "Acoustic sensor for determining combustion properties of natural gas," *Meas. Sci. Technol.*, vol. 5, pp. 1375–1381, 1994.

[37] J. Blitz, *Fundamentals of Ultrasonics.* Butterworth and Co., 1963.

[38] J. Blitz, *Elements of Acoustics.* Butterworth and Co., 1964.

CHAPTER 4

APPLICATION FOR AN ULTRASONIC GAS SENSOR - EGR SENSOR

4.1 Introduction

EXHAUST gas recirculation (EGR) has been used for years to improve the performance of internal combustion engines. This chapter shows that acoustic methods can be used to measure EGR. Theory is presented which shows that sound speed measurements can be used to measure the amount of EGR in the intake manifold. In particular, the discrete acoustic wave and phase detection (DAWPD) method can be used to measure EGR rates with a fast-response time.

Experimental results show that a DAWPD sensor could be used as an EGR sensor. The results of the experiment showed that EGR rates could be measured with adequate accuracy at steady-state. Transient measurements were not possible due to engine limitations. This chapter shows that the sensor's performance was limited by the ultrasonic transducers used. It is postulated that the sensor performance could be improved with smaller and temperature independent non-resonant transducers.

4.2 Justification for an Exhaust Gas Recirculation Sensor

Exhaust gas recirculation is a technique used to lower oxides of nitrogen (NO_x) emissions in automobiles. The principle of the technique is to mix exhaust gas with the intake air/fuel mixture. This has the effect of lowering the combustion temperature and slowing the combustion reaction, which has been shown to reduce NO_x emissions. EGR levels of 15% (by mass) have been to shown to reduce NO_x emissions dramatically and modern engines have been able to tolerate EGR rates up to 30%[1,2]. To optimize fuel economy, emissions and driveablity, EGR and spark timing must be controlled separately. Without variable valve timing, as engine speed and load increases, the amount of residual gas (or 'internal EGR') left in the cylinder decreases. Too little EGR in the cylinder provides less emission reduction benefits, while too much EGR can result in misfires and slow burning velocities, which result in a significant increase in unburnt hydrocarbons. Due to the variations in the amount of internal EGR, an external EGR system is used to control the amount of EGR.

Generally, external EGR is controlled by connecting the exhaust manifold and the intake manifold with a pipe to which a control valve is fitted. In an open-loop control system, the valve position is set for the desired EGR rate based on engine parameters, such as throttle position and engine speed. In a closed-loop control system, the valve is adjusted in conjunction with a valve position sensor and a pressure sensor. The differential pressure is measured across the valve so that the flow rate through the pipe can be measured. The control valve can be adjusted for the desired amount of EGR.

Open-loop control of EGR can become extremely inaccurate. Open-loop control is not robust to parameter variation as changes in the open-loop system are directly seen in the output. Over time, particulate matter from the exhaust gas can clog the EGR pipe and control valve. As the valve and pipe become clogged, the amount of EGR reaching the intake manifold will be lower than expected. Closed-loop control can compensate for changes in valve performance due to clogging. However, the pressure measurement by the pressure sensor is only valid during steady-state operation. EGR rate predictions can be complicated during transient engine operation. Even for short duration EGR changes, there can be an significant increase in unburnt hydrocarbons[1]. A fast response, real time EGR rate measurement method is desirable to optimize engine emissions.

There are a few measurement methods that have been used to measure EGR in real time. Non-dispersive infrared (NDIR) CO_2 sensors have been used to measure the EGR in intake manifolds[3,4], where the EGR rate is determined by:

$$EGR = \frac{CO2_{intake}}{CO2_{exhaust}} \tag{4.1}$$

where $CO2_{intake}$ and $CO2_{exhaust}$ are the concentrations of carbon dioxide in the intake manifold and exhaust manifold, respectively. These NDIR-based methods have fast response times (on the order of 1 ms) and good accuracy[3]. However, NDIR sensors are extremely expensive (~\$100,000[5]) and thus not currently feasible for production vehicles.

Another EGR measurement method is the use of a thermal anemometer, which operates on a similar principle as a hot wire anemometer[6]. This sensor has shown that it has adequate accuracy and time response, but there are questions about manufacturability, cost and long-term accuracy.

Previously it has been shown that the discrete acoustic wave and phase detection (DAWPD) method can be used to measure the sound speed of a gas mixture (see Chap. 3). The DAWPD method can also be used to measure the EGR rate in vehicles. A sensor using the DAWPD method can be inexpensive (on the order of a few dollars in mass production) and have a very fast response time.

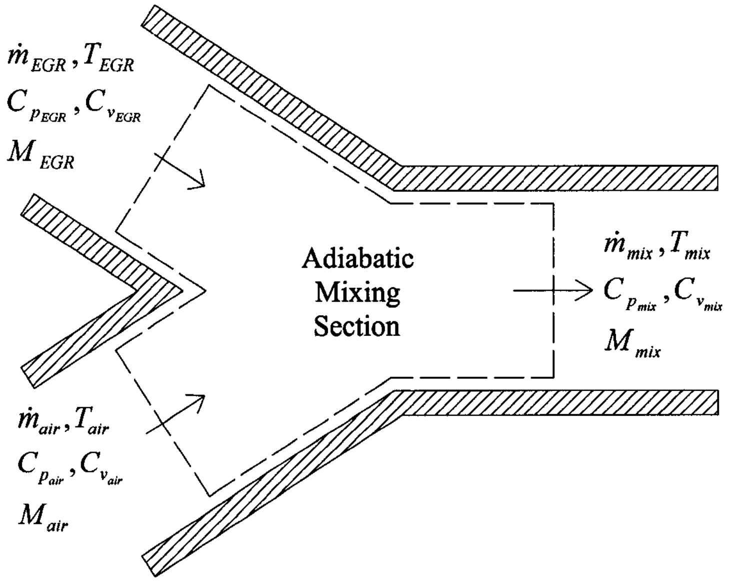

Figure 4.1: Schematic of Mixing of Exhaust Gas and Fresh Intake Air

4.3 Theory of EGR Measurement by Sound Speed

EGR in the intake manifold of an internal combustion engine can be measured by the sound speed of the intake mixture. A change in sound speed is caused by a large increase in the temperature of the intake mixture due to an increase in EGR.

The relationship between EGR rate and temperature can be derived by applying the conservation of mass and conservation of energy across an adiabatic mixing section (see Fig. 4.1). For the thermodynamic system shown in Fig. 4.1, the conservation of mass across the mixing section is:

$$\dot{m}_{EGR} + \dot{m}_{air} = \dot{m}_{mix} \tag{4.2}$$

where $\dot{m}$ is the mass flow rate.

Furthermore, the conservation of energy applied across the adiabatic mixing section, neglecting heat loss and potential and kinetic energy changes, results in:

$$\dot{m}_{EGR}h_{EGR} + \dot{m}_{air}h_{air} = \dot{m}_{mix}h_{mix} \tag{4.3}$$

where h is the specific enthalpy.

Substituting Eq. 4.2 into Eq. 4.3 reveals:

$$\dot{m}_{EGR}h_{EGR} + \dot{m}_{air}h_{air} = (\dot{m}_{EGR} + \dot{m}_{air})h_{mix} \tag{4.4}$$

This equation can be simplified to give the mass ratio of EGR flow to air flow, EGR^*:

$$EGR^* = \frac{\dot{m}_{EGR}}{\dot{m}_{air}} = \frac{h_{mix} - h_{air}}{h_{EGR} - h_{mix}} \tag{4.5}$$

For an ideal gas, the change in enthalpy can be approximated by product of the specific heat at constant pressure, C_p, and the change in the temperature. Furthermore, the specific heat at constant pressure of air and exhaust gas is approximately the same, allowing Eq. 4.5 to be expressed only by the temperature of the gases. Therefore, Eq. 4.5 can be simplified to[7]:

$$EGR^* = \frac{C_{p_{air}}(T_{mix} - T_{air})}{C_{p_{EGR}}(T_{EGR} - T_{mix})} \approx \frac{T_{mix} - T_{air}}{T_{EGR} - T_{mix}} \tag{4.6}$$

Traditionally, EGR rates are expressed in the ratio of EGR mass flow to the total mass flow, EGR.[a] Equation 4.7 shows the relationship between EGR^* and EGR, which has been simplified into terms of the temperature of the gases.

$$EGR = \frac{\dot{m}_{EGR}}{\dot{m}_{EGR} + \dot{m}_{air}} = \frac{EGR^*}{1 + EGR^*} \approx \frac{T_{mix} - T_{air}}{T_{EGR} - T_{air}} \tag{4.7}$$

---

[a] The mass fraction, EGR, and the volume fraction of EGR, y_{EGR}, are approximately the same since the molar mass of the exhaust gas and air are approximately the same.

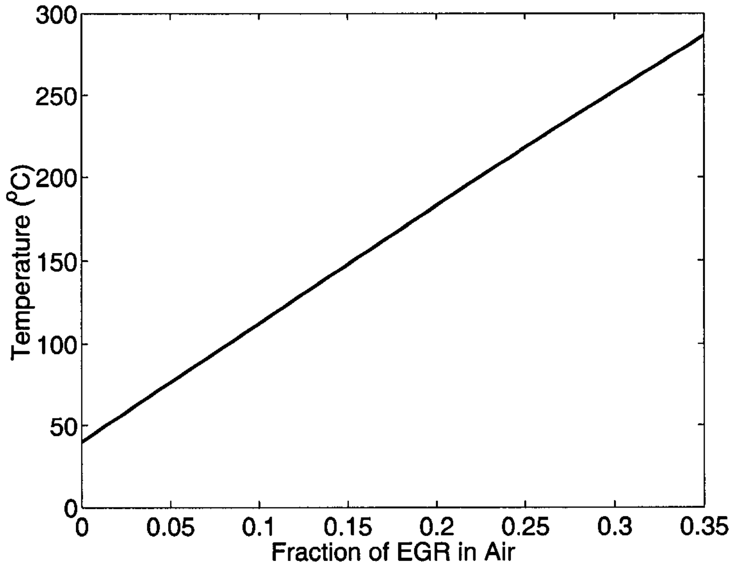

Figure 4.2: Intake Mixture Temperature Variation with Concentration of EGR at 500°C in Air at 20°C where the Exhaust Gas is the Product of a Stoichiometric Combustion of Methane and Air

Equation 4.7 is expressed graphically in Fig. 4.2, where the temperature of EGR and air are 500°C and 20°C, respectively; and the exhaust gas is the product of a stoichiometric combustion of methane and air. The figure shows that even small amounts of EGR can greatly increase the temperature of the intake mixture.

Since the addition of EGR in the intake manifold increases the temperature of the intake mixture, the sound speed of the intake mixture can be used to determine the amount of EGR in the mixture. The advantage of a sound speed measurement compared to a traditional temperature measurement (ie. thermocouples) is that the sound speed measurement have much faster response times, and are more durable.

For an ideal gas, the sound speed can be calculated using Eq. 4.8:

$$c = \sqrt{\frac{\gamma RT}{M}} \tag{4.8}$$

where R is the universal gas constant, T is the temperature, M is the molecular weight and γ is the ratio of specific heat at constant pressure, C_p, to the specific heat at constant volume, C_v.

For a binary mixture of intake air and EGR Eq. 4.8 the sound speed can be found from Eq. 4.9:

$$c = \sqrt{\frac{RT_{mix}(y_{EGR}C_{p_{EGR}} + (1 - y_{EGR})C_{p_{air}})}{(y_{EGR}M_{EGR} + (1 - y_{EGR})M_{air})(y_{EGR}C_{v_{EGR}} + (1 - y_{EGR})C_{v_{air}})}} \tag{4.9}$$

Changes in the air-fuel ratio (A/F) in engines can cause changes in the molecular mass and specific heats of the exhaust gas. However, stoichiometric engines will maintain a constant A/F ratio during engine operation. Equation 4.9 can be further simplified by the fact that the molecular mass and specific heats for EGR and air are approximately the same. With this simplification, the sound speed of the intake mixture in a stoichiometric engine can be expressed as:

$$c \approx \sqrt{\frac{C_{p_{mix}}}{C_{v_{mix}}}\frac{RT_{mix}}{M_{mix}}} \tag{4.10}$$

The sound speed of a mixture of EGR and air can be expressed as a function of the fraction of EGR in the mixture when Eq. 4.7 is substituted for the mixture temperature:

$$c \approx \sqrt{\frac{C_{p_{mix}}}{C_{v_{mix}}}\frac{R}{M_{mix}}\left(T_{air} + EGR(T_{egr} - T_{air})\right)} \tag{4.11}$$

Figure 4.3 graphically represents Eq. 4.9. The figure shows that even small amounts of EGR can greatly increase the sound speed of the intake mixture, just as the temperature was shown to increase. Therefore, sound speed measurement can be used to measure external EGR in an internal combustion engine.

The range of sound speeds that could be encountered in the intake manifold will depend on the temperature of the intake air, the temperature of the exhaust gas and the EGR rate. In general, the intake air can range in temperatures from -40 to 40°C,

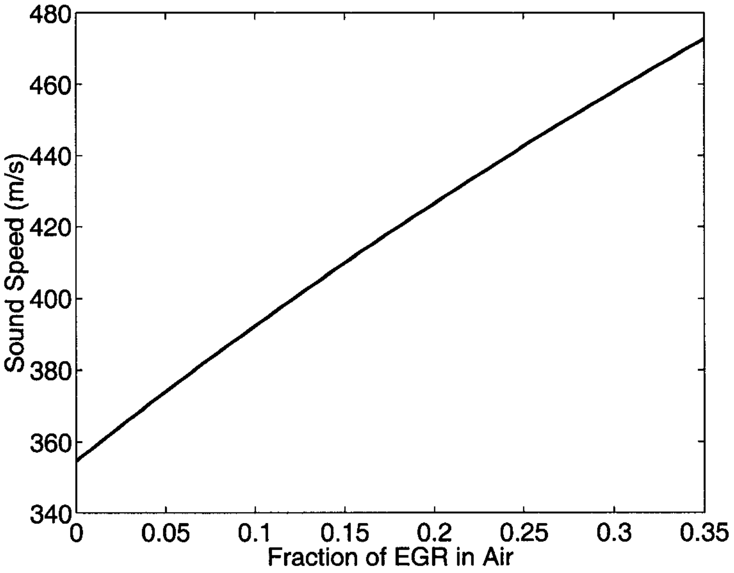

Figure 4.3: Sound Speed Variation with Concentration of EGR at 500°C in Air at 20°C where the Exhaust Gas is the Product of a Stoichiometric Combustion of Methane and Air

while exhaust temperatures can be as high as 700°C. Also, EGR rates can range from 0 to 35%. An acoustic EGR sensor must be able to measure an range of sound speeds from 300 m/s (pure air at -40°C) to 480 m/s (a mixture of air at 40°C and 35% EGR at 700°C) as found from Eq. 4.11.

4.4 Experimental Setup

The theory of EGR measurement using acoustic methods was tested using the DAWPD sensor described in Chap. 2. The experimental set-up is shown in Fig. 4.4. A certified fuel research (CFR) engine (# CFR-48) was used for the experiment and is described in Table 4.1. The CFR engine was controlled with a Digalog dynamometer controller (# 1022A) from which the engine speed could be set for any throttle position. For this experiment the engine was run at 800 rpm. The CFR engine operated on natural gas supplied directly from the building supply. The amount of natural gas was controlled

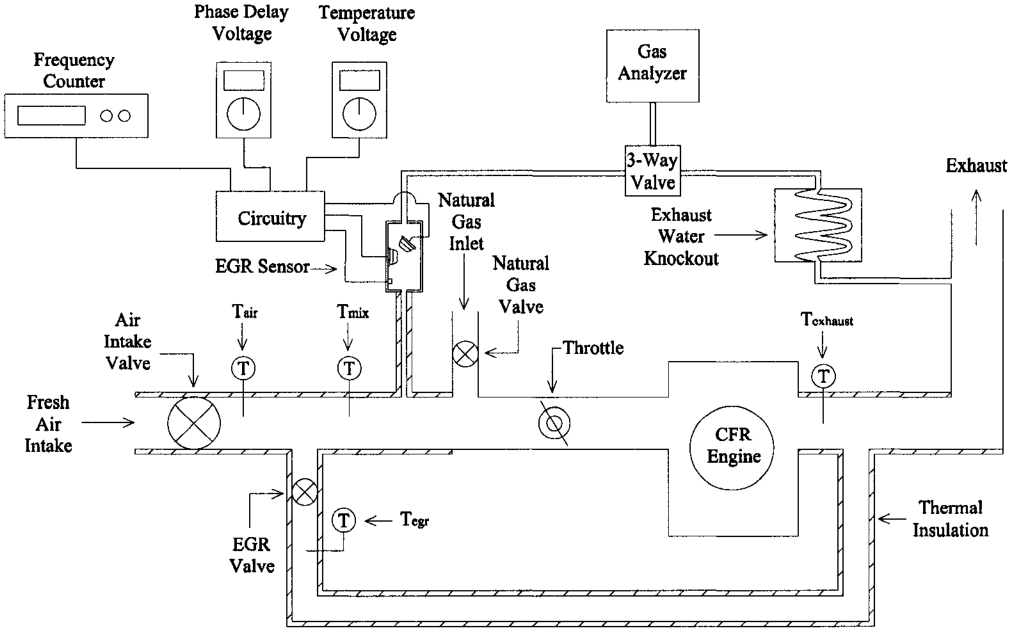

Figure 4.4: Schematic of EGR Experimental Setup

manually with a 1/4" natural gas gate valve (see Fig. 4.4). A Snap-On emission gas analyzer (# MT3500) measured the composition of the exhaust gas. The CFR engine ran at a stoichiometric A/F ratio by adjusting the fuel flow rate so that the amount of CO and O_2 in the exhaust was minimized. For accurate CO_2 measurements with the gas analyzer, water vapour must be removed from the sample line. The Snap-On analyzer uses NDIR detectors. The infrared absorption of water vapour is similar to that of CO and CO_2, so water vapour present in the sample will result in a inaccurate measurement with an NDIR detector. For this reason an exhaust water knockout was used for the exhaust sample. A water knockout was not needed for the intake mixture since the water vapour condensed in the intake manifold and in the sample line.

The EGR rate was controlled by an EGR supply line with a 1" gate valve (EGR valve). The EGR supply line (1" diameter) was insulated to reduce the heat loss of the exhaust gas. The EGR rate was controlled by adjusting the EGR valve or the 1-1/2" gate valve for the fresh air intake (air intake valve). The EGR rate in

Table 4.1: Certified Fuel Research Engine Description

Specification	Value
Displacement	0.6 L
Cylinders	1
Compression Ratio	8.68
Valves	2
Fuel	Natural Gas

the intake manifold was calculated by measuring the amount of CO_2 in the intake manifold and dividing it by the amount of CO_2 in the exhaust (see Eq. 4.1).

For theory verification, the EGR was also measured using the temperature method described in Sec. 4.3. For this method, the intake temperature (T_{air}), EGR temperature (T_{EGR}), mixture temperature (T_{mix}) and exhaust temperature (T_{exhaust}) was measured with thermocouples. All thermocouples used were type K and were wired to a thermocouple multi-channel digital temperature indicator (Omega #DP462). The T_{mix}, T_{air} and T_{EGR} thermocouples were 1/16" probe-type thermocouples with exposed junctions (Alltemp #A6-16-K-ESS), and the T_{exhaust} thermocouple had a 1/8" diameter probe with a grounded junction (Omega #KQSS-18G).

During testing the EGR temperature measurement was always lower than expected. This was due to intake air mixing into the EGR supply line. During the exhaust stroke of the single cylinder CFR engine, the inlet and exhaust valves are both open for a brief time. While the inlet valve is open, the exhaust gas in the cylinder is pushed out the inlet valve. This displaces the air in the intake manifold, causing the intake gas mixture near the EGR valve to be pushed into the EGR line (see Fig. 4.5). For the model described in Sec. 4.3 the temperature measurements must be made outside the mixing region. Thus, for experimental purposes the intake temperature measurement was located outside of the mixing region. Also, the EGR temperature measurement (T_{EGR} in the figure) could not be used due to mixing, so the exhaust temperature (T_{exhaust} in the figure) measurement was used for the measurement of the EGR temperature. As discussed in Sec. 4.3, the model has assumed an adiabatic mixing region. This assumption will not be valid since the mixing region is relatively large with a large surface area. The large surface area will result in high amounts of heat loss. This will result in the EGR measurements being lower than expected since the temperature of the intake mixture will be lower due to the heat transfer from the EGR line. Insulation was added to the EGR line and mixing region to reduce the heat transfer.

Also, the temperature measurements must be taken at steady-state since changes in EGR rates will change the thermal equilibrium and heat transfer rates, resulting in inaccurate measurements in transient conditions. For a non-adiabatic model, Eq. 4.3 must be expressed as:

$$\dot{m}_{EGR}h_{EGR} + \dot{m}_{air}h_{air} = \dot{m}_{mix}h_{mix} + \dot{Q}_{out} \tag{4.12}$$

where $\dot{Q}_{out}$ is the heat transfer from the mixing region into the environment. During transient EGR changes, the heat transfer rate ($\dot{Q}_{out}$) will also change. The measured EGR rate will differ from the actual EGR rate if the heat transfer rate does not remain constant. Once the system reaches thermal equilibrium the heat transfer rate will be constant allowing for a stable EGR rate measurement.

The DAWPD sensor was attached to the intake manifold with insulated 1/4" tubing. The placement of the sampling point was located very close to the mixture temperature thermocouple, T_{mix}. Ideally, the prototype sensor would be placed directly in the intake manifold; however, the prototype sensor was too large to be placed in the intake manifold. In a commercial application, a MEMS (Micro-Electro-Mechanical System) sensor could be used to fit into the intake manifold (see Chap. 2).

The gas mixture in the intake manifold was drawn through the prototype sensor by the pump in the gas analyzer. The sensor output voltage and the temperature voltage

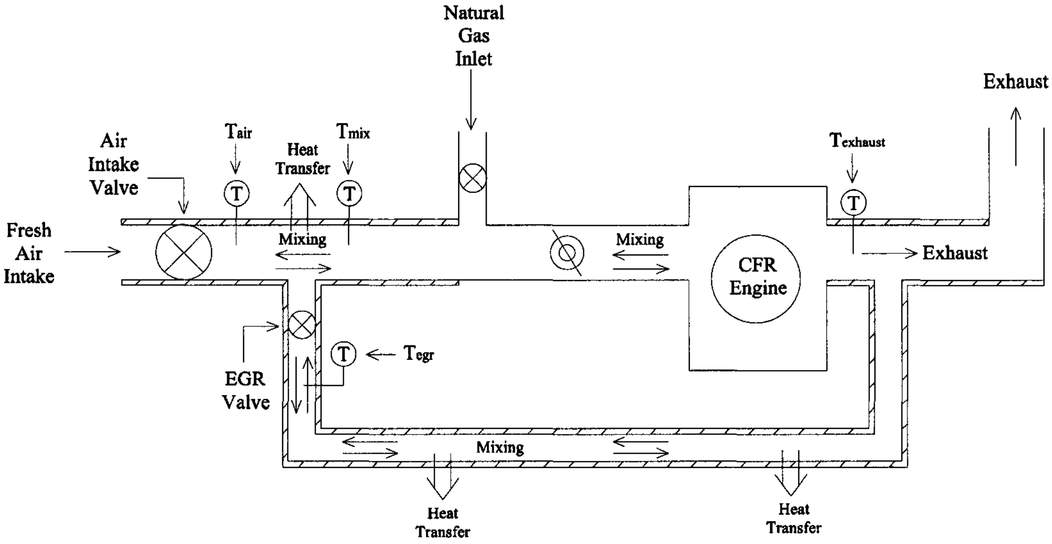

Figure 4.5: Diagram of Exhaust Gas Mixing and Heat Loss

was recorded for each EGR rate. Since the intake mixture was drawn through the tubing and sensor, the temperature in the sensor would be lower than that measured by the T_{mix} thermocouple. This resulted in a less sensitive measurement because there was a smaller temperature change for a change in EGR rate.

As discussed in Sec. 2.5.2, temperature changes of the ultrasonic transducers will result in inaccurate measurements due to resonant frequency and driving frequency mismatch. To compensate for this mismatch, the driving frequency was changed to match the resonant frequency for each measurement. The correlation between the resonant frequency and temperature was found by measuring the resonant frequency for various temperatures as described in Sec. 2.6.5. From these measurements, a curve was found which described the resonant frequency as a function of temperature (see Fig. 4.6). For each measurement with the prototype sensor the temperature in the sensor was recorded, then the driving frequency was adjusted to match the resonant frequency of the transducers (from the resonant frequency curve found in

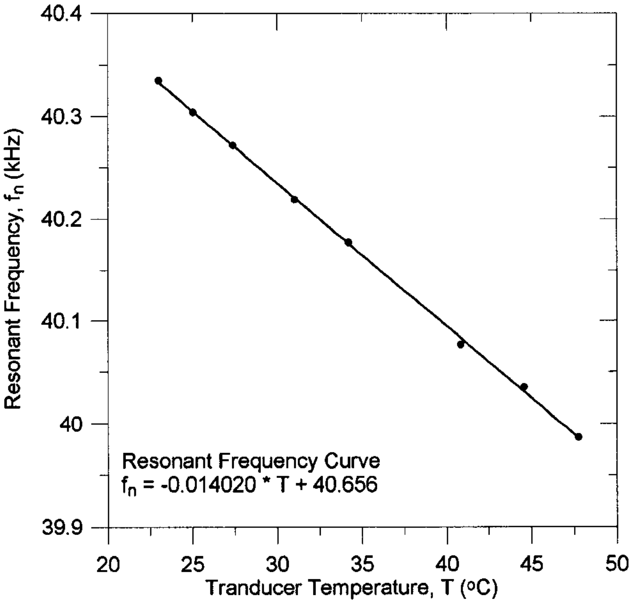

Figure 4.6: Temperature Dependance of the Resonant Frequency of the Ultrasonic Transducers

Fig. 4.6). After the frequencies were matched, the output voltage of the sensor could be recorded.

4.5 Experimental Results

The theory of exhaust gas recirculation measurement was verified using experimental results. The experimental results show that the DAWPD method can be used to measure EGR with adequate accuracy and range.

A convenient method to compare theoretical and experimental measurements were to calculate the sound speed of the intake mixture as a function of the fraction of EGR. Figure 4.7 compares the experimental and theoretical measurements. The theoretical sound speed is calculated by Eq. 4.11. The sensor output voltage can be related to the sound speed by calibrating the prototype sensor with gases of known sound speed (a mixture of nitrogen and methane for instance). As expected, the experimental data is consistently lower than the theoretical data. As discussed in Sec. 4.4, the

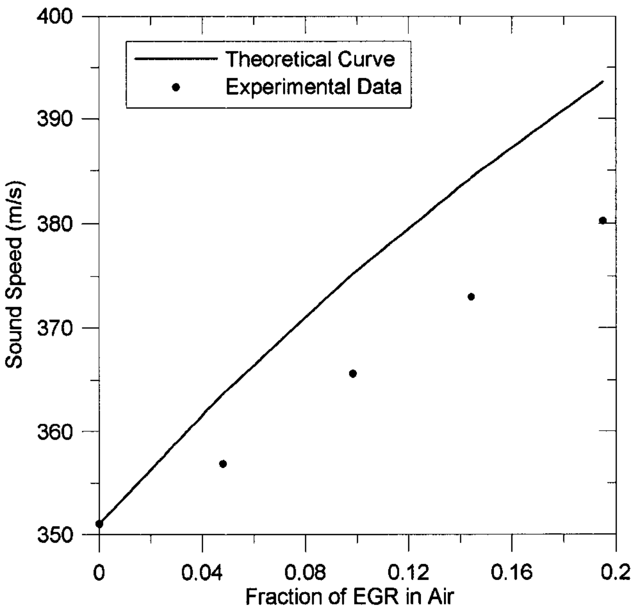

Figure 4.7: Comparison of Theoretical and Experimental Data for the Prototype EGR Sensor

heat transfer from the exhaust line to the environment will result in a lower mixture temperature that is predicted by the adiabatic model. The sound speed of the intake mixture will also be lower because the mixture temperature is lower (see Eq. 4.10).

The static characteristics of the prototype sensor that were examined were: accuracy, repeatability error, calibration error, resolution error and range. The property of interest for the EGR sensor is the concentration of EGR in the intake mixture. Therefore, the sensor characteristics will be expressed in %EGR. These static characteristics are calculated in App. F and summarized in Table 4.2. The calibration curve of the prototype EGR sensor is shown in Fig. 4.8 and the experimental results are shown in App. F. For the calculation of the calibration, repeatability and resolution error; the most conservative, or worst-case, error limit was used. The maximum error measured for each characteristic is given.

The accuracy of the EGR sensor was found to be ±1.13 %EGR. It is unclear what accuracy would be necessary for optimum EGR control. However, it is expected that

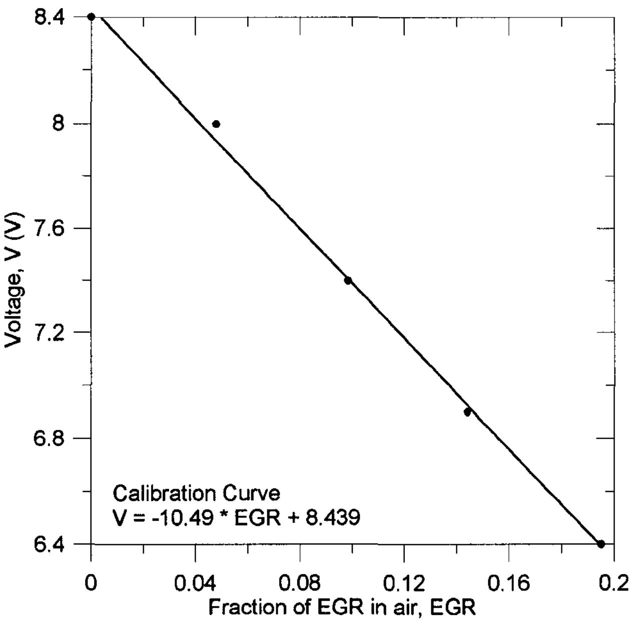

Figure 4.8: Calibration Curve of Prototype EGR Sensor

Table 4.2: Static Characteristics of the Exhaust Gas Recirculation Sensor

Characteristic	Value (% EGR)
Accuracy, δ_{total}	±1.13
Calibration Error, δ_{cal}	±0.62
Repeatability Error, δ_r	±0.64
Resolution Error, δ_{res}	±0.95
Range (as tested)	0 - 20

this accuracy would be adequate for this application.

The range of the prototype was limited by the maximum operating temperature of the piezoelectric transducers used in the prototype. The transducers can only be operated to a maximum temperature of 60°C. At high EGR rates, the temperature of the intake mixture can be much higher than the maximum operating temperature. At EGR rates of 20% the temperature in the sensor reached 52°C, which is relatively low considering that the temperature in the intake manifold was 97°C. Therefore, the experimental testing was limited to 0 - 20% EGR rates. For commercial applications the sensor would be placed directly inside the intake manifold, where the temperature of can reach 250°C with high amounts of EGR. Therefore, different ultrasonic transducers which could operate over a range of temperatures from -40 to 250°C would be required.

4.6 Improvements for a Commercially Successful EGR Sensor

Further modifications are needed to make a commercially successful EGR sensor. The current EGR sensor prototype was limited by its size, lower temperature rating, temperature dependance and relatively large air and EGR mixing section. The sensor performance could be improved by using micro-sized, high temperature, MEMS ultrasonic transducers in a near-adiabatic mixing section.

First, the size of the prototype sensor did not allow it to be placed in the intake manifold. MEMS transducers are required to make a sensor small enough to fit inside the intake manifold. Placing the sensor inside the manifold will result in a more accurate sensor since the sensitivity of the sensor will increase because the intake mixture temperature will be higher.

Second, the natural frequency of the transducers that were used in the prototype was temperature dependant. This results in large errors as the natural frequency deviates from the driving frequency (see Sec. 2.7.2). This was compensated for by using resonant frequency matching. For a commercial sensor, MEMS transducers could be used so that the transducers are not driven near resonance, so that changes in frequency ratio will only produce small phase angle changes..

Third, the range of the prototype sensor was limited by the maximum operating temperature of the ultrasonic transducers. MEMS transducers can have high operating temperatures, allowing the prototype sensor to be operated in the high temperature conditions that exist in an intake manifold.

Fourth, the intake air and EGR gas mixing section should be small enough so that it could be considered adiabatic. In the experiment, back-flow from single cylinder CFR engine caused mixing through out the EGR line. In multi-cylinder engines the back-flow will be considerably less because the back-flow from one cylinder will be consumed by another cylinder starting the intake stroke. Therefore, the mixing section will be small allowing measurements to be made in real-time instead of requiring a steady-state thermal equilibrium measurement for adequate accuracy.

4.7 Conclusions

EGR sensors can be used to improve the performance of internal combustion engines. Various EGR measurement methods can be used; however, a durable, fast-response and cost effective method is the DAWPD acoustic technique. The DAWPD sensor was able to measure EGR in steady-state conditions with adequate accuracy ($\pm 1.13\%$ EGR).

Modifications must be made for a commercial sensor to be developed. These modifications include: i) MEMS transducers for a smaller sensor to fit inside the intake manifold, ii) transducers with little resonant frequency change, or be non-resonant devices, iii) transducers which can operate in high temperature environments and iv) operation in a small mixing section so that measurement could be made in real-time.

REFERENCES

[1] J. B. Heywood, *Internal Combustion Engine Fundamentals.* McGraw Hill, Inc, 1988.

[2] J. R. Mondt, *Cleaner Cars - The History and Technology of Emission Control Since the 1960s.* Society of Automotive Engineers, 2000.

[3] C. Sutela, N. Collings, and T. Hands, "Real time CO_2 measurement to determine transient intake gas composition under EGR conditions," *Society of Automotive Engineers*, 2000. SAE Paper 2000-01-2953.

[4] M. Hall and P. Zuzek, "Fiber optic sensor for time-resolved measurements of exhaust gas recirculation in engines," *Society of Automotive Engineers*, 2000. SAE Paper 2000-01-2865.

[5] M. Peckham, "Quote for fast response HC, NO_x, CO, CO_2 and particulate instruments." Personal Communication, 2003. Cambustion Ltd.

[6] M. Hall and P. Zuzek, "Cooled EGR rate measurement with a thermal anemometer for EPA02 heavy duty diesel engine emission control," *Society of Automotive Engineers*, 2003. SAE Paper 2003-01-0263.

[7] C. R. Koch, "EGR fraction estimate using temperature." Personal Communication, 2002.

CHAPTER 5

CONCLUSIONS

5.1 Thesis Conclusions

THIS thesis presented the development and possible applications for the discrete acoustic wave and phase detection method. The following conclusions were reached from the development of the DAWPD method:

1. The DAWPD method can be used to measure sound speeds over path lengths on the order of one wavelength.
2. Sources of error in the DAWPD method were identified as:
    - Reflections between ultrasonic transducers
    - Reflections from the environment
    - Changes in the frequency ratio, $\frac{f}{f_n}$, due to temperature and age effects
3. The DAWPD method can be used to measure the quality of a natural gas fuel with a sound speed accuracy of ±1.65 m/s.
4. The DAWPD method can be used to measure the concentration of a variable gaseous fuel to an accuracy of ±6.31% H_2.

5. The DAWPD method can be used to measure the external exhaust gas recirculation in an automotive engine to an accuracy of ±1.13% EGR.

The development of the DAWPD method showed that sound speed measurements can be made over small paths with high accuracy. The small path length allows this type of sensor to be small enough to fit into an engine compartment.

Sources of error were identified during the development of the DAWPD method. It was found that ultrasonic reflections from the environment ie. walls) and between transducers cause error in the measurement system. Reflections from the walls of the sensor can be reduced by placing acoustic insulation of the walls of the sensor. Reducing reflections between the transducers can be accomplished by:

i. increasing the distance between transducers,

ii. angling the transducers,

iii. offsetting the transducers and,

iv. decreasing the diameter of the transducers.

Another source of error was changes in the frequency ratio ($\frac{f}{f_n}$) of the ultrasonic transducers. Changes in the frequency ratio can occur from a change in driving frequency (f) of the transducers due to drift in the electronic circuitry. A more common cause of changes in the frequency ratio occurs when the resonant frequency (f_n) changes due to temperature or age effects. Error due to frequency ratio changes can be reduced by:

i. matching the driving frequency and resonant frequency with the use of a feedback system,

ii. maintaining the temperature of the transducers,

iii. or operating at frequencies well below resonance (with broadband (low Q_m) transducers).

It was found that there is a correlation between sound speed and the quality of natural gas or peak-shaved natural gas. The DAWPD method was shown to be able to measure the quality of a natural gas fuel for NGVs with adequate accuracy and range.

It was also found that the concentration of binary gas mixture can be determined by measuring the sound speed of the mixture. The DAWPD method was shown to measure the concentration of a mixture of hydrogen and methane for a VGF vehicle with accuracy adequate for the application. The range of the sensor was limited by poor acoustic impedance matching between the prototype transducers and high hydrogen concentration mixtures. The range of the prototype sensor could be improved by simply using transducers better acoustically matched to that particular medium.

The DAWPD method was also found to be able to measure EGR in a combustion engine. The DAWPD sensor was able to measure EGR in steady-state conditions with adequate accuracy. It was also found that modifications are necessary for proper performance in a commercial automotive application. First, smaller transducers are needed so that the sensor could easily be mounted inside the intake manifold. Second, non-temperature dependant transducers are needed so that changes in the temperature of the transducers does not change the resonant frequency of the transducer. Third, high temperature transducers are required so that the sensor can measure large amounts of EGR. Fourth, the air and EGR mixing section must be small and near-adiabatic so that measurements can be made in real-time.

5.2 Further Work

Through out the development and testing of the DAWPD method, it was found that the performance was limited by the operating characteristics of the ultrasonic transducers. The major limiting characteristics of the transducers were:

i. size,

ii. temperature dependance of the resonant frequency,

iii. maximum operating temperature,

iv. and poor acoustic impedance matching to the gas mediums of interest.

Many of these problems can be attributed to type of piezoelectric transducers that was used, which was an piezoceramic transducer. Many types of transducers are commercially available, such as piezoceramic, electrostatic, composite, and piezopolymer[1]. In recent years, considerable research has been conducted on MEMS-type ultrasonic transducers[2–4]. MEMS-type transducers could be able to over come some of the problems mentioned above.

First, the advantage of MEMS-type transducers is that they can be constructed to micro- and millimeter dimensions. The size of the transducer is important for two reasons: i) the smaller the transducer, the less reflections there will be between the transducers and ii) smaller transducers allow for small sensors. As discussed in Sec. 2.7, smaller path lengths can be used with small diameter transducers. With very small MEMS transducers the total sensor design could be much smaller, allowing the sensor to be placed in spaces such as automotive gaseous fuel regulators (for fuel measurement) and intake manifolds (for EGR measurement). In general, smaller transducer diameters result in larger natural frequencies, allowing the sensor to be operated at higher frequencies which allows for smaller path lengths.

Second, MEMS transducers also have the advantage of being having lower Q_m factors. The piezoceramic transducers tested in this thesis were highly resonant. The transducers were driven at resonance and small changes in the resonant frequency created large errors in the measurement system. However, the inherently high natural frequency and low Q_m factors of the MEMS devices allow the transducers to be operate much lower than the natural frequency of the transducer. Also, the improved impedance matching of light weight MEMS diaphragm devices with air translates to a higher effective sensitivity. These two factors should make it possible to design a non-resonant sensor with acceptable sensitivity. This is a subject for further work in the area.

Third, MEMS transducers can have lower acoustic impedances than piezoelectric transducers. Piezoelectric materials have impedances many orders of magnitude higher than the impedances of gases, therefore, matching layers are used so that transducer impedances are much closer to air. This however compromises bandwidth and often the proper materials cannot be found. MEMS transducers have acoustic impedances much closer to that of gases. Therefore, MEMS transducers would be ideal for measuring fuels high in hydrogen which have very small acoustic impedances.

Fourth, MEMS transducers can withstand higher operating temperatures than piezoelectric transducers can. Piezoelectric transducers generally cannot operate at temperatures higher than 80°C, which makes them ill-suited for automotive applications. For example, piezoelectric transducers are unsuitable for fuel quality measurements in automotive gas regulators because they are heated by engine coolant and frequently operate at temperatures over 100°C. Also, EGR temperatures can approach 300°C. MEMS transducers can operate at temperatures on the order of hundreds of degrees Celsius, making them ideal for automotive applications. Also, the heat transfer in micro-scale devices is inherently fast, making it easier to build in a capability to measure and compensate for temperature effects in the design of a

MEMS device. This is a subject for further work in the area.

REFERENCES

[1] W. Manthey, N. Kroemer, and V. Mágori, "Ultrasonic transducers and transducer arrays for applications in air," *Meas. Sci. Technol.*, vol. 3, pp. 249–261, 1992.

[2] L. Rufer, C. Domingues, and S. Mir, "Behavioural modelling and simulation of a MEMS-based ultrasonic pulse-echo system," in *Design, Test, Integration, and Packaging of MEMS/MOEMS 2002. Cannes, France*, pp. 171–182. Vol. 4655.

[3] P. D. Harris, M. K. Andrews, and G. C. Turner, "Ultrasonic transmission and reception from bulk-micromachined transdcuers," *IEEE Transactions on Ultrasonics, Ferroelectrics, and Frequency Control*, vol. 48, no. 1, pp. 224–231, 2001.

[4] I. Ladabaum, X. Jin, H. T. Soh, A. Atalar, and B. T. Khuri-Yakub, "Surface micromachined capacitive ultrasonic transducers," *IEEE Transactions on Ultrasonics, Ferroelectrics, and Frequency Control*, vol. 45, no. 3, pp. 678–690, 1998.

APPENDIX A

UNCERTAINTY ANALYSIS OF SOUND SPEED MEASUREMENT METHODS

A.1 Uncertainty Analysis of Time of Flight Method

The sound speed, c, can be represented as a function of distance and time:

$$c = \frac{d}{t} \tag{A.1}$$

so that,

$$c = f(d, t) \tag{A.2}$$

For calculation proposes a theoretical time-of-flight sensor can be devised. Assuming the sensor has a path length, d, of 10 mm and is operating at a frequency of 40 kHz in air. The error in the distance can be assumed to be the error of the machining tolerance when the part is manufactured, reasonable machining tolerances are ± 5 thousandths of an inch or 1.27×10^{-4} m.

The mean value of the time measurement can be found from rearranging Eq. A.1 so that

$$t = \frac{d}{c} \tag{A.3}$$

where d is the path length between the sending and receiving transducers (0.01 m) and c is the sound speed in air (343 m/s) at standard conditions. Therefore, the mean value of the time variable will be,

$$t = \frac{0.01\text{m}}{343\text{m/s}} = 2.92 \times 10^{-4}\text{s} \tag{A.4}$$

The error in the time dimension is dependent on the type of the transducer used. Most commercially available ultrasonic transducers that operate in the 40 kHz range use mechanical structures to match the impedance of the piezoelectric ceramic to the impedance of air. These devices are resonant in nature, requiring a series of pulses to fully excite the transducer. Figure A.1 shows the build-up of the receiving signal of a ultrasonic transducer. This build-up causes error in the time measurement because there is uncertainty which pulse is the first pulse in the train of sent waves. The build-up period depends on the particular transducer used, however for this error analysis we will conservatively assume a build-up period of one half wavelength (a less conservative estimate being 1 or 2 wavelengths). Therefore at a frequency of 40 kHz the period, and the uncertainty in the time dimension, will be 12.5×10^{-6} s.

To summarize the uncertainty in the distance and time dimensions will be:

$d = 0.01 \pm 1.27 \times 10^{-4}$ m

$t = 2.92 \times 10^{-5} \pm 12.5 \times 10^{-6}$ s

The standard error in c can be found from:

$$\Delta c = \sqrt{(\frac{\partial f}{\partial d}\Delta d)^2 + (\frac{\partial f}{\partial t}\Delta t)^2} \tag{A.5}$$

Therefore,

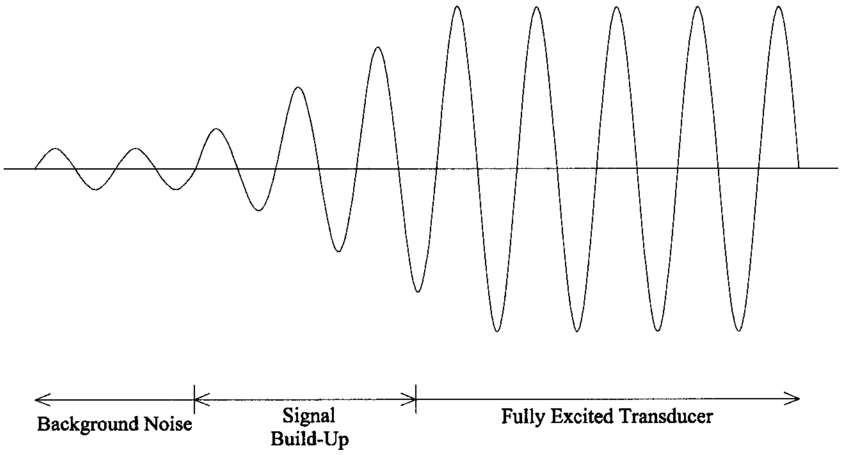

Figure A.1: Signal Build-Up of Receiving Ultrasonic Transducer

$$\frac{\partial f}{\partial d}\Delta d = \frac{1}{t}\Delta d = \frac{1}{2.92 \times 10^{-5}}(1.27 \times 10^{-4}) = 4.35\text{m/s} \tag{A.6}$$

$$\frac{\partial f}{\partial t}\Delta t = \frac{-d}{t^2}\Delta t = \frac{-0.01}{(2.92 \times 10^{-5})^2}(2.5 \times 10^{-5}) = 147\text{m/s} \tag{A.7}$$

Substituting back into Eq. A.5,

$$\Delta c = \sqrt{(4.35)^2 + (147)^2} = 147\text{m/s} \tag{A.8}$$

$$c = 343 \pm 147\text{m/s} \tag{A.9}$$

Notice that the standard error in c is dominated by the error in the time measurement.

A.2 Uncertainty Analysis of Phase Discrimination Method

Using the discrete acoustic wave and phase discrimination method the sound speed, c, can be represented as a function of frequency, path length and phase difference.

$$c = \frac{1}{\frac{\phi}{2\pi f d} + \frac{1}{c_{ref}}} \tag{A.10}$$

so that,

$$c = g(\phi, f, d) \tag{A.11}$$

The standard error in c can be found from,

$$\Delta c = \sqrt{(\frac{\partial g}{\partial \phi}\Delta\phi)^2 + (\frac{\partial g}{\partial f}\Delta f)^2 + (\frac{\partial g}{\partial d}\Delta d)^2} \tag{A.12}$$

As before a theoretical sensor is needed for calculation purposes. Assume that the sensor has the same path length and frequency as above and is operating in air. The reference gas will be methane at standard temperature. Also assume that the error in the electronics is ± 3%.

The error in the phase dimension is highly dependant on ultrasonic wave reflections within the sensor. Reflections from the walls of the sensor enclosure and between the transducers cause constructive and destructive interference of the original ultrasonic wave which alters the phase of the received wave. Figure A.2 depicts an example of a reflection which causes a phase change in the received wave. Figures A.2a and A.2b show the original and reflected wave, respectively. The reflected wave (which has reflected off a wall for example) will have traveled a longer path length and will have a smaller amplitude and will be out of phase of the original wave. The addition of the ultrasonic waves at the position of the receiving transducer will result in a wave of different amplitude and phase of that of the original wave (as seen in Fig. A.2c). The change of phase is proportional to the relative amplitude of the reflected wave and the relative phase difference between the original and reflected wave. For example, if the amplitude of the reflected wave is small compared to the original wave, then the change in phase will be small, thereby reducing the uncertainty in the phase measurement. By reducing the reflections from the walls of the sensor and between the transducers, it has been found experimentally that the uncertainty in the phase measurement can be less than 1%.

Thus for sensor uncertainty calculations the following values can be used:

$c_{ref} = 450$ m/s

$f = 40,000$ kHz $\pm 3\%$

$d = 0.01 \pm 1.27 \times 10^{-4}$ m

$\phi = 0.55\pi$ rad $\pm 1\%$ (where ϕ can be found by solving Eq. A.10 for ϕ)

Therefore,

$$\frac{\partial g}{\partial \phi}\Delta\phi = \frac{\frac{-1}{2\pi f d}}{\left(\frac{\phi}{2\pi f d}+\frac{1}{c_{ref}}\right)^2}\Delta\phi = 0.812\text{m/s} \tag{A.13}$$

$$\frac{\partial g}{\partial f}\Delta f = \frac{\frac{\phi 2\pi d}{(2\pi f d)^2}}{\left(\frac{\phi}{2\pi f d}+\frac{1}{c_{ref}}\right)^2}\Delta f = 2.44\text{m/s} \tag{A.14}$$

$$\frac{\partial g}{\partial d}\Delta d = \frac{\frac{\phi 2\pi f}{(2\pi f d)^2}}{\left(\frac{\phi}{2\pi f d}+\frac{1}{c_{ref}}\right)^2}\Delta d = 1.03\text{m/s} \tag{A.15}$$

Substituting back into Eq. A.12,

$$\Delta c = \sqrt{(0.812)^2 + (2.44)^2 + (1.03)^2} = 2.77\text{m/s} \tag{A.16}$$

$$c = 343 \pm 2.77\text{m/s} \tag{A.17}$$

A.3 Comparison of the Uncertainty of Sound Speed Measurement Methods

The uncertainty in the time of flight measurement method was clearly dominated by error in the time dimension. The uncertainty of this method can be greatly improved by spacing the transducer farther apart, thereby increasing the mean value of t, or

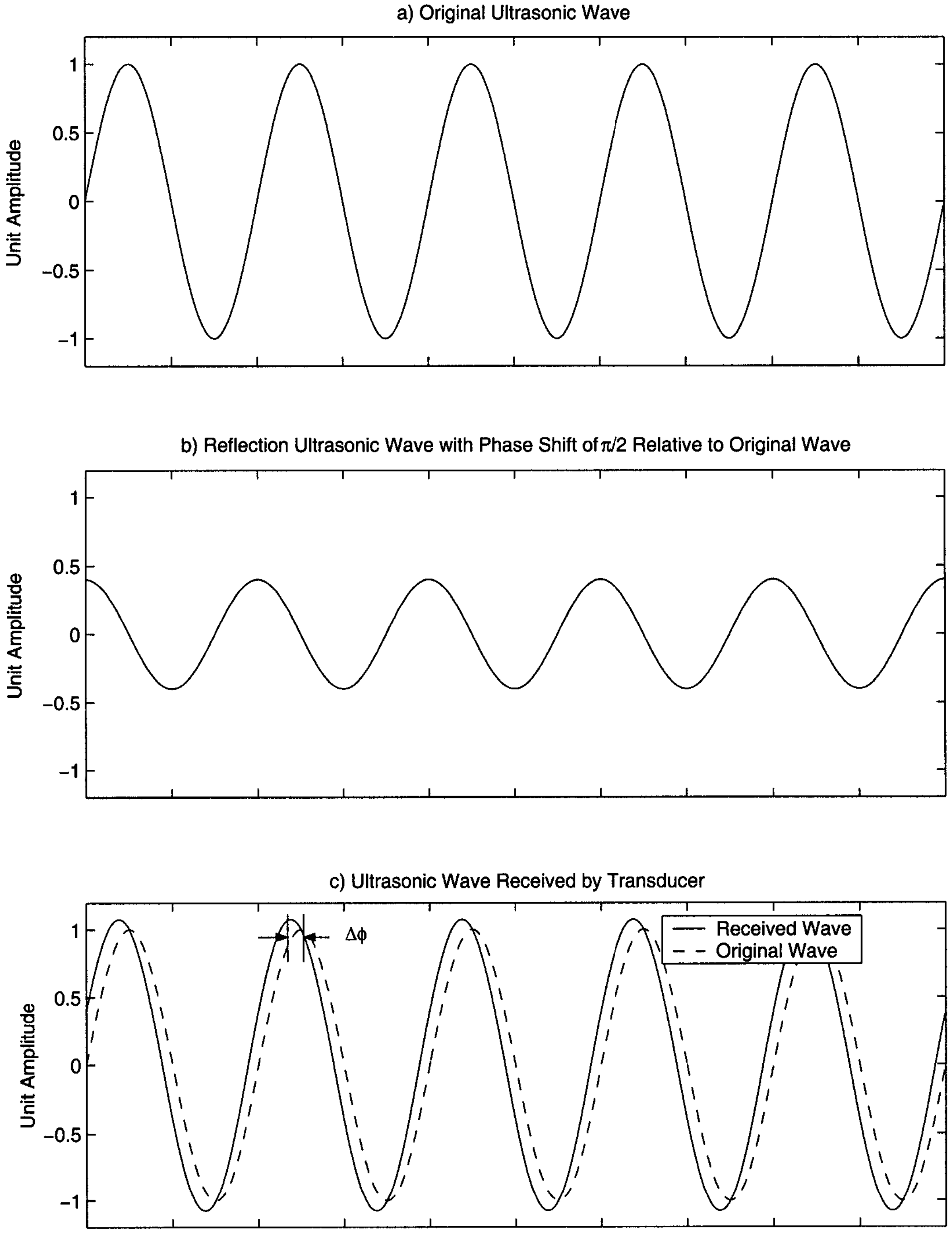

Figure A.2: Interference of Original and Reflected Signal and Resulting Phase Shifted Received Signal by increasing the frequency of the transducer which decreases the uncertainty in t.

In contrast the uncertainty of the DAWPD method varies little with distance and frequency. This shows that for a compact sensor operating in similar conditions, a phase discrimination method will be more accurate than a time of flight method.

APPENDIX B

CALIBRATION OF DASIBI® MULTI-GAS CALIBRATOR

B.1 Introduction

The Dasibi® multi-gas calibrator is used to create gas mixtures. For this project the calibrator is used to create various mixtures of nitrogen, methane and hydrogen. The calibrator's mass flow controllers (MFCs) use the thermal conductivity properties of a gas to measure the mass flow rate. However, the calibrators MFCs, like most MFCs, are calibrated with nitrogen. To use other gases such as hydrogen and methane the Dasibi® must be calibrated so that a correction factor can be found.

B.2 Procedure

The following procedure was used to calibrate the Dasibi® Multi-Gas Calibrator in the University of Alberta Mechanical Engineering Engine Lab.

The bottle of the gas calibrated was placed on a scale (GSE-550, with a range of 60 kg and resolution of 0.02 kg). The scale was connected to a data acquisition system which showed the output of the scale and plots the scale measurement against time. Using the manual controls on the Dasibi® calibrator, gases were passed through the calibrator at various flow rates. For each flow rate, the mass flow was measured over an appropriately long amount of time. The mass flow rate can be found from:

$$\dot{m} = \frac{m_i - m_f}{\Delta t} \tag{B.1}$$

However, the calibrator displays information in standard volumetric flow rate, which can be found from:

$$Q = \frac{\dot{m}}{\rho_{std}} \tag{B.2}$$

where

$$\rho_{std} = \frac{P}{RT} \tag{B.3}$$

and R is the gas constant of the gas of interest, P = 101.3 kPa and T= 298 K.

The actual volumetric flow rate was plotted against the calibrator's indicated volumetric flow rate for various flow rates. Linear regression was used to fit the data points and the correlation coefficient was calculated of the linear best-fit line. The slope of the linear regression equation was the correction factor for the gas of interest.

B.3 Results

The Dasibi® calibrator was calibrated with three different gases: nitrogen, methane and hydrogen. Figure B.1 shows the calibration data for nitrogen, methane and hydrogen.

The slope of the linear regression equation gives the correction factor for each gas. Table B.1 shows the correction factor found from the Dasibi calibration as well as the correction factors normally used with thermal conductivity mass flow controllers.

The correction factors found from the Dasibi® calibration are close to the commonly used correction factors. Differences can be attributed to differences in mass flow controllers.

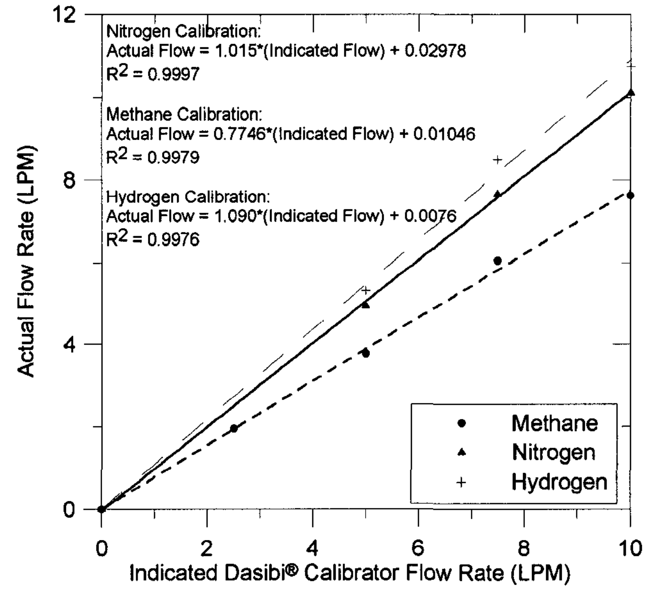

Figure B.1: Calibration Curve of Dasibi® Calibrator with Nitrogen, Methane and Hydrogen

Table B.1: Mass Flow Controller Correction Factors for Various Gases

Gas	Dasibi® Correction Factor	Common Correction Factor
Nitrogen	1.02	1.00
Methane	0.77	0.73
Hydrogen	1.09	1.01

APPENDIX C

SMALL PROTOTYPE CONSTRUCTION AND DRAWINGS

The drawings of the small prototype components are found in this appendix. Figure C.1 shows the assembly of the small prototype. The assembly shows the large transducers in the assembly although the small transducers can be interchanged with this prototype.

The construction of the prototype is basic. Most of the parts can be assembled as shown in the assembly figure, although some construction elements are not shown such as: i) the mounting of the transducers, ii) wire soldering, iii) acoustic insulation, iv) gas sealing and v) temperature sensor.

C.1 Transducer Mounting

The transducers were mounted so that they were electrically isolated and mechanically isolated from vibrations. The transducers were electrically isolated by applying heat-shrink to the transducer leads so that the leads did not touch the transducer mounts. Also, a plastic shim (large and small transducer shim, see Figs. C.12 and C.13) was added to isolate the back of the transducer from the transducer mount to ensure that the transducer would not be grounded to the transducer mount. The transducers, transducer shims and transducer mounts were attached to each other with a silicon rubber sealant. Silicon sealant ensures that the transducer is mechanically isolated from the rigid transducer mount. Therefore, the transducer can vibrate freely without being impeded by the mount. Hard-setting epoxies are not recommended since they do not mechanically isolate the transducer.

C.2 Wire Soldering

Wires are required to connect the leads of the transducers to the electrical pin connectors. A thin gauge braided wire was used so that the receiving transducer could be translated and rotated freely without being impeded by a stiff wire. The wires were soldered to the transducers and the electrical connector with an acid-core solder. The transmitting and receiving transducer leads were soldered to pins 1 and 2 of the electrical pin connectors.

C.3 Acoustic Insulation

Kaowool® board insulation (M Board) was cut 10 mm thick and placed inside the small prototype. The sides and top of the prototype could be insulated; however, the bottom of the sensor could not be insulated since the receiving transducer mount and the position indicator occupied the bottom.

C.4 Gas Sealing

To prevent gases from escaping the sensor, gaskets, sealing tape and some silicon epoxy was used. Gaskets (see Figs. C.4 and C.11) were used to seal the lid, the transmitting transducer mount and the circumference of the receiving transducer's electrical pin connector. Also the interior of the electrical connector was coated with a silicon sealant to ensure the connector did not leak. The slot in the main body of the sensor used to adjust angle and offset was covered with a sealant tape (Polyken Foilmastic Sealant 360-17) to prevent the slot from leaking gas.

C.5 Temperature Sensor

The AD590 temperature sensor was soldered directly to pins 3 and 4 of the electrical pin connector of the receiving transducer. Care was taken to ensure that the pins of the temperature sensor and the transducer wires did not short.

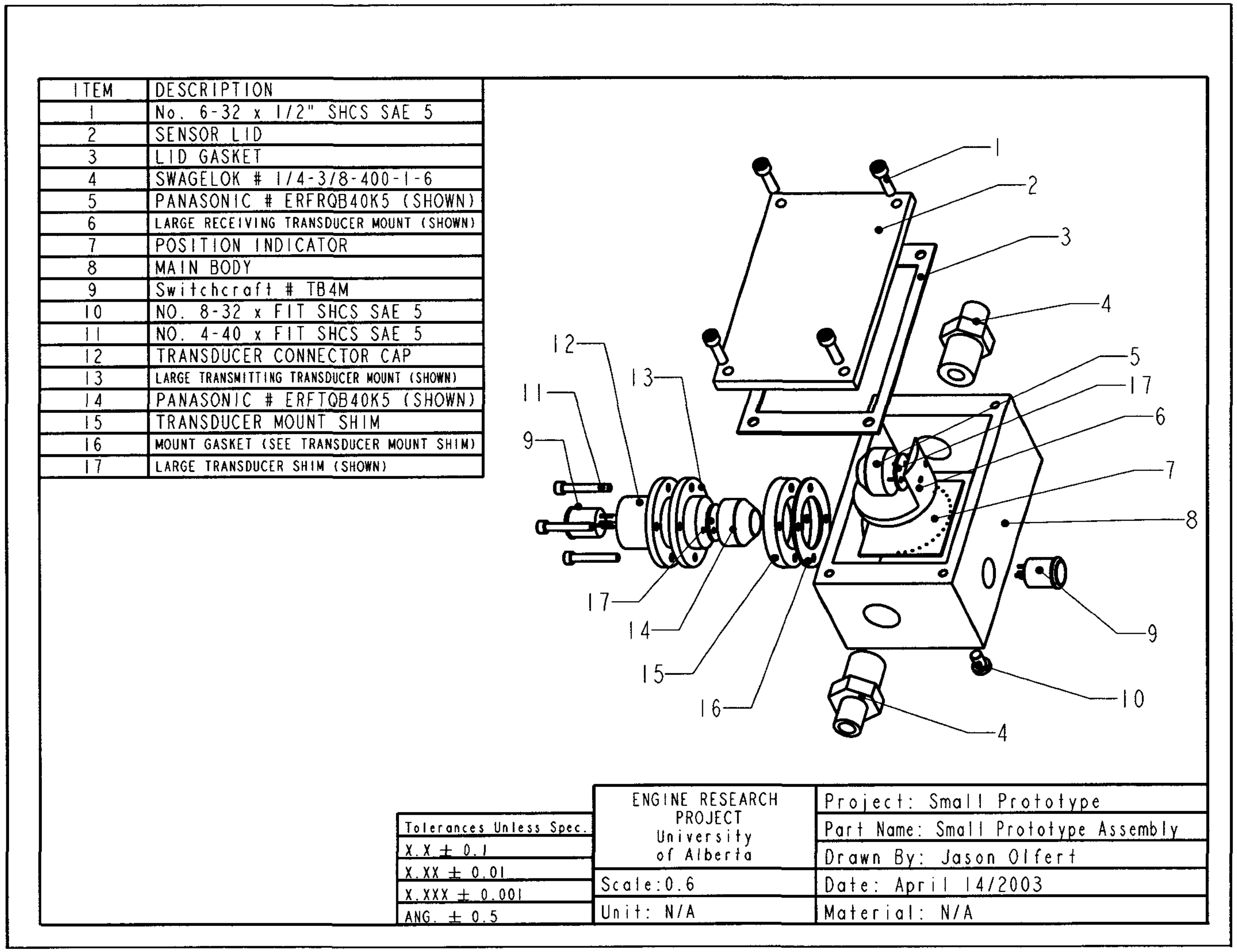

ITEM	DESCRIPTION
1	No. 6-32 x 1/2" SHCS SAE 5
2	SENSOR LID
3	LID GASKET
4	SWAGELOK # 1/4-3/8-400-1-6
5	PANASONIC # ERFRQB40K5 (SHOWN)
6	LARGE RECEIVING TRANSDUCER MOUNT (SHOWN)
7	POSITION INDICATOR
8	MAIN BODY
9	Switchcraft # TB4M
10	NO. 8-32 x FIT SHCS SAE 5
11	NO. 4-40 x FIT SHCS SAE 5
12	TRANSDUCER CONNECTOR CAP
13	LARGE TRANSMITTING TRANSDUCER MOUNT (SHOWN)
14	PANASONIC # ERFTQB40K5 (SHOWN)
15	TRANSDUCER MOUNT SHIM
16	MOUNT GASKET (SEE TRANSDUCER MOUNT SHIM)
17	LARGE TRANSDUCER SHIM (SHOWN)

Tolerances Unless Spec.
X.X ± 0.1
X.XX ± 0.01
X.XXX ± 0.001
ANG. ± 0.5

ENGINE RESEARCH
PROJECT
University
of Alberta
Scale:0.6
Unit: N/A

Project: Small Prototype
Part Name: Small Prototype Assembly
Drawn By: Jason Olfert
Date: April 14/2003
Material: N/A

Figure C.1: Drawing of Small Prototype Assembly

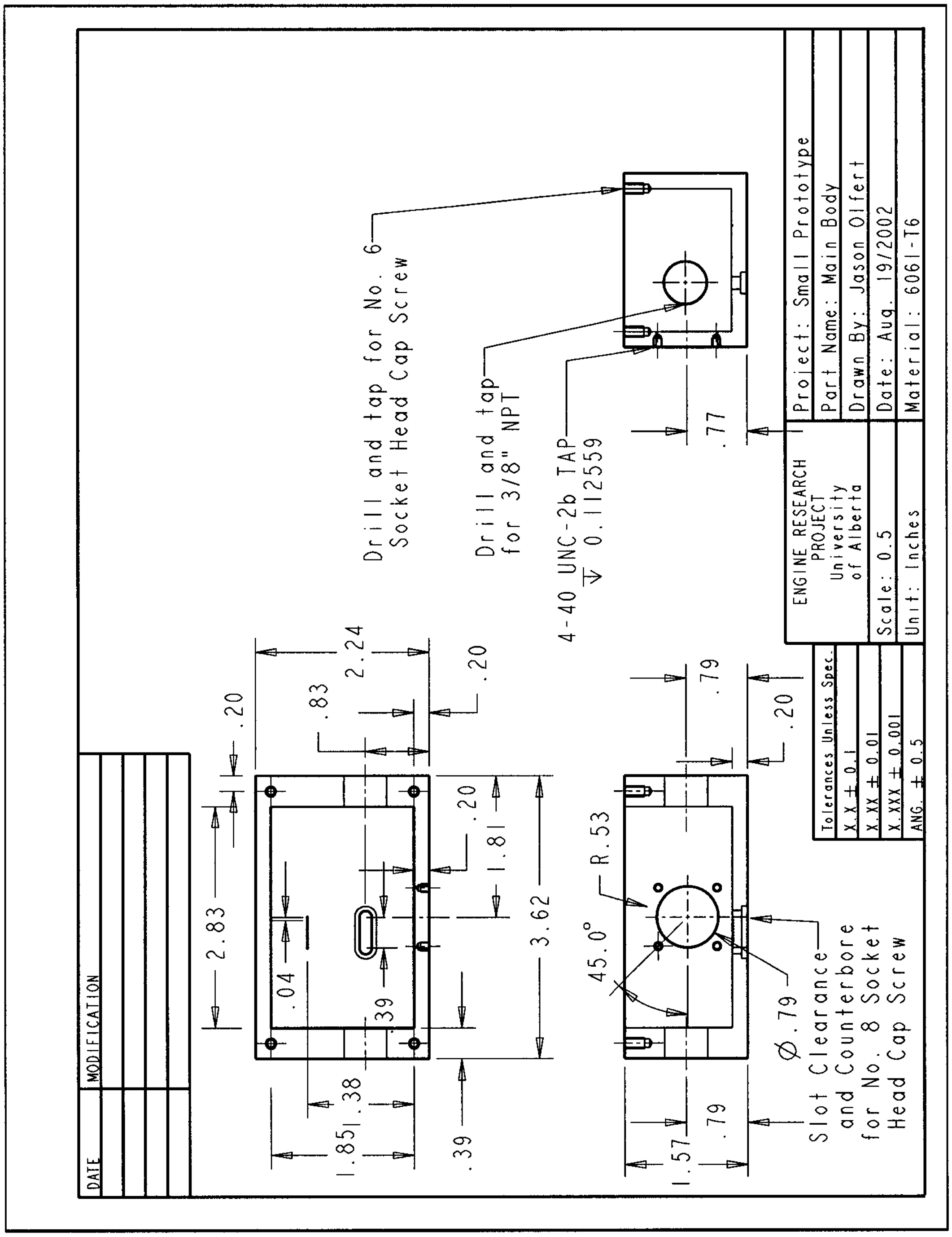

Figure C.2: Drawing of Main Body of Small Prototype

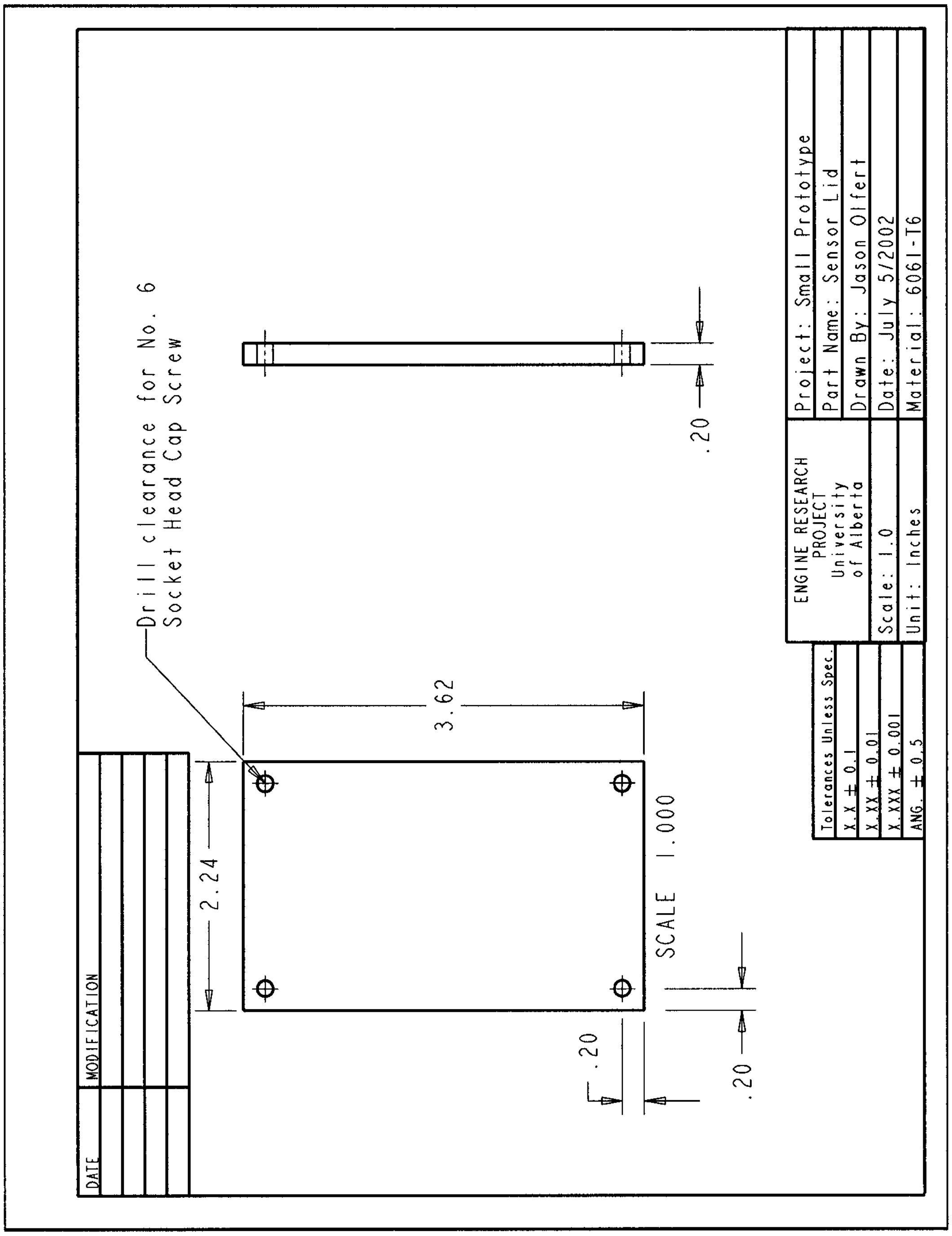

Figure C.3: Drawing of Sensor Lid of Small Prototype

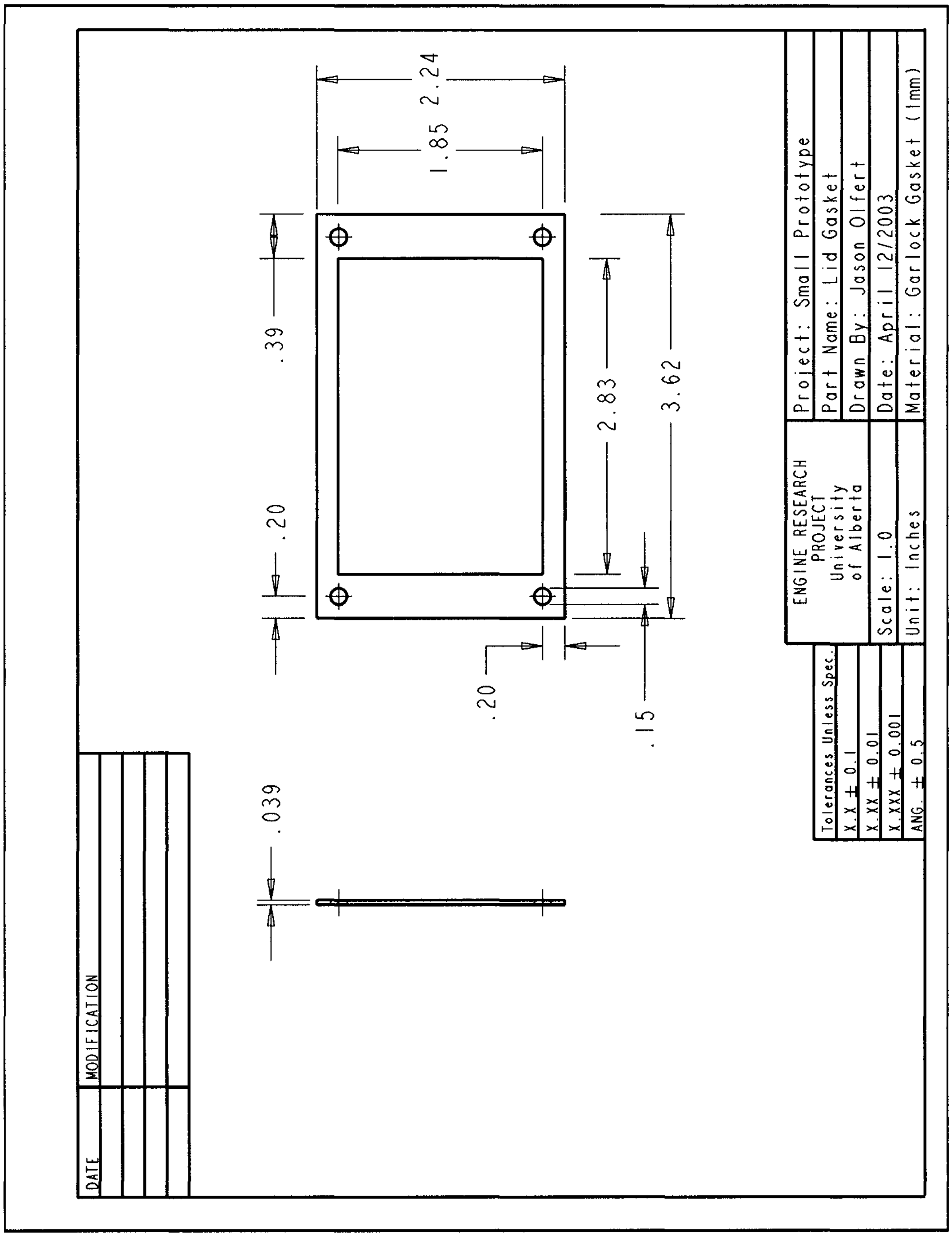

Figure C.4: Drawing of Sensor Lid Gasket of Small Prototype

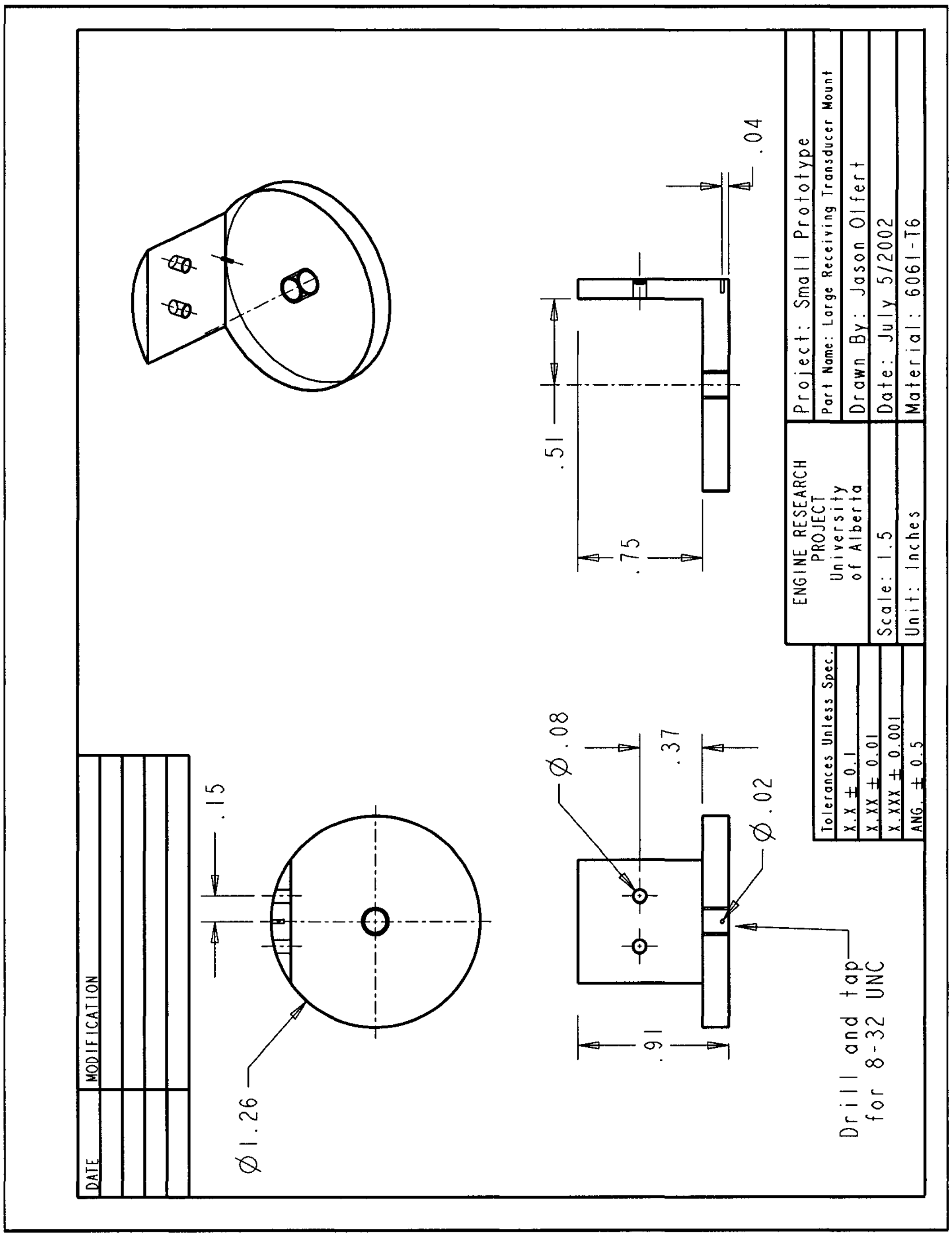

Figure C.5: Drawing of Large Receiving Transducer Mount of Small Prototype

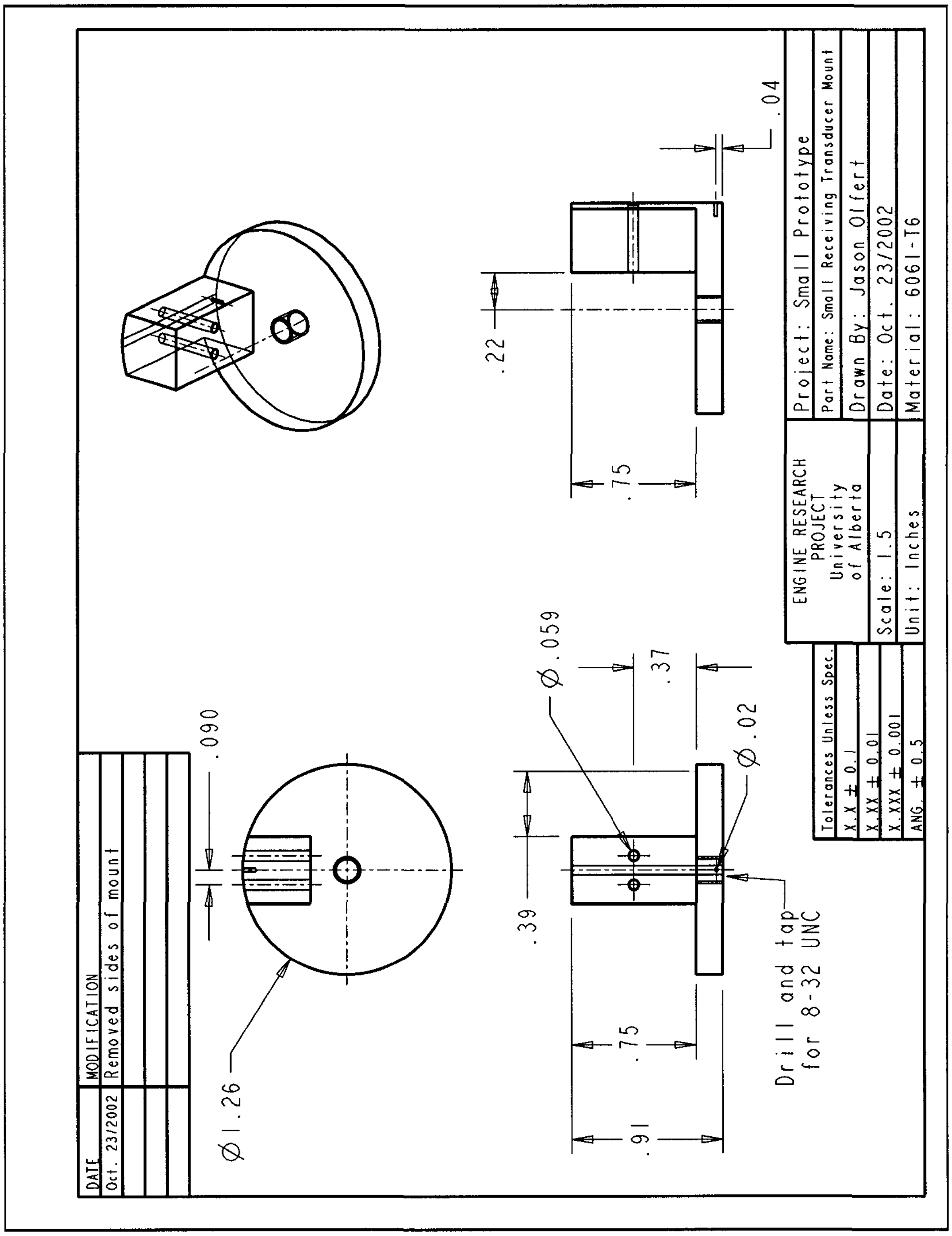

Figure C.6: Drawing of Small Receiving Transducer Mount of Small Prototype

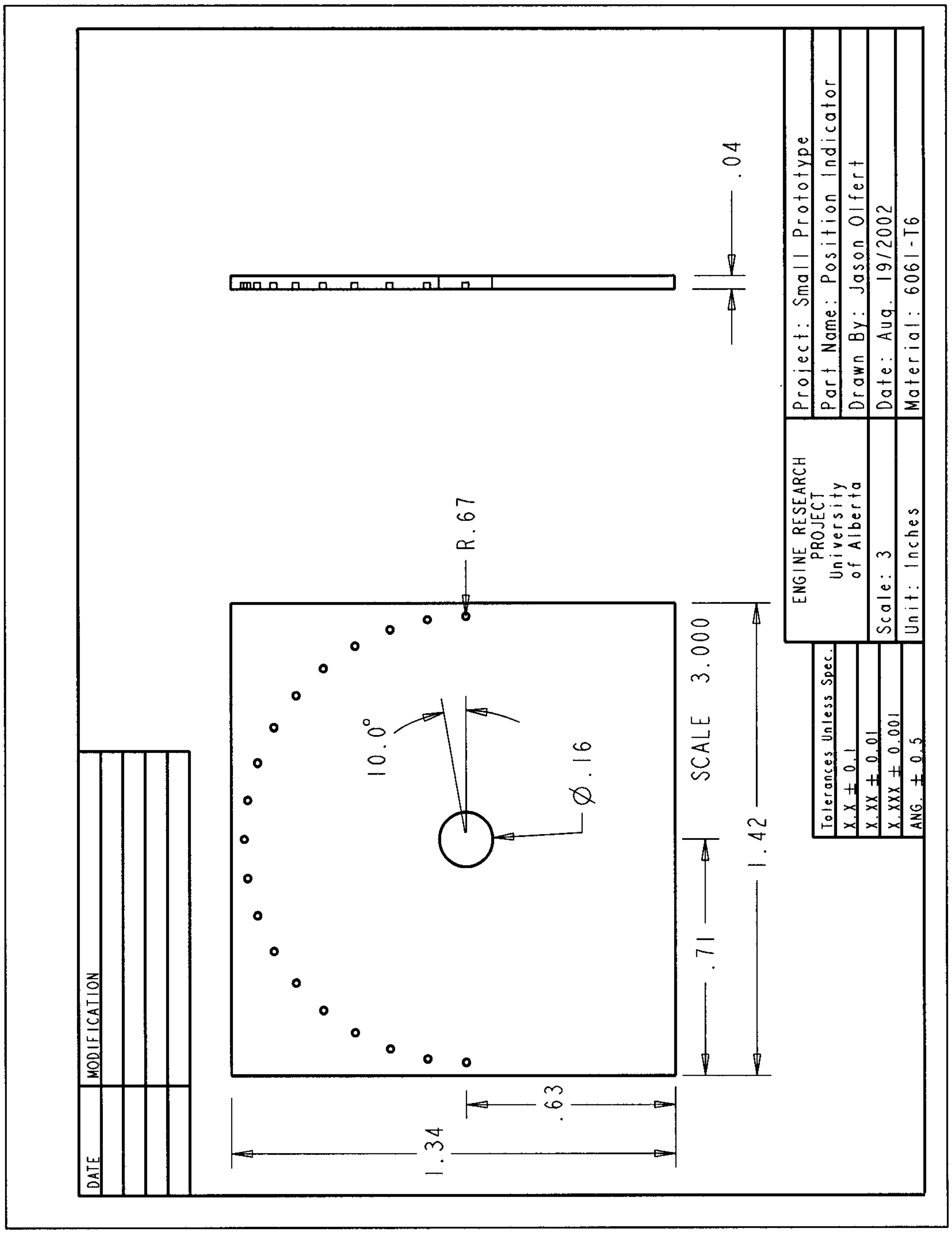

Figure C.7: Drawing of Position Indicator of Small Prototype

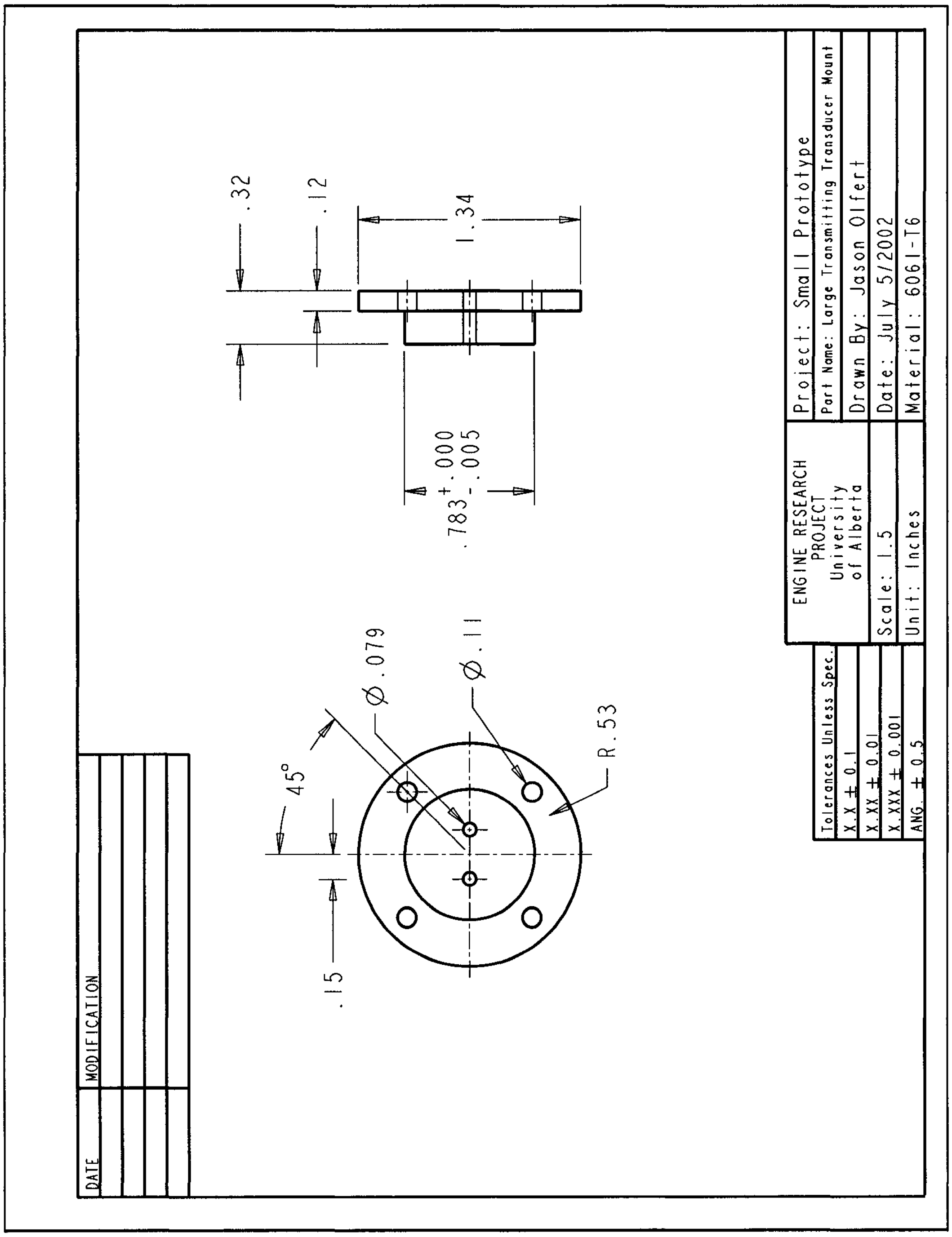

Figure C.8: Drawing of Large Transmitting Transducer Mount of Small Prototype

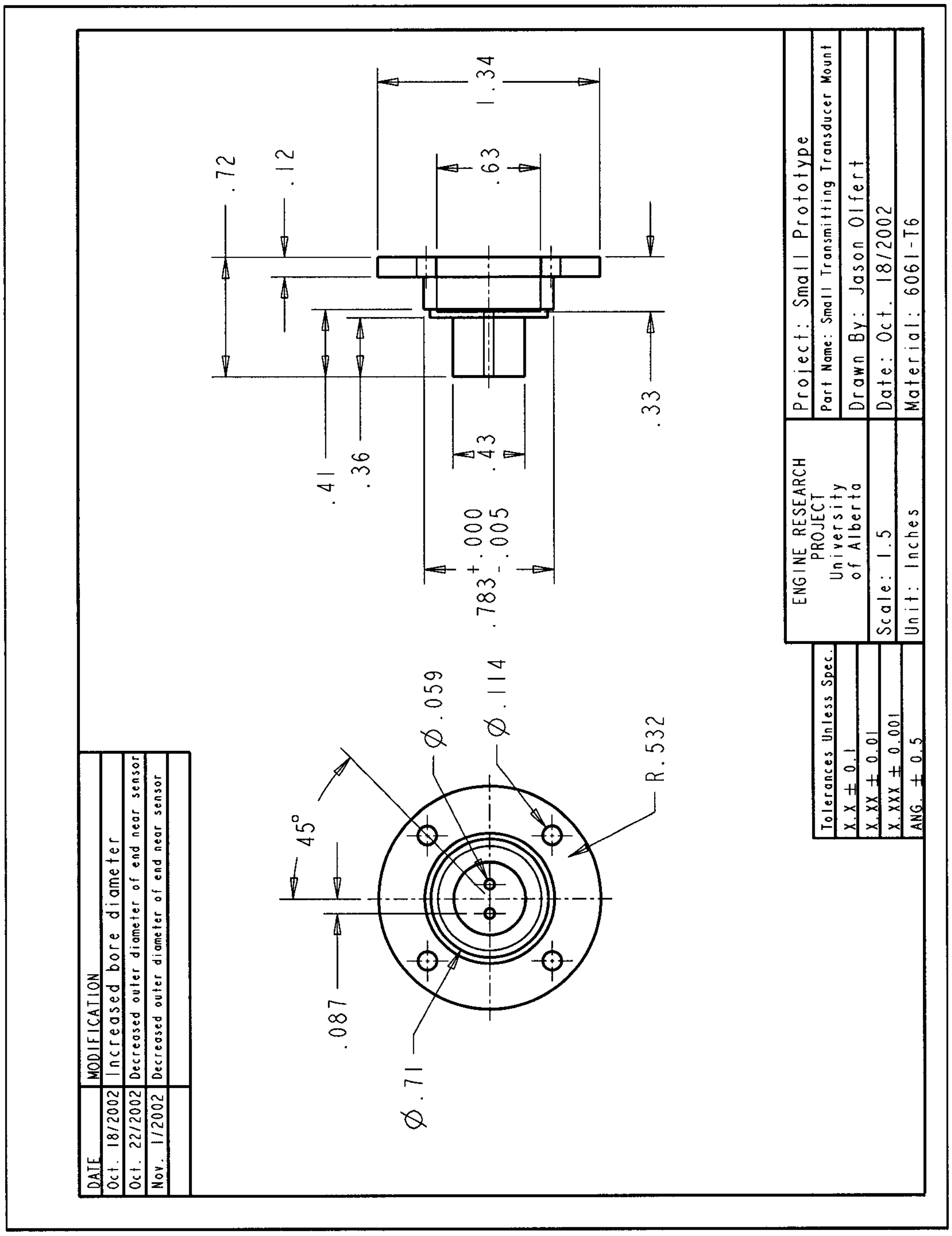

Figure C.9: Drawing of Small Transmitting Transducer Mount of Small Prototype

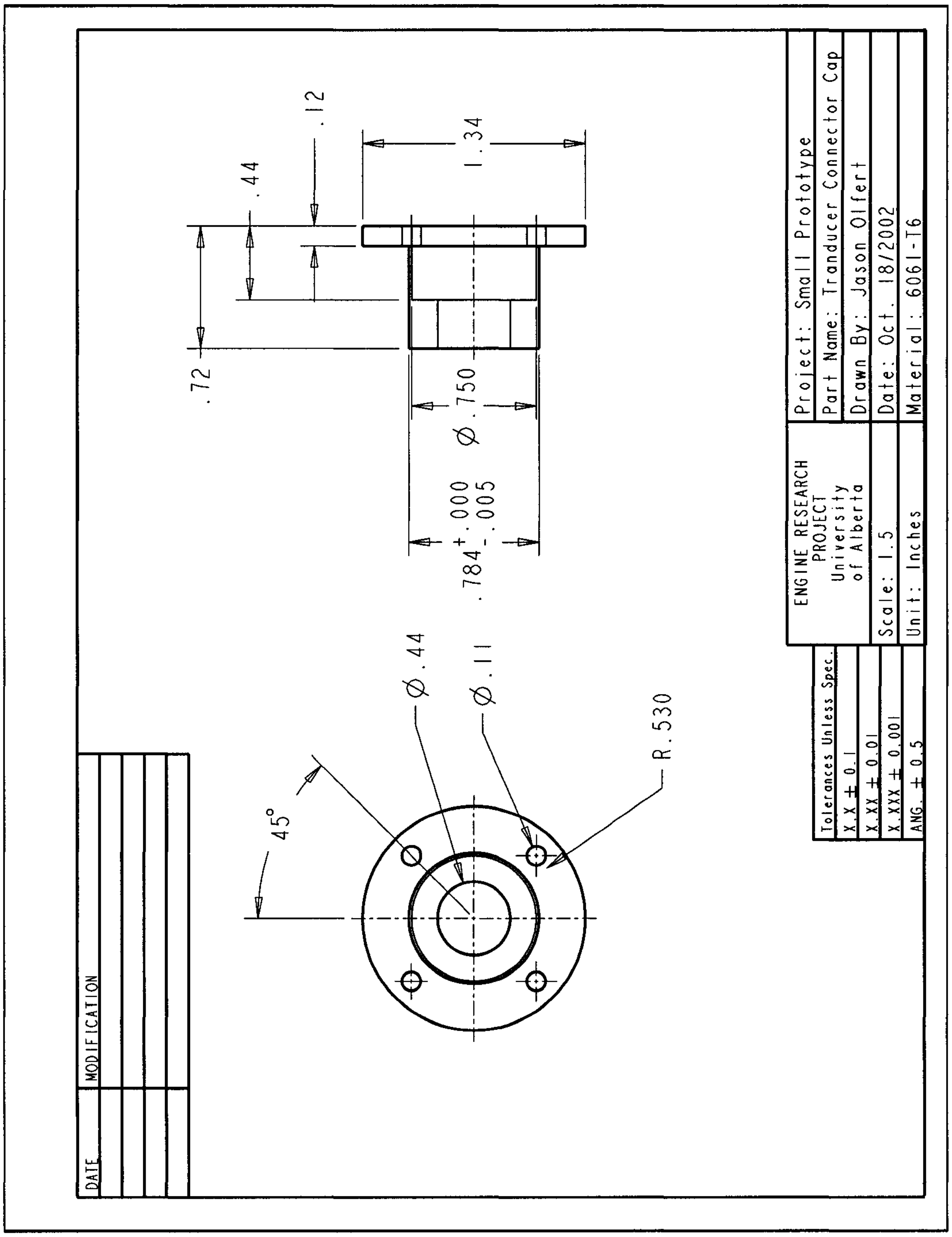

Figure C.10: Drawing of Transducer Connector Cap of Small Prototype

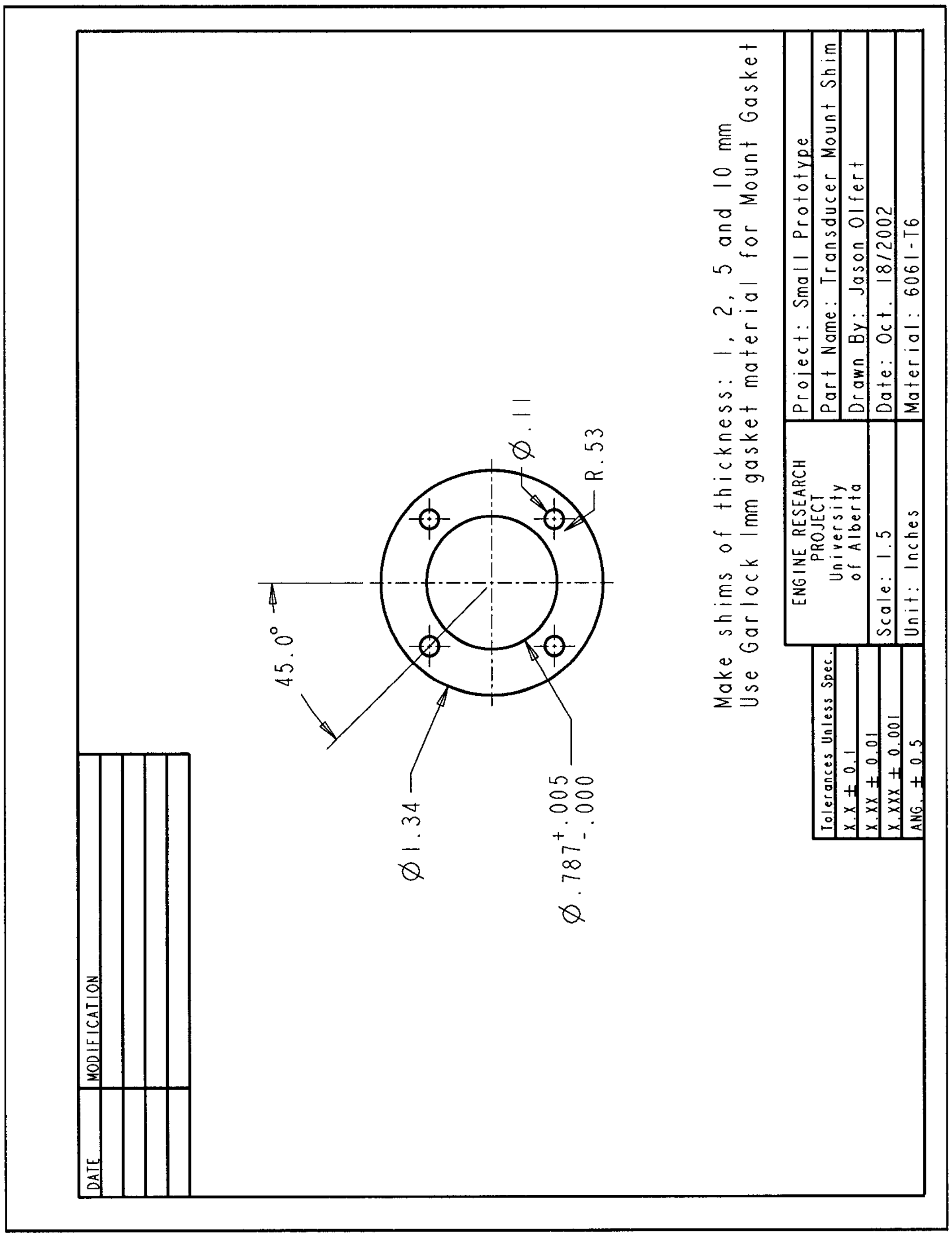

Make shims of thickness: 1, 2, 5 and 10 mm
Use Garlock 1mm gasket material for Mount Gasket

ENGINE RESEARCH PROJECT
University of Alberta

Project: Small Prototype
Part Name: Transducer Mount Shim
Drawn By: Jason Olfert
Scale: 1.5
Date: Oct. 18/2002
Unit: Inches
Material: 6061-T6

Tolerances Unless Spec.
X.X ± 0.1
X.XX ± 0.01
X.XXX ± 0.001
ANG. ± 0.5

Figure C.11: Drawing of Transducer Mount Shim of Small Prototype

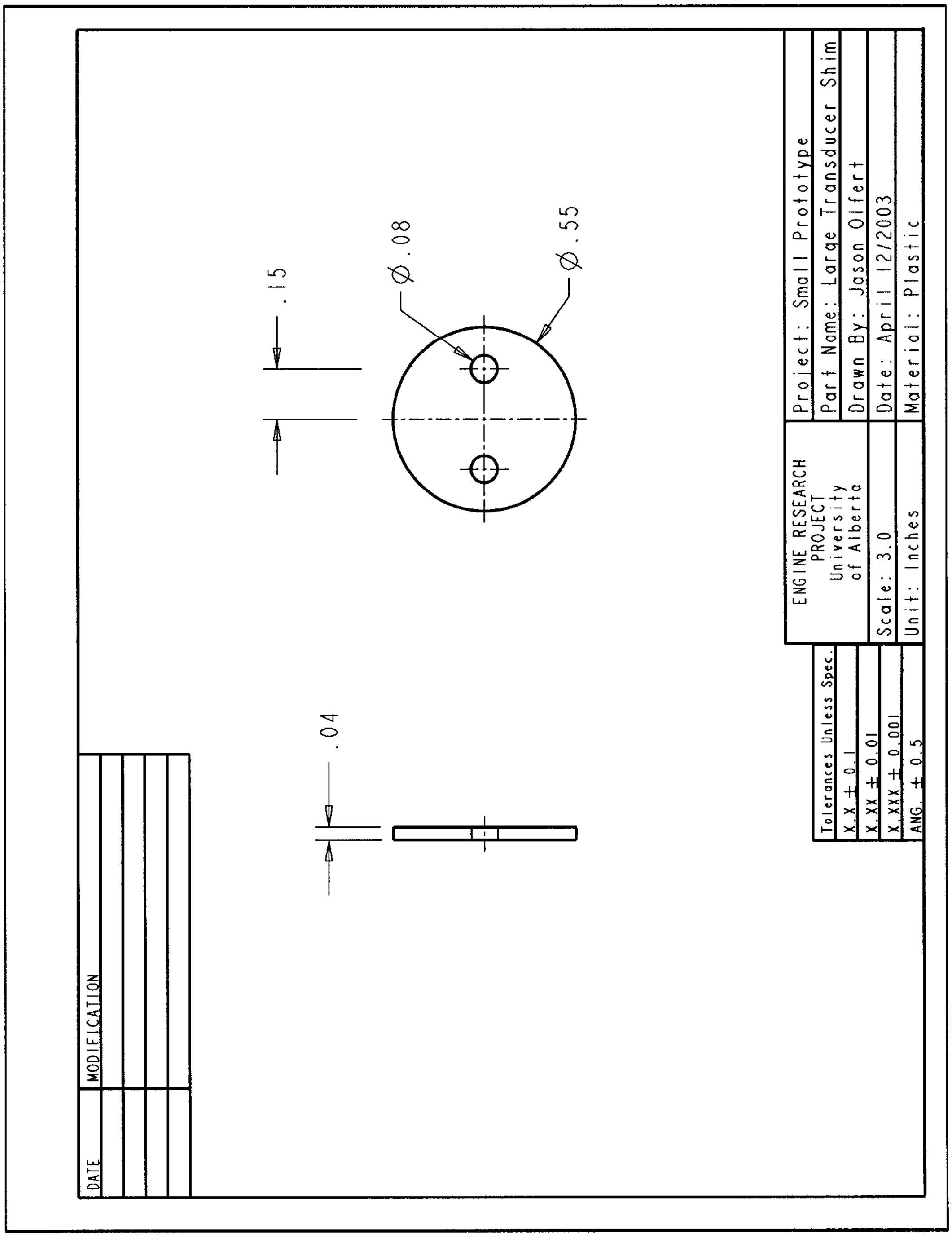

Figure C.12: Drawing of Large Transducer Shim of Small Prototype

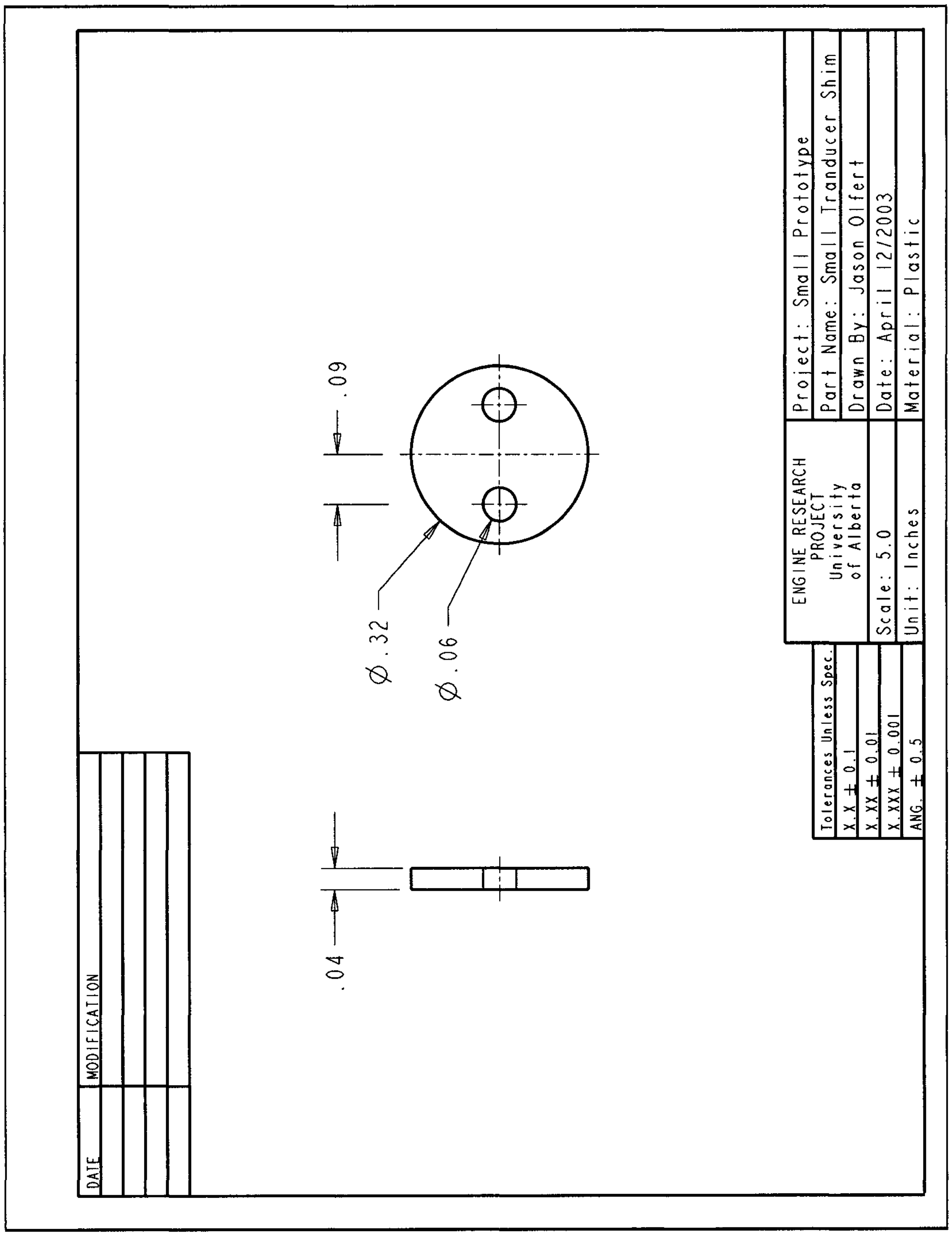

ENGINE RESEARCH PROJECT
University of Alberta

Project: Small Prototype
Part Name: Small Tranducer Shim
Drawn By: Jason Olfert
Date: April 12/2003
Material: Plastic
Scale: 5.0
Unit: Inches

Tolerances Unless Spec.
X.X ± 0.1
X.XX ± 0.01
X.XXX ± 0.001
ANG. ± 0.5

Figure C.13: Drawing of Small Transducer Shim of Small Prototype

APPENDIX D

LARGE PROTOTYPE CONSTRUCTION AND DRAWINGS

The drawings of the large prototype components are found in this appendix. Figure D.1 shows the assembly of the large prototype. The assembly shows the large transducers in the assembly although the small transducers can be interchanged with this prototype.

The main body of the large prototype is made from a commercially available aluminum enclosure (Hammond® # 1411R). Holes were punched into the enclosure for the transducer mounts and the Swagelok® bulkhead fittings (see Figs. D.2 and D.3).

Construction of this prototype is very similar to the small prototype. The transducers and mounts can be constructed in the same way as explained in App. C. Also, Kaowool® board insulation (M Board), 10 mm thick, was attached to all interior sides of the large prototype with adhesive tape.

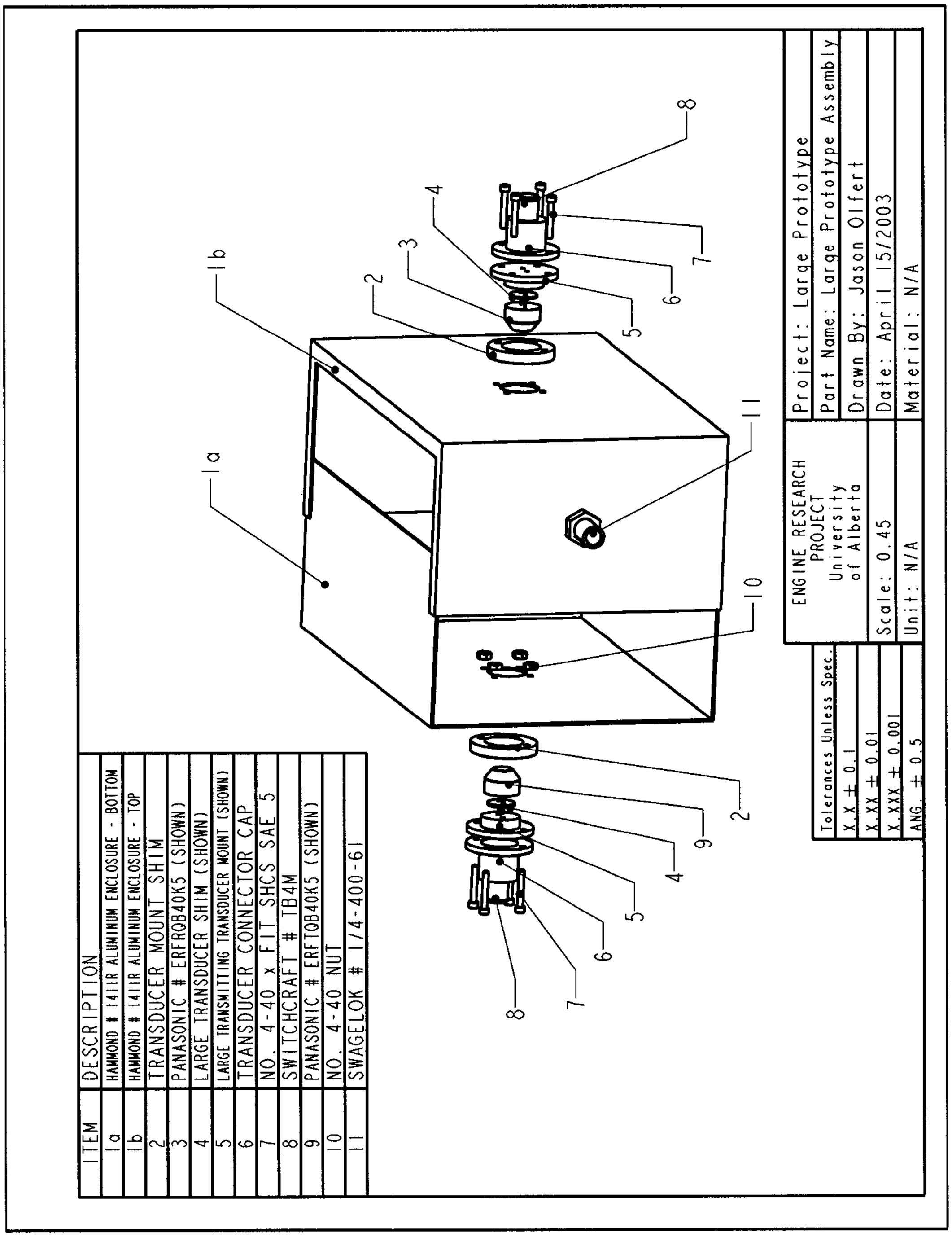

ITEM	DESCRIPTION
1a	HAMMOND # 1411R ALUMINUM ENCLOSURE - BOTTOM
1b	HAMMOND # 1411R ALUMINUM ENCLOSURE - TOP
2	TRANSDUCER MOUNT SHIM
3	PANASONIC # ERFRQB40K5 (SHOWN)
4	LARGE TRANSDUCER SHIM (SHOWN)
5	LARGE TRANSMITTING TRANSDUCER MOUNT (SHOWN)
6	TRANSDUCER CONNECTOR CAP
7	NO. 4-40 x FIT SHCS SAE 5
8	SWITCHCRAFT # TB4M
9	PANASONIC # ERFTQB40K5 (SHOWN)
10	NO. 4-40 NUT
11	SWAGELOK # 1/4-400-61

Tolerances Unless Spec.
X.X ± 0.1
X.XX ± 0.01
X.XXX ± 0.001
ANG. ± 0.5

ENGINE RESEARCH
PROJECT
University
of Alberta
Scale: 0.45
Unit: N/A

Project: Large Prototype
Part Name: Large Prototype Assembly
Drawn By: Jason Olfert
Date: April 15/2003
Material: N/A

Figure D.1: Drawing of Large Prototype Assembly

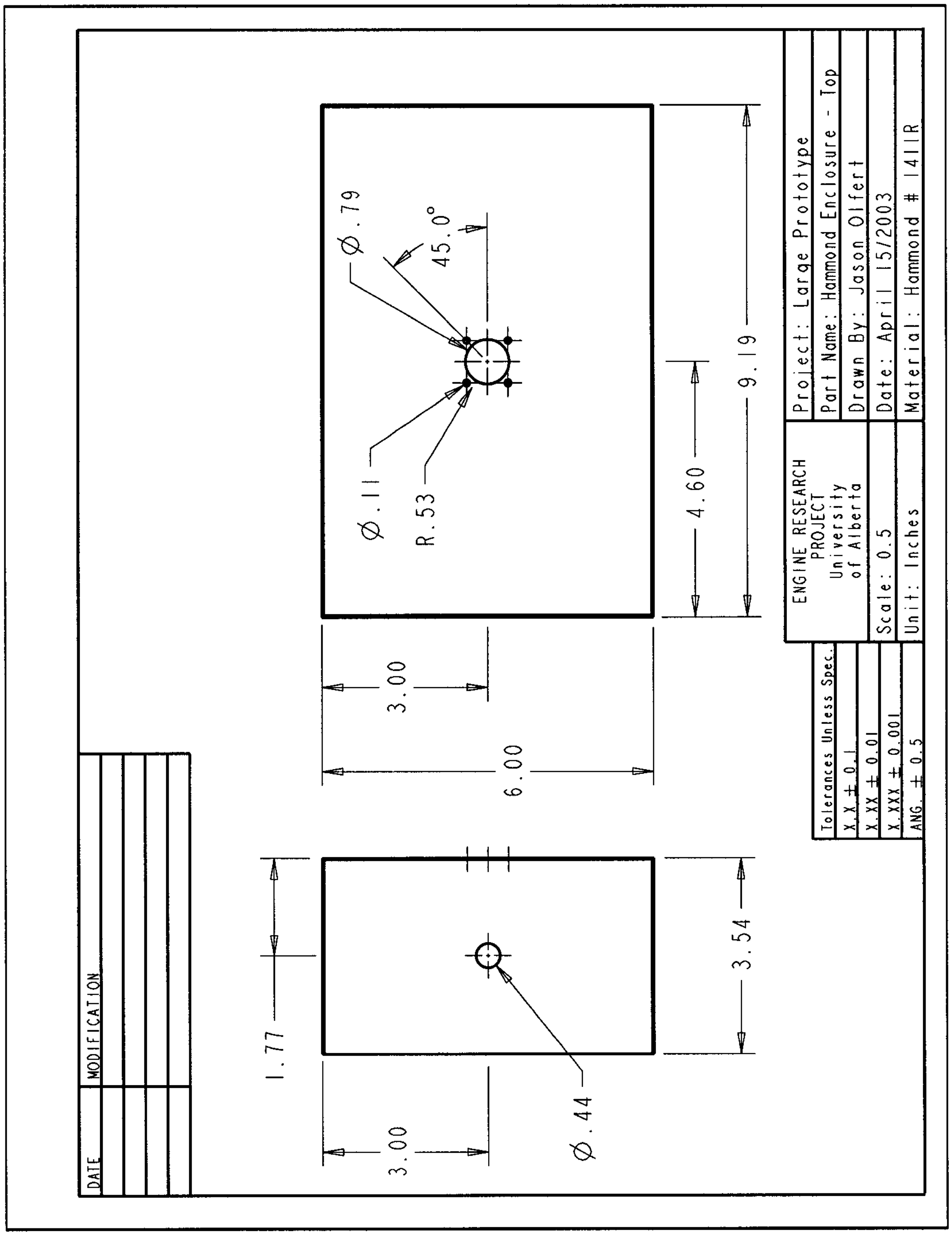

Figure D.2: Drawing of Top Hammond Enclosure

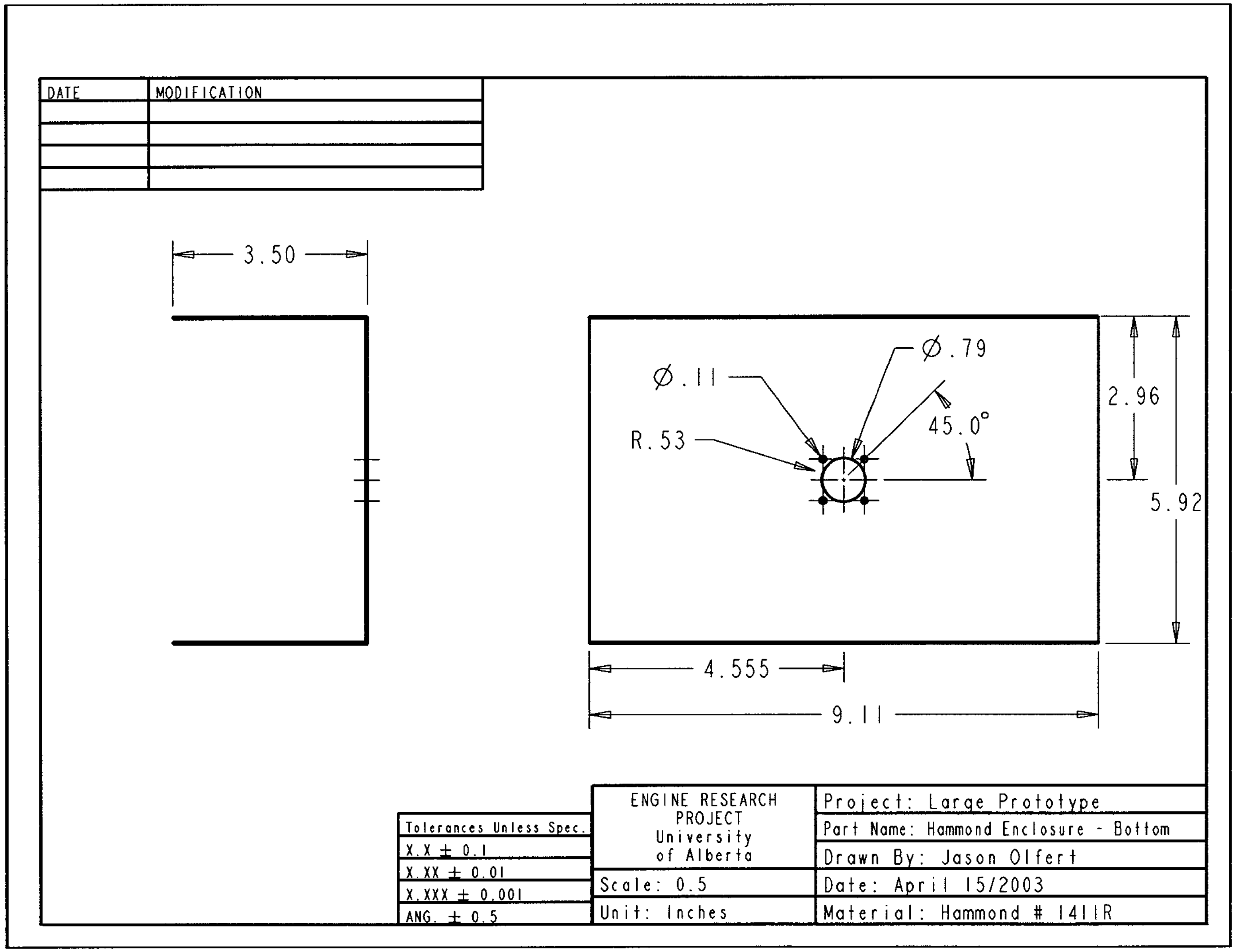

Figure D.3: Drawing of Bottom Hammond Enclosure

APPENDIX E

CALCULATING LEAN FLAMMABILITY LIMITS OF NATURAL GAS WITH LE CHATELIER'S RULE

E.1 Introduction

Calculating lean flammability limits (LFLs) of natural gas can be slightly more complicated than calculating LFLs of a simple mixture of flammable gases. Traditionally, the LFL of a flammable mixture, LFL_{mix}, can be calculated from Le Chatelier's Rule[1-3] as follows:

$$LFL_{mix} = \frac{100}{\sum_i \frac{p_i}{LFL_i}} \tag{E.1}$$

where p_i is the percentage of the gas component (by volume) and LFL_i is the LFL of the gas component.

However, Eq. E.1 cannot directly be used for a mixture containing inert gases and air. A procedure has been developed to calculate the LFL for mixtures containing flammable gases, inert gases and air[2].

This appendix will show a sample calculation of the LFL of a natural gas mixture containing methane, heavier hydrocarbons, inert gases and air as shown in Table E.1.

The LFLs for this kind of mixture can be found by: i) calculating the composition of the mixture on an air-free basis, ii) grouping mixtures for each inert gas; with each

Table E.1: Sample Natural Gas Composition Including LFLs of Gas Components

Component	Percent Composition	Air-Free Composition	LFL[a]
Methane	83.94%	90.36%	5.0%
Ethane	5.62%	6.05%	3.0%
Propane	0.99%	1.07%	2.1%
C_4 and higher[b]	0.31%	0.33%	1.8%
Nitrogen	6.28%	0.71%	-
Carbon Dioxide	1.37%	1.47%	-
Oxygen	1.49%	0%	-

Source: S. Schaedel, 1996[4]

[a] Lean flammability limits from Glassman, 1987[5]

[b] Assumed to be *n*-butane for calculation purposes

mixture of one flammable gas with one inert gas, iii) find the LFL of each of these mixtures from experimental data, iv) find the LFL of the air-free mixture by using Le Chatelier's Rule on the grouped mixtures and the remaining flammable gases and v) adjust the air-free LFL to the original mixture's LFL.

E.2 Composition of Air-Free Mixture

The natural gas composition can be adjusted to an air-free mixture by finding the percentage of air in the mixture. The percentage of air can be found from:

$$p_{air} = p_{O_2} \times 4.77 \frac{\%\ \text{air}}{\%\ O_2} \tag{E.2}$$

for the sample gas,

$$p_{air} = 1.49\% \times 4.77 = 7.10\%$$

Therefore, the remaining components, besides the nitrogen, can be found by adjusting to the air-free mixture by Eq. E.3:

$$p_{i,i \neq N_2} = p_i \times \frac{100}{p_{air}} \tag{E.3}$$

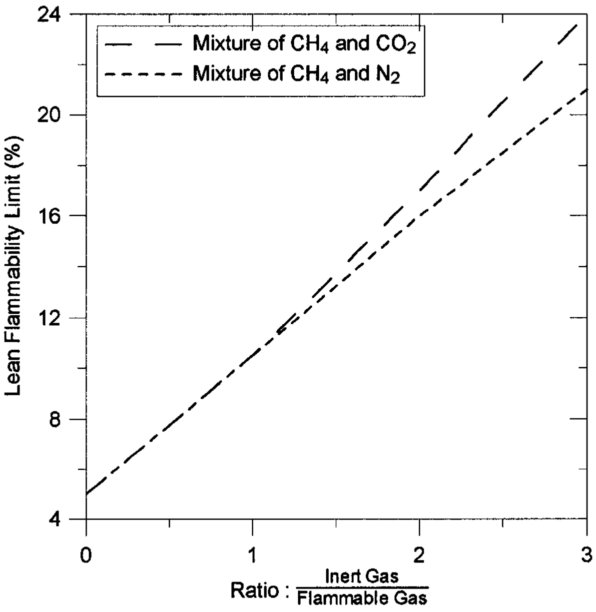

Source: G.W. Jones, *Inflammability of mixed gases*. US Gov. Print. Off., 1929.

Figure E.1: Lean Flammability Limits of Mixtures of Methane, Carbon Dioxide and Nitrogen

And the percentage of nitrogen will be the balance of the mixture:

$$p_{N_2} = 100 - \sum_i p_i \tag{E.4}$$

Therefore, the air-free composition of the natural gas can be calculated and is shown in Table E.1.

E.3 Group Mixtures of Inert and Flammable Gases

The inert gases can be grouped with flammable gases for which experimental data exists for the LFL of the grouped mixture. Experimental data exists for the LFLs of mixtures of methane and nitrogen and methane and carbon dioxide as seen in Fig. E.1.

The division of the methane and inert gases is somewhat arbitrary but the mix-

Table E.2: Grouping of Flammable and Inert Gases

Component or Mixture	Flammable Percent	Inert Percent	Total Percent	Ratio of: $\frac{\text{Inert}}{\text{Flammable}}$	LFL
Methane/N_2	0.36%	0.71%	1.07%	2	16%
Methane/CO_2	0.74%	1.47%	2.21%	2	17%
Methane	89.27%	-	89.27%	-	5.0%
Ethane	6.05%	-	6.05%	-	3.0%
Propane	1.07%	-	1.07%	-	2.2%
C_4 and higher[a]	0.33%	-	0.33%	-	1.9%

[a] Assumed to be *n*-butane for calculation purposes

tures will be chosen so that the ratio of the gases lie within the limits of Fig. E.1 (ie. a ratio between 0 and 3). Table E.2 shows the groupings of methane and inert gases as well as the balance of flammable gases in the sample natural gas.

E.4 Find LFL of Each Mixture and Component

The LFL for each mixture of inert and flammable gas can be found from Fig. E.1. For example, the LFL of the mixture of methane and nitrogen can be found by calculating the ratio:

$$\text{Ratio} = \frac{\%\ \text{Inert Gas}}{\%\ \text{Flammable Gas}} = \frac{0.71\%}{0.36\%} = 2 \qquad \text{(E.5)}$$

Figure E.1 shows that for a mixture of methane and nitrogen with a ratio of 2, the LFL will be 16%. The same procedure is used for finding the LFL of the methane and carbon dioxide mixture and the results are shown in Table E.2.

The LFL of the pure flammable gas components are also found experimentally and can be found in combustion books such as Glassman's[5]. The LFL for each pure flammable gas is shown in Table E.2.

E.5 Find LFL of Air-Free Mixture by Le Chatelier's Rule

The LFL of the air-free mixture can be found by simply applying Le Chatelier's rule to the components of the air-free mixture shown in Table E.2:

$$\begin{aligned} LFL_{\text{air-free mix}} &= \frac{100}{\sum_i \frac{p_i}{LFL_i}} \\ &= \frac{100}{\frac{1.07}{16} + \frac{2.21}{17} + \frac{89.37}{5.0} + \frac{6.05}{3.0} + \frac{1.07}{2.2} + \frac{0.33}{1.9}} \\ LFL_{\text{air-free mix}} &= 4.8\% \end{aligned} \tag{E.6}$$

Therefore the LFL of the air-free mixture is 4.8%.

E.6 Find LFL of Total Natural Gas Mixture

The LFL of the air-free mixture must be corrected for the amount of air originally in the mixture. Hence, the LFL of the natural gas mixture, LFL_{NG}, can be found from:

$$\begin{aligned} LFL_{NG} &= LFL_{\text{air-free mix}} \times \frac{100}{100 - p_{air}} \\ &= 4.8\% \times \frac{100}{100 - 7.1} \\ LFL_{NG} &= 5.2\% \end{aligned} \tag{E.7}$$

Therefore, the LFL of the natural gas mixture is 5.2%.

REFERENCES

[1] G. W. Jones, *Inflammability of Mixed Gases.* U.S. Govt. Print. Off., 1929.

[2] H. F. Coward and G. W. Jones, "Limits of flammability of gases and vapors," Tech. Rep. Bulletin 503, U.S. Bureau of Mines, 1952.

[3] M. G. Zabetakis, "Flammability characteristics of combustible gases and vapors," Tech. Rep. Bulletin 627, U.S. Bureau of Mines, 1965.

[4] S. Schaedel, M. Czachorski, P. Rowley, M. Richards, and Y. Shikari, "Gas composition issues and implications for natural gas vehicles and fueling stations," Tech. Rep. GRI-96/0028, Gas Research Institute, 1996.

[5] I. Glassman, *Combustion.* Academic Press, Inc, 1987.

APPENDIX F

STATIC CHARACTERISTICS OF PROTOTYPE SENSORS

Sensor static characteristics of interest are accuracy, calibration error, repeatability error, resolution error and range. This appendix calculates the static characteristics of the prototype natural gas quality (NGQ) sensor, variable gaseous fuel concentration (VGFC) sensor and exhaust gas recirculation (EGR) sensor. Five tests were taken on the NGQ and VGFC sensor and one one test on the EGR sensor. The raw data for each sensor tested is shown in Table F.1, F.4 and F.7. For each sensor the accuracy, calibration error, repeatability error, resolution error and range is found.

F.1 Static Characteristics of Natural Gas Quality Sensor

The following static characteristics are found for the natural gas quality sensor: calibration error, repeatability, resolution, accuracy and range. The experimental data for the NGQ sensor is see in Table F.1.

NGQ Sensor Calibration Error

The calibration error is the deviation of the calibration data to the calibration curve. The calibration curve and calibration data is shown in Fig. F.1. The calibration curve is found by plotting the sound speed, c, by the average voltage reading. A second order polynomial is used to 'best-fit' the calibration data. Therefore, the calibration

Table F.1: Experimental Data for Natural Gas Quality Sensor

Sound	Voltage (V)					
Speed (m/s)	Test 1	Test 2	Test 3	Test 4	Test 5	Average
350.5	7.96	8.01	7.96	7.96	7.96	7.97
354.4	7.51	7.58	7.54	7.53	7.55	7.54
359.1	7.06	7.12	7.11	7.08	7.12	7.10
364.7	6.58	6.65	6.64	6.61	6.66	6.63
371.3	6.06	6.14	6.14	6.14	6.15	6.13
379.0	5.47	5.50	5.52	5.51	5.50	5.50
388.2	4.72	4.73	4.76	4.75	4.73	4.74
399.0	3.99	4.01	4.05	4.04	4.04	4.03
411.9	3.16	3.17	3.23	3.19	3.20	3.19
427.4	2.20	2.20	2.22	2.23	2.24	2.22
446.3	1.34	1.34	1.35	1.34	1.35	1.34

curve for this prototype sensor is:

$$V = 2.539 \times 10^{-4}c^2 - 0.2711c + 71.74 \tag{F.1}$$

A conservative estimate of the calibration error, δ_{cal}, will be the maximum error of the measurement reading from the calibration curve. Where the error at each reading, δ_{cal_i}, can be calculated by:

$$\delta_{cal_i} = \left| \frac{V_{meas_i} - V_{cal_i}}{\frac{dV}{dc}\big|_{c_i}} \right| \tag{F.2}$$

where V_{meas} is the voltage measurement (in this case the average voltage of the 5 tests will be used), V_{cal} is the voltage calculated from the calibration curve and $\frac{dV}{dc}(c_i)$ is the slope calculated at the reading of interest. For this calibration curve:

$$\frac{dV}{dc} = 5.078 \times 10^{-4}c - 0.2711 \tag{F.3}$$

Table F.2 shows the calibration error calculation. The maximum δ_{cal_i} is used as the calibration error, which is a conservative calculation of the error. The calculation

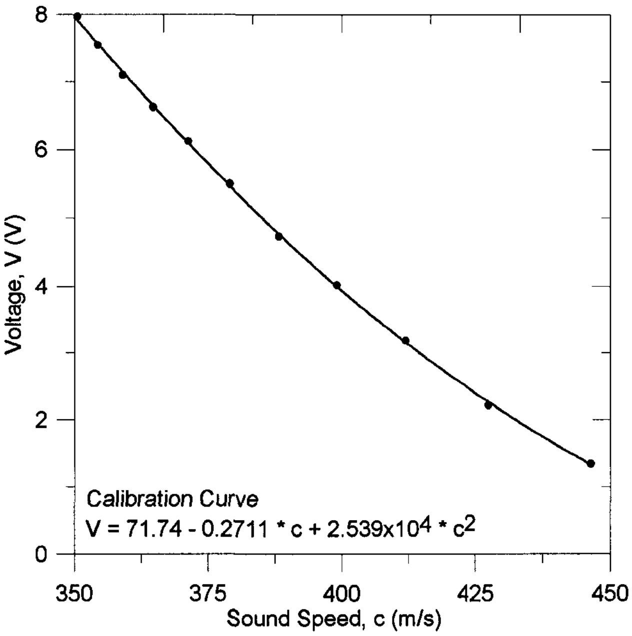

Figure F.1: Calibration Curve of Prototype Natural Gas Quality Sensor

shows that the calibration error is ±1.18 m/s.

NGQ Sensor Repeatability Error

Repeatability error is the error caused by a sensor which does not produce the same results under the same conditions. The repeatability error, δ_r, will be the maximum difference between two readings. Where the repeatability error at each reading, δ_{r_i}, can be found from:

$$\delta_{r_i} = \left| \frac{\max(V_{meas})_i - \min(V_{meas})_i}{\frac{dV}{dc}\big|_{c_i}} \right| \tag{F.4}$$

where $\max(V_{meas})_i$ and $\min(V_{meas})_i$ is the maximum and minimum voltage reading for all the experimental tests.

Table F.3 shows the repeatability error calculation. Again, the maximum δ_{r_i} was used for the repeatability error calculation, so that a conservative estimate could be found. The calculation shows that the repeatability error is ±1.13 m/s.

Table F.2: Calibration Error Calculation for NGQ Sensor

c (m/s)	V_{meas} (V)	V_{cal} (V)	$\lvert V_{meas} - V_{cal}\rvert$ (V)	$\lvert \frac{dV}{dc}\rvert_c \rvert$ (Vs/m)	δ_{cal_i} (m/s)
350.5	7.97	7.92	0.04	0.093	0.43
354.4	7.54	7.57	0.06	0.091	0.61
359.1	7.10	7.14	0.08	0.089	0.93
364.7	6.63	6.65	0.07	0.086	0.86
371.3	6.13	6.10	0.04	0.083	0.45
379.0	5.50	5.47	0.00	0.079	0.00
388.2	4.74	4.77	0.05	0.074	0.71
399.0	4.03	4.00	0.01	0.068	0.18
411.9	3.19	3.16	0.00	0.062	0.05
427.4	2.22	2.26	0.06	0.054	1.18
446.3	1.34	1.33	0.01	0.044	0.24
				δ_{cal}	± 1.18

Table F.3: Repeatability Error Calculation for NGQ Sensor

c (m/s)	max(V_{meas}) (V)	min(V_{meas}) (V)	$\lvert \max(V_{meas}) - \min(V_{meas})\rvert$ (V)	$\lvert \frac{dV}{dc}\rvert_c \rvert$ (Vs/m)	δ_{r_i} (m/s)
350.5	8.01	7.96	0.05	0.093	0.54
354.4	7.58	7.51	0.07	0.091	0.77
359.1	7.12	7.06	0.06	0.089	0.68
364.7	6.66	6.68	0.08	0.086	0.93
371.3	6.15	6.06	0.09	0.083	1.09
379.0	5.52	5.47	0.05	0.079	0.64
388.2	4.76	4.72	0.04	0.074	0.54
399.0	4.05	3.99	0.06	0.068	0.88
411.9	3.23	3.16	0.07	0.062	1.13
427.4	2.24	2.20	0.04	0.054	0.74
446.3	1.35	1.34	0.01	0.044	0.23
				δ_r	± 1.13

NGQ Sensor Resolution Error

Resolution is the smallest increment of input to produce a output change. For the NGQ sensor the sensor would produce a stable reading of 0.01 V. Therefore the resolution error, δ_{res}, can be found from:

$$\begin{aligned}\delta_{res} &= \frac{\text{Output Resolution}}{\min(|\frac{dV}{dc}|_{c_i}|)} \\ &= \frac{0.01 \text{ V}}{0.044 \text{ Vs/m}} \\ \delta_{res} &= \pm 0.22 \text{ m/s}\end{aligned} \tag{F.5}$$

The minimum slope is used so that a conservative estimate of the resolution error is found. Therefore, the resolution error is ± 0.22 m/s.

NGQ Sensor Accuracy

The total error (δ_{total}), or accuracy, will be the 'root-sum-square' of the calibration error, repeatability error and resolution error. Therefore, the accuracy of the NGQ sensor will be:

$$\begin{aligned}\delta_{total} &= \sqrt{\delta_{cal}^2 + \delta_r^2 + \delta_{res}^2} \\ &= \sqrt{(1.18)^2 + (1.13)^2 + (0.22)^2} \\ \delta_{total} &= \pm 1.65 \text{ m/s}\end{aligned} \tag{F.6}$$

Therefore, the total error is ±1.65 m/s. Recall, that the maximum errors of calibration, repeatability and resolution was used in each case. Therefore, this accuracy estimation is very conservative.

NGQ Sensor Range

The range of the NGQ sensor and the DAWPD method in general, is proportional to the design parameters such as path length, driving frequency, phase range of phase comparator and sound speed of the reference gas. Therefore, the range of the prototype can be found by finding the highest and lowest sound speed that can be measured without exceeding the range of the phase comparator.

The range of the phase comparator in the prototype sensor was 0 to π radians. The prototype's 'time delay' circuitry was adjusted so that the highest sound speed measured (pure methane at 23.9 °C or 446.3 m/s) related to a phase difference of 0 radians. This is the reference sound speed, c_{ref}. Therefore, the lowest sound speed that can be measured with this configuration is:

$$c_{low} = \frac{1}{\frac{\theta}{2\pi f d^*} + \frac{1}{c_{ref}}} \tag{F.7}$$

where f is the driving frequency of the ultrasonic transducers, θ is the phase range of the phase comparator in radians and d^* is the theoretical path length found from (see Sec. 3.6.1):

$$d^* = \left| \frac{\Phi_1 - \Phi_n}{\frac{1}{c_1} - \frac{1}{c_n}} \right| \tag{F.8}$$

where Φ_1 and Φ_n are the experimental time difference measurements spanning the range of measurements. c_1 and c_n can be determined from Eq. 3.3 since a binary gas mixture (nitrogen and methane) was used to create the range of sound speeds.

For the NGQ sensor Φ_1 and Φ_n were found to be 0 and 6.8 μs, respectively. Therefore, the theoretical path length and range can be calculated:

$$\begin{aligned} d^* &= \left| \frac{0\text{ s} - 6.8 \times 10^{-6}\text{ s}}{\frac{1}{350.5\text{ m/s}} - \frac{1}{446.3\text{ m/s}}} \right| \\ d^* &= 0.0111\text{ m or } 11.1\text{ mm} \end{aligned}$$

Table F.4: Experimental Data for Variable Gaseous Fuel Concentration Sensor

H_2 Concentration	Voltage (V)					
(% Volume)	Test 1	Test 2	Test 3	Test 4	Test 5	Average
0.0	11.77	11.79	11.80	11.75	11.79	11.78
13.6	10.36	10.35	10.37	10.14	10.45	10.33
26.1	9.54	9.53	9.59	9.15	9.71	9.50
37.8	8.14	8.16	8.20	7.55	8.31	8.07
48.6	6.06	5.98	6.02	5.48	6.06	5.92
58.6	4.22	4.16	4.22	3.91	4.24	4.15
68.0	2.54	2.55	2.57	2.42	2.31	2.48
76.8	0.14	0.14	0.03	0.04	0.01	0.07

Therefore, the lowest sound speed that can be measured is:

$$\begin{aligned} c_{low} &= \frac{1}{\frac{\pi}{2\pi(40{,}000\mathrm{Hz})(0.0111\mathrm{m})} + \frac{1}{446.3\mathrm{m/s}}} \\ c_{low} &= 297.0\mathrm{m/s} \end{aligned}$$

Therefore the range of the prototype sensor tested is 297.0 to 446.3 m/s. The range can be adjusted with the time delay circuitry in the sensor circuitry (see Sec. 2.6.1).

F.2 Static Characteristics of Variable Gaseous Fuel Concentration Sensor

A similar error analysis can be preformed on the experimental data for the prototype VGFC sensor. The following static characteristics are found for the VGFC sensor: calibration error, repeatability, resolution, accuracy and range. The experimental data for the VGFC sensor is seen in Table F.4.

VGFC Sensor Calibration Error

The calibration curve and calibration data for the VGFC sensor are shown in Fig. F.2. The calibration curve is found by plotting the concentration of hydrogen, y_{H_2}, by the average voltage reading. A second order polynomial is used to 'best-fit' the calibration

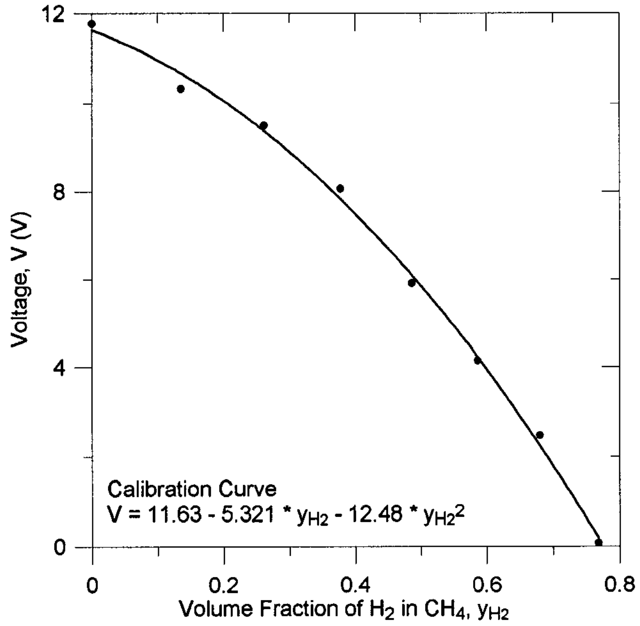

Figure F.2: Calibration Curve of Prototype Variable Gaseous Fuel Concentration Sensor

data. Therefore, the calibration curve for this prototype sensor is:

$$V = -12.48 y_{H_2}^2 - 5.321 y_{H_2} + 11.63 \tag{F.9}$$

and the slope for the calibration curve is:

$$\frac{dV}{dy_{H_2}} = -24.96 y_{H_2} - 5.321 \tag{F.10}$$

Using Eq. F.2, the conservative calibration error can be found for the VGFC sensor. Table F.5 shows the results of the calculation, which resulted in a calibration error of ±0.0364 volume fraction of hydrogen in methane, or ±3.64%(vol.).

Table F.5: Calibration Error Calculation for Variable Gaseous Fuel Concentration Sensor

y_{H_2} (vol.)	V_{meas} (V)	V_{cal} (V)	$\lvert V_{meas} - V_{cal}\rvert$ (V)	$\lvert \frac{dV}{dy_{H_2}}\rvert_{y_{H_2}}\rvert$ (V/vol.)	δ_{cal_i} (vol.)
0.00	11.78	11.63	0.14	5.32	0.0261
0.136	10.33	10.68	0.32	8.71	0.0364
0.261	9.50	9.39	0.15	11.8	0.0129
0.378	8.07	7.84	0.30	14.7	0.0202
0.486	5.92	6.11	0.05	17.4	0.0026
0.586	4.15	4.23	0.01	19.9	0.0003
0.680	2.48	2.25	0.29	22.3	0.0132
0.768	0.07	0.19	0.05	24.5	0.0022
				δ_{cal}	± 0.0364

Table F.6: Repeatability Error Calculation for Variable Gaseous Fuel Concentration Sensor

y_{H_2} (vol.)	$\max(V_{meas})$ (V)	$\min(V_{meas})$ (V)	$\lvert \max(V_{m.}) - \min(V_{m.})\rvert$ (V)	$\lvert \frac{dV}{dy_{H_2}}\rvert_{y_{H_2}}\rvert$ (V/vol.)	δ_{r_i} (vol.)
0.00	11.80	11.75	0.05	5.32	0.0094
0.136	10.45	10.14	0.31	8.71	0.0356
0.261	9.71	9.15	0.56	11.8	0.0473
0.378	8.31	7.55	0.76	14.7	0.0515
0.486	6.06	5.48	0.58	17.4	0.0333
0.586	4.24	3.91	0.33	19.9	0.0165
0.680	2.57	2.31	0.26	22.3	0.0117
0.768	0.14	0.01	0.13	24.5	0.0053
				δ_r	± 0.0515

VGFC Sensor Repeatability Error

The repeatability error of the VGFC sensor can be found with a similar method as described above. Table F.6 shows the repeatability error calculation. The calculation shows that the calibration error is ±0.0515 volume fraction of hydrogen in methane, or ±5.15%(vol.).

VGFC Sensor Resolution Error

For the VGFC sensor the sensor would produce a stable reading of 0.01 V. Therefore the resolution error, δ_{res}, can be found from:

$$\begin{aligned}\delta_{res} &= \frac{\text{Output Resolution}}{\min(|\frac{dV}{dy_{H_2}}|_{y_{H_{2_i}}}|)} \\ &= \frac{0.01 \text{ V}}{24.5 \text{ V/vol.}} \\ \delta_{res} &= \pm 4 \times 10^{-4} \text{ vol.}\end{aligned}$$

The minimum slope is used so that a conservative estimate of the resolution error is found. Therefore, the resolution error is ±4 × 10^{-4}(vol.), or ±0.04%(vol.).

VGFC Sensor Accuracy

The accuracy of the VGFC sensor can be calculated using the 'root-sum-square' method described earlier:

$$\begin{aligned}\delta_{total} &= \sqrt{(0.0364)^2 + (0.0515)^2 + (0.0004)^2} \\ \delta_{total} &= \pm 0.0631 \text{ vol.}\end{aligned}$$

Therefore, the total error is ±0.0631 (vol.), or ±6.31%(vol.) of hydrogen in methane. Recall, that the maximum errors of calibration, repeatability and resolution was used in each case. Therefore, this accuracy estimation is very conservative.

VGFC Sensor Range

The range of the prototype is limited by the acoustic impedance of the transducers used. This limits the prototype to a range of 0 to 77.5%(vol.) of hydrogen in methane, or sound speeds from 444 to 809 m/s. With transducers better matched to the acoustic

Table F.7: Experimental Data for Exhaust Gas Recirculation Sensor

$CO2_{intake}$ (%)	$CO2_{exhaust}$ (%)	EGR (%)	Output Voltage (V)	Driving Frequency (kHz)
0.00	10.10	19.5	8.4	39.930
0.50	10.05	14.4	8.0	39.986
1.01	10.26	9.8	7.4	40.042
1.45	10.41	4.8	6.9	40.126
1.97	10.40	0.0	6.4	40.211

impedance of hydrogen and methane, the range of the transducer could be extended to cover the range of 0 to 100% hydrogen.

F.3 Static Characteristics of Exhaust Gas Recirculation Sensor

Similarly, an error analysis can be preformed on the experimental data for the prototype EGR sensor. The following static characteristics are found for the EGR sensor: calibration error, resolution, accuracy and range. The experimental data for the EGR sensor is seen in Table F.7. The repeatability error was not found for this prototype due to the length of time to complete each experiment and the repeatability can be assumed to be on the same order of magnitude as the other prototype sensors.

EGR Sensor Calibration Error

The calibration curve and calibration data for the EGR sensor are shown in Fig. F.3. The calibration curve is found by plotting the concentration of EGR, by the voltage reading. Theoretically, the experimental data should follow second order polynomial. However, the range of sound speeds is small enough that a linear line can be used. Therefore, the calibration curve for this prototype sensor is:

$$V = -10.49EGR + 8.439 \tag{F.11}$$

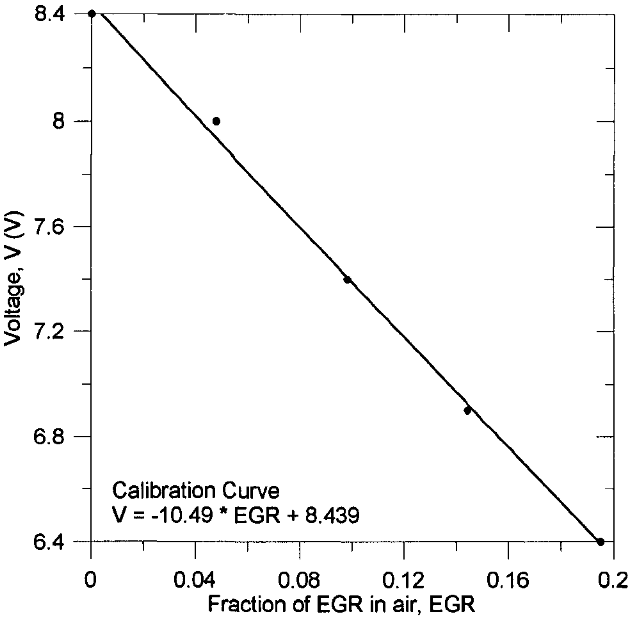

Figure F.3: Calibration Curve of Exhaust Gas Recirculation Sensor

Table F.8: Calibration Error Calculation for Exhaust Gas Recirculation Sensor

EGR (.vol)	V_{meas} (V)	V_{cal} (V)	$\lvert V_{meas} - V_{cal}\rvert$ (V)	$\lvert \frac{dV}{dEGR}\rvert_{EGR}\lvert$ (V/vol.)	δ_{cal_i} (vol.)
0.000	6.4	6.39	0.006	10.49	0.0006
0.048	6.9	6.93	0.026	10.49	0.0025
0.098	7.4	7.41	0.007	10.49	0.0006
0.144	8.0	7.94	0.065	10.49	0.0062
0.195	8.4	8.44	0.039	10.49	0.0037
				δ_{cal}	± 0.0062

Using Eq. F.2, the calibration error can be found for the EGR sensor. Table F.8 shows the results of the calculation, which resulted in a calibration error of ±0.0062 volume fraction of EGR, or ±0.62%(vol.).

EGR Sensor Repeatability Error

Multiple tests were not taken for the EGR sensor. However, the EGR sensor had the same set-up (ie. 8 mm normal distance, 4 mm offset and 70° angle) and range as the NGQ sensor. Therefore, it can be assumed that the repeatability will be on the

Table F.9: Experimental sound speed and EGR data

EGR (.vol)	Mixture Temp. (°C)	Sound Speed (m/s) (eq. 4.11)
0.000	34.9	352
0.048	47.0	359
0.098	63.9	368
0.144	80.4	377
0.195	96.9	386

same order of magnitude as the NGQ sensor. The NGQ sensor's repeatability was found to be ±1.13 m/s; however, this will have to be expressed in %EGR for the EGR sensor. This can be done be relating the experimental EGR and sound speed data. Table F.9 shows the EGR measured and the mixture temperature inside the intake manifold. From this temperature the sound speed can be calculated using Eq. 4.11. The EGR and sound speed data can be plotted and a linear regression model is used to find the slope of the relationship. From the data shown the slope is 0.00565 $\frac{\%\mathrm{EGR}}{\mathrm{m/s}}$. The repeatability expressed in %EGR can be found by multiplying the slope by the repeatability expressed in m/s. Thus,

$$\delta_r = \pm 0.00565 \frac{\%\mathrm{EGR}}{\mathrm{m/s}} \times 1.13\mathrm{m/s} = \pm 0.0064\%\mathrm{EGR} \tag{F.12}$$

Therefore, the repeatability error in the prototype EGR sensor is ±0.0064 (vol.), or ±1.3% EGR

EGR Sensor Resolution Error

For the EGR sensor the sensor would produce a stable reading of 0.1 V. Therefore the resolution error, can be found from:

$$\begin{aligned}\delta_{res} &= \frac{\text{Output Resolution}}{\left|\frac{dV}{dEGR}\right|}\\ &= \frac{0.1\ \text{V}}{10.49\ \text{V/vol.}}\\ \delta_{res} &= \pm 9.5 \times 10^{-3}\ \text{vol.} = \pm 0.95\%\end{aligned}$$

Therefore, the resolution error is ±0.95% EGR.

EGR Sensor Accuracy

The accuracy of the EGR sensor can be calculated using the 'root-sum-square' method described earlier:

$$\begin{aligned}\delta_{total} &= \sqrt{(0.0095)^2 + (0.0062)^2 + (0.0064)^2}\\ \delta_{total} &= \pm 0.013\ \text{vol.} = \pm 1.3\%\end{aligned}$$

Therefore, the total error is ±0.13 (vol.), or ±1.3% EGR. Again, the maximum errors of calibration and resolution was used in each case. Therefore, this accuracy estimation is very conservative.

EGR Sensor Range

The range of the prototype is limited by the maximum operation temperature of the piezoelectric transducers used in the prototype. The transducers can only be operated to a maximum temperature of 60°C. At high EGR rates the temperature of the intake mixture can be much higher than the maximum operating temperature. Therefore, the experimental testing was limited to 0 - 20% EGR rates.